UCLouvain

AGRO LOUVAIN

Faculté des bioingénieurs

# Assessing the potential of enhanced silicate weathering in a tropical soil to remove atmospheric $CO_2$ and improve soil fertility: a modelling study

Author: Juliette Glorieux
Supervisor: Pierre Delmelle (AGRO/ELI/ELIE/SST)
Readers : Jean-Pascal van Ypersele de Strihou (ELI/ELIC/PHYS/SC/SST)
Yannick Agnan (AGRO/ELI/ELIE/SST)
Academic year 2021-2022
Master dissertation presented in partial fulfillment of the requirements for the degree of Master in Bioengineering: Environmental Bioengineering

# Summary

Enhanced silicate weathering in croplands is increasingly suggested as a negative emission technology that could remove significant quantities of $CO_2$ from the atmosphere and induce ancillary benefits to soil fertility and crop growth. However, many uncertainties remain as most existing enhanced silicate weathering studies rely on the extrapolation of laboratory weathering rates to calculate $CO_2$ removal and barely evaluate enhanced silicate weathering impact on soil properties. Moreover, different application modes and silicate materials are discussed but no studies precisely assess their effect under similar conditions. Given the scarcity of reactive transport modelling studies on enhanced silicate weathering with basalt and olivine, we use the reactive transport model CrunchFlow to investigate the effect of adding both crushed silicates to an Oxisol to enhance chemical weathering and atmospheric $CO_2$ removal. We tested two application rates (5000 and 150000 g $m^{-2}$) either added to the soil surface or mixed within the top 20 cm of the soil profile.

We show here that repeated addition of basalt leads to higher annual $CO_2$ removal than olivine. However, the basalt annual $CO_2$ removal gradually decreases with time, whereas the olivine $CO_2$ removal is predicted to remain stable. We estimate annual $CO_2$ removal in the range of 2172-4188 and 4231-6951 g $CO_2$ $m^{-2}$ $yr^{-1}$, after 30 annual applications of olivine and basalt respectively, subjected to 100 years of weathering. If deployed on tropical croplands, enhanced silicate weathering may thus sequester about 3.3-10.4% of the current annual anthropogenic $CO_2$ emissions. Our results demonstrate that both $CO_2$ removal efficacy and soil fertility improvement are maximised when the material is incorporated into the top soil layer.

We found that basalt application may lead to higher co-benefits for soil fertility as significant concentrations of $K^+$, $Ca^{2+}$ and $Mg^{2+}$ are released into the soil solution. As enhanced silicate weathering with olivine and basalt induces a significant increase in the soil solution pH, these nutrients will be readily available to crop plants. Moreover, repeated basalt application induces an increase in the cation exchange capacity, thereby increasing soil chemical fertility. In contrast, a $Ca^{2+}$ deficit in plants may arise after olivine amendment due to $Mg^{2+}$ continuous release.

Enhanced silicate weathering studies based on a reactive transport model would benefit from a comparison with data acquired through a long-term in situ enhanced silicate weathering experiment so as to validate the silicate weathering rates inferred theoretically and to better assess the actual co-benefits of enhanced silicate weathering for soil fertility. Nevertheless, reactive transport modelling offers a unique tool for exploring enhanced silicate weathering in soils under various environmental conditions, soil properties and silicate application modalities.

# Acknowledgments

First and foremost, I would like to address my most sincere gratitude to my supervisor, Pr. Pierre Delmelle. Thanks for sharing his passion and knowledge with us in the field in Ecuador and for his continuous support throughout the change in my Master dissertation subject and this eventful year. His judicious advice, reasoning, and expertise helped me to deepen my reflection throughout the realisation of this project. In addition, I want to thank you for the human connection that this project was accompanied by.

Besides Pr. Pierre Delmelle, I am extremely grateful for the friends I met in Canada. Thank you for supporting and accompanying me throughout the semester, for the motivation boost when it was hard to find, for filling day-to-day life with energy and laughter, and for all these new experiences we had the opportunity to share.

I would like to extend my appreciation to Pr. Jean-Pascal van Ypersele and Yannick Agnan for agreeing to be a part of my jury. I truly appreciate the time and energy dedicated to reading and evaluating this master dissertation.

I also wish to thank Marlon Calispa for his enthusiasm in all situations and help while working in the field in Ecuador. Thank you for making us discover your wonderful country. All the knowledge he shared enabled me to broaden my thinking. Muchas gracias Marlon for being available when needed during the completion of this study.

Thanks to all my friends and fellow bioengineer students for making these 5 years at university so memorable. I would especially like to thank Hind Dib with whom I shared the intense journey that is a Master thesis.

Last but not least, I would like to express a very special thanks to my family for their unwavering support, love and belief in me. Thanks to my mother for her wise counsel and my stepfather for proofreading this thesis. Thanks to my brother and sisters for their constant positive attitude which helped me to relax along the way.

# List of Acronyms

| | |
|---|---|
| **BECCS** | Bioenergy with Carbon Capture and Storage |
| **CDR** | Carbon Dioxide Removal |
| **CEC** | Cation Exchange Capacity |
| **$CO_2$** | Carbon Dioxide |
| **ESW** | Enhanced Silicate Weathering |
| **ET** | Evapotranspiration |
| **GHG** | Greenhouse Gas |
| **IPCC** | Intergovernmental Panel on Climate Change |
| **LLNL** | Lawrence Livermore National Laboratory |
| **NDC** | Nationally Determined Contribution |
| **NETs** | Negative Emission Technologies |
| **$P_{CO_2}$** | Partial pressure of $CO_2$ |
| **PZC** | Point of Zero Charge |
| **REV** | Representative Elementary Volume |
| **RTM** | Reactive transport modelling |
| **SRM** | Solar Radiation Management |
| **SSA** | Specific Surface Area |
| **TST** | Transition State Theory |
| **UNFCCC** | United Nations Framework Convention on Climate Change |
| **WMFR** | Well-mixed Flow through Reactor |

# Contents

# List of Figures

# List of Tables

# 1 Introduction

Due to rapid industrialisation and the associated increase in greenhouse gas emissions, the global mean temperature has risen by at least 1.1 °C since 1880 (NASA's Goddard Institute for Space Studies [GISS], n.d.). To avoid dangerous climate change and serious implications for the next generations, action to limit global temperature rise to a maximum of 2 °C — preferably 1.5 °C — above pre-industrial levels is urgently needed ( Edwards et al., 2017; de Coninck et al., 2018; Canadell et al., 2021). According to several studies, including the last IPCC report, the currently-planned measures are not fit for purpose and will not reduce greenhouse gas emissions sufficiently to keep global warming within these targets by the end of the century (Fuss et al., 2016; Fuss et al., 2018, IPCC, 2022a). Therefore, IPCC climate scenarios limiting global warming to 1.5 or 2 °C rely on widespread application of both a significant reduction in greenhouse gas emissions and technologies that remove $CO_2$ from the air on a massive scale by 2100 (Rockström et al., 2017; United Nation Environmental Program [UNEP], 2018; Goll et al., 2021). Numerous uncertainties surrounding the efficacy and potential consequences of these so-called negative emission technologies (NETs) subsist, resulting in vigorous scientific, economic and ethical debate (Lawford-Smith and Currie, 2017; Bradford et al., 2019). However, halting the increase in greenhouse gas (GHG) concentrations in the atmosphere is a race against time and one of the largest challenges – if not the largest – mankind is facing. Therefore, all measures that can potentially temper the build-up of $CO_2$ concentration in the atmosphere should be considered and their efficacy and side effects assessed.

Among the NETS that are currently discussed, enhanced silicate weathering (ESW) refers to the application of crushed silicate minerals or rocks to the soil surface (e.g. Beerling et al., 2020) or the ocean (Meysman and Montserrat, 2017) to enhance slow chemical reactions that naturally break down silicates and consume $CO_2$ from the atmosphere, leading to its sequestration at geological timescales (Berner, 1992; Kump et al., 2000). ESW deployement, along with other strategies, over several decades has gained increased interest as a nature-based option that may offer an interesting $CO_2$ removal (CDR) potential of 2-4 Gt $CO_2$ $yr^{-1}$ (Canadell et al., 2021). In addition, when applied to soils, ESW may also result in co-benefits in terms of chemical fertility and crop productivity through soil pH increase and slow nutrient release (ten Berghe et al., 2012; Kantola et al., 2017; de Oliveira Garcia et al., 2020).

However, the efficacy of ESW in soils to remove $CO_2$ from the atmosphere has not yet been fully evaluated and its potential negative repercussions on soil properties and functioning remain unclear. In fact, existing studies have produced uncertain or even contrasting results. Moreover, various modalities and soil settings for deploying ESW have been proposed, but a rigorous quantification of the pros and cons of each configuration is lacking. Notably, some authors (e.g. Beerling et al., 2020; de Oliveira Garcia et al., 2020) suggest to apply a silicate powder as a thin layer to the soil surface, whereas others argue that the material should be incorporated into the plough mixing depth (Kelland et al., 2020; Lewis et al., 2021; Vienne et al., 2022). The ideal composition of the silicate is also questioned. Olivine (a magmatic mineral) was initially thought to be the best mineral for ESW, but basalt (a common volcanic rock with a low silica content) is now increasingly being researched. Although basalt has a reduced potential for atmospheric $CO_2$ removal, its chemical weathering may generate greater co-benefits to agriculture compared to olivine.

Clearly, a thorough assessment of the impact of enhanced silicate weathering - and its numerous

modalities - on weathering rates (and consequently, $CO_2$ removal potential) and on soil physical and chemical properties are urgently needed. The aim of our Master research is to contribute to a better description of the geochemical reactions and their temporal evolution (over a period of 100 yr) which take place when ESW is implemented in soils. A such study should provide new evidence for correctly assessing the impact of the technique on (i) $CO_2$ removal from the atmosphere and (ii) soil's key properties and functioning.

# 2 State of the Art

Since the 1800's, global average temperatures have been rising dramatically. The last decade (2011-2020) is the warmest on record and, apart from global temperature rise, global climate change bears other hazardous consequences such as sea level rise, ocean acidification, loss of biodiversity and intensification of extreme climate events (i.e. storms and droughts) (United Nations [UN], n.d.). Climate change also threatens our ability to grow food and our health and safety. Human activity has been the main driver of climate change, mainly due to increased GHG emissions (notably $CO_2$) by burning fossil fuels as coal, oil and gas (UN, n.d.).

Nations worldwide agree that action to limit global temperature rise to a maximum of 2 °C — preferably 1.5 °C — above pre-industrial levels, as defined in the United Nations Framework Convention on Climate Change (UNFCCC) Paris Agreement, is urgently needed to avoid dangerous climate change and serious implications for future generations (Edwards et al., 2017; de Coninck et al., 2018; Canadell et al., 2021). Current nationally determined contributions (NDC) and even the most ambitious emissions phase-out are insufficient to reach these goals (UNEP, 2018; Beerling et al., 2020). Pathways likely to limit warming within these targets by 2100 presented in the last Intergovernmental Panel on Climate Change (IPCC) report, now all require large-scale carbon dioxide ($CO_2$) removal (Sanderson et al., 2016; Beerling et al., 2018; Minx et al., 2018; Beerling et al., 2020; Canadell et al., 2021) to counterbalance residual emissions along with a rapid, significant decrease in GHG emissions in all sectors (IPCC, 2022a; Figure A.1). Scenarios following NDCs until 2030 even highlight an amplified dependence on CDR later in the century to make up for these higher emissions (IPCC, 2022a).

In order to achieve CDR, geoengineering techniques have been increasingly put forward and researched. The prospect of deploying these NETs over several decades stirs vigorous scientific, economic and ethical debate (Lawford-Smith and Currie, 2017; Bradford et al., 2019) due to numerous uncertainties surrounding their efficacy and potential consequences. However, halting the increase in GHG concentrations in the atmosphere remains a race against time, and NETs are necessary to compensate for the inadequacy of currently-planned measures for reducing greenhouse gas emissions (Fuss et al., 2016; Fuss et al., 2018).

## 2.1 Geoengineering

Geoengineering refers to a broad set of techniques through which the climate system is deliberately modified at a large-scale so as to mitigate the effects of climate change (Keith, 2000; Köhler et al., 2010; Boucher et al., 2013; Stocker et al., 2013). These NETs are divided between solar radiation management (SRM) methods, aiming to mitigate the warming caused by anthropogenic GHG emissions by increasing the planet's reflectivity, and CDR methods, which intend to slow down the increase or reduce atmospheric $CO_2$ concentration (Figure 1; Boucher et al., 2013; Stocker et al., 2013).

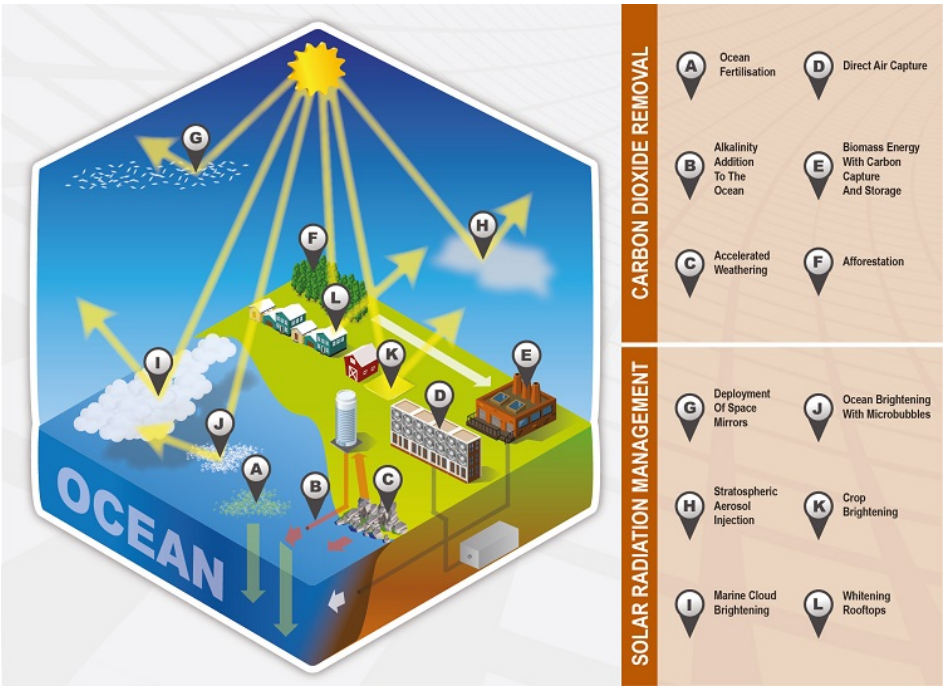


Figure 1: Overview of proposed geoengineering techniques. Carbon Dioxide Removal methods: (A) ocean fertilisation through nutrient input resulting in an increase in ocean productivity and the transport of a fraction of the resulting biogenic carbon downward; (B) alkalinity addition to the ocean from solid minerals enhancing atmospheric $CO_2$ dissolution in the ocean; (C) increasing weathering rate of silicate minerals and transport of the dissolved carbonate minerals produced to the ocean; (D) chemical capture of atmospheric $CO_2$ and its storage underground or in the ocean; (E) capture of the $CO_2$ emitted during biomass combustion in an electric power plant and its storage underground or in the ocean; and (F) $CO_2$ storage by land biomass through afforestation and reforestation. Solar Radiation Management methods: (G) installation of reflectors to reflect sun radiation; (H) injection of aerosols in the atmosphere; (I) enhancing marine clouds reflection through seeding; (J) production of microbubbles at the surface of the ocean to make it more reflective; (K) growing more reflective crops; and (L) whitening of roofs and buildings (Boucher et al., 2013).

### 2.1.1 Solar radiation management

Solar radiation management methods aim to modify Earth's radiative budget to reduce average global surface temperature (Stocker et al., 2013). Most methods, such as stratospheric aerosol injection or marine cloud brightening, aim to reduce incoming solar radiation reaching the surface by making the planet more reflective (Stocker et al., 2013). Other techniques propose to decrease optical thickness or clouds lifetime to increase outgoing longwave radiation and reduce the greenhouse effect (Stocker et al., 2013; Canadell et al., 2021).

Solar radiation management approaches could offset part of global warming effects, like reducing maximum global surface temperature (Boucher et al., 2013). However, SRM deployment must be maintained as long as GHG emissions continue and even increase if GHG atmospheric concentration continues to rise to avoid a rapid global temperature increase. Moreover, SRM techniques do not address other key consequences of global warming such as ocean acidification (Boucher et al., 2013; Ciais et al., 2013; IPCC, 2022b). Large uncertainties remain on the feasibility, efficacy, potential co-benefits and negative side effects (Boucher et al., 2013; IPCC, 2022b). For example, it is acknowledged that SRM is expected to cause a small but significant decrease in global precipitation, which could impact crop productivity worldwide (Boucher

et al., 2013). These techniques must be deployed alongside other efforts to reach zero or net negative $CO_2$ emissions as they will not stop $CO_2$ concentration from increasing in the atmosphere (Boucher et al., 2013), emphasising the need for CDR methods.

### 2.1.2 Carbon dioxide removal

Carbon dioxide removal involves manipulating the carbon cycle to enhance biological or geological sinks, or the deployment of an industrial process that captures $CO_2$ directly from the atmosphere and stores it permanently (Boucher et al., 2013; Canadell et al., 2021). Each approach has its own maturity and potential, and involves different costs, risks, co-benefits, negative side effects and timescale of carbon storage. The timescale of carbon storage ranges from decades to centuries for vegetation and soil reservoirs to thousands of years when carbon is stored in the ocean or in geological formations (IPCC, 2022a).

To have a tangible effect on atmospheric $CO_2$ concentration, CDR techniques will have to be deployed globally and during several decades and perhaps up to a century (Boucher et al., 2013). A CDR of 5 Gt $CO_2$ $yr^{-1}$ by 2050 has been suggested in decarbonation scenarios (Rockström, 2017). Along the reduction of $CO_2$ atmospheric concentration, CDR methods address three other issues on different timescales. In the short term, they contribute to the reduction in net $CO_2$ and GHG emissions (IPCC, 2022a). In the mean term, these techniques are required to offset hard-to-abate residual emissions from industrial activities, transport or agriculture and achieve net-zero emissions both globally and nationally (Strefler et al., 2018; Johansson et al., 2020; Riahi et al., 2021; IPCC, 2022b). Aligned with the second objective, in the long term, they will help to reach net negative $CO_2$ or GHG emissions if their deployment enables carbon sequestration to exceed annual residual emissions (IPCC, 2022a).

Carbon dioxide removal techniques are still being developed and their potential and constraints remain difficult to evaluate (Boucher et al., 2013; Canadell et al., 2021). The most investigated techniques are land-based biological CDR with afforestation and reforestation or bioenergy with carbon capture and storage (BECCS) (Goll et al., 2021, IPCC, 2022a), whereas ESW has been gaining increased attention. Afforestation and reforestation is already largely practiced. Although it favours biodiversity, employment and local activities, this technique has a relatively low carbon sequestration potential (0.5 to 1.1 Gt $CO_2$ $yr^{-1}$). In addition, negative socio-economic and environmental impacts (Vaughan and Gough, 2016; Boysen et al., 2017; IPCC, 2022a), for example, on biodiversity, fresh water use, or land-use competition, may arise if inadequately managed (Heck et al., 2018; Fuhrman et al., 2021; IPCC, 2022a).

Bioenergy with carbon capture and storage is the process of producing energy from sustainably sourced biomass, which absorbs $CO_2$ during its growth, and capturing and storing the carbon produced in the energy generation process, thus removing it from the atmosphere. The carbon sequestration potential for BECCS ranges from 0.5 to 11 Gt $CO_2$ $yr^{-1}$ (IPCC, 2022a). While this process can improve waste management and enhance air quality, therefore implying public health benefits (IPCC, 2022a), it must be deployed cautiously to avoid land and water use competition for biodiversity conservation or food production (Heck et al., 2018; Fuhrman et al., 2021; IPCC, 2022a).

Among CDR, ESW is increasingly regarded as a nature-based option that could contribute significantly to carbon sequestration as its potential is estimated between 2 and 4 Gt $CO_2$ $yr^{-1}$ (Schuiling and Krijgsman, 2006; Hartmann et al., 2013; Strefler et al., 2018; Canadell et al.,

2021; IPCC, 2022a). Enhanced silicate weathering refers to the stimulation of slow chemical processes that naturally break down silicate rocks and consume $CO_2$ from the atmosphere, ultimately leading to $CO_2$ being locked up in carbonates on the ocean floor (Berner, 1992; Kump et al., 2000). Aside from an interesting carbon sequestration potential, ESW brings forward several co-benefits like enhancing plant growth, countering ocean acidification and various potential positive effects on soils (ten Berghe, 2012; Beerling et al., 2020; de Oliveria Garcia et al., 2020; Kelland et al., 2020; IPCC, 2022a). Our study focuses on this CDR approach, which is detailed in the following sections.

## 2.2 Enhanced weathering

At geological timescale (>100000 years), silicate weathering exerts a major control in regulating atmospheric $CO_2$ concentration (Colbourn et al., 2015; Amann et al., 2020). Carbonic acid provided by the dissolution of atmospheric $CO_2$ in rainwater accelerates the chemical weathering of silicate rocks. This process then generates bicarbonate as well as cations such as $Ca^{2+}$ or $Mg^{2+}$ (Equation 1). Eventually, this bicarbonate may be transported by rivers or groundwater to the ocean where it is stored as alkalinity at millennial timescales (Köhler et al., 2010; Colbourn et al., 2015; Lewis et al., 2021).

$$CaSiO_{3(s)} + 2CO_{2(aq)} + H_2O \rightleftharpoons Ca^{2+} + 2HCO_3^- + SiO_{2(aq)} \quad (1)$$

Carbonates may precipitate in the soil (Manning, 2008) or on the ocean floor (Equation 2), leading to a net uptake of 1 mol of $CO_2$ for every 2 mol of $CO_2$ consumed during silicate weathering (Equation 1). Some authors also suggested using carbonates for enhanced weathering but, because of carbonates precipitation, this process would yield no net $CO_2$ sequestration on longer timescale (Hartmann et al., 2013; Amann et al., 2020).

$$Ca^{2+} + 2HCO_3^- \rightleftharpoons CO_{2(aq)} + H_2O + CaCO_{3(s)} \quad (2)$$

Enhanced silicate weathering intensifies the natural dissolution of silicate rocks that naturally absorbs $CO_2$ from the atmosphere, ultimately locking it up as carbonate on the ocean floor at geological timescale (Schuiling and Krijgsman, 2006; Hartmann et al., 2013; Beerling et al., 2018; Goll et al., 2021). The technique involves the mining, comminution and spreading of finely ground unstable silicate rocks or minerals on croplands (eg. Beerling et al., 2018; Strefler et al., 2018; Beerling et al., 2020) or forests soils (Haraldsen and Pedersen, 2003; de Oliveria Garcia et al., 2018), although application directly into the ocean and in coastal zones is also investigated (Meysman and Montserrat, 2017). By increasing the exposed reactive surface, ESW stimulates this slow chemical process.

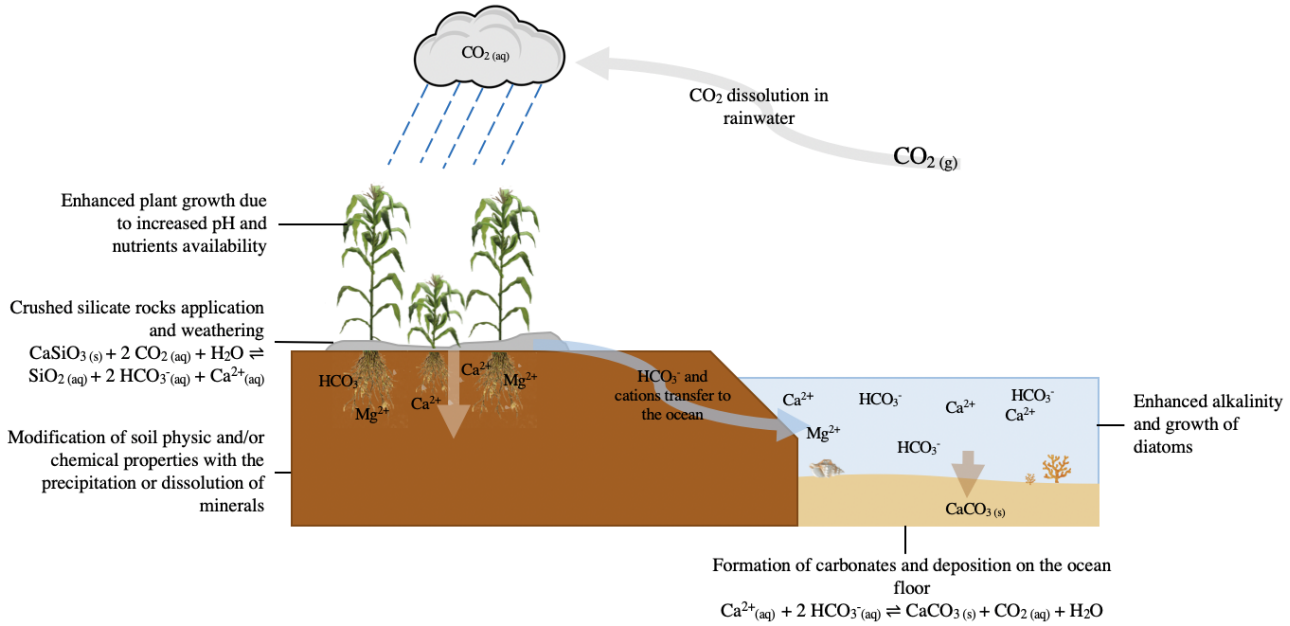


Figure 2: Schematic representation of potential effects of enhanced silicate weathering (ESW). Modified from Kelly et al. (2010) and Beerling et al. (2018).

### 2.2.1 Potential of enhanced weathering as a CDR technique

Predicting the potential of ESW to remove $CO_2$ from the atmosphere is essential to eventually recommend its use as a NET. Numerous studies evaluate ESW CDR potential which is estimated in the range of 1-5 Gt $CO_2$ $yr^{-1}$ globally (Fuss et al., 2018; Beerling et al., 2020; Goll et al., 2021). For example, Strefler et al. (2018) estimated CDR potential of basalt to 4.9 Gt $CO_2$ $yr^{-1}$ when spread over croplands in warm and temperate humid regions. Köhler et al. (2010)'s study evaluated olivine CDR potential to 3.7 Gt $CO_2$ $yr^{-1}$ when distributed over the humid tropics in the Amazon and Congo river catchments. Renforth (2012) has computed a potential of 430 Gt $CO_2$ for the United Kingdom based on the available silicate materials. However, current estimates are surrounded by large uncertainties and do not take the same parameters into account, betraying important gaps in knowledge. Following Strefler et al. (2018), the $CO_2$ removal rate in ESW is influenced by three factors: the amount of rock spread, the dissolution rate and the carbon sequestration potential of the amended silicate material. To have a tangible influence on atmospheric $CO_2$, soil amendment with silicates to boost weathering will have to be repeated annually over several decades (Lawford-Smith and Currie, 2017; Fuss et al., 2018; Beerling et al., 2020). Suggested annual applications rates range from 5 kg $m^{-2}$ up to 20 kg $m^{-2}$ (Schuiling and Krijgsman, 2006; Renforth, 2012; ten Berghe et al., 2012; Amann et al., 2018; Beerling et al., 2020).

#### Silicates weathering rates

The rate at which a silicate rock (comprised of minerals) or an individual mineral deliberately added to soil weathers governs the rate at which $CO_2$ is consumed from the atmosphere. Due to the lack of reliable field weathering rates, most ESW studies rely on mineral weathering kinetics extrapolated from laboratory experiments (Hartmann et al., 2013; Kantola et al., 2017; Beerling et al., 2018; Fuss et al., 2018; Strefler et al., 2018), but it is well known that the rate

of weathering of silicate minerals in the field is much lower (by one to five orders of magnitude) than would be predicted by rates of dissolution of the same minerals in the laboratory (Brantley et al., 2008).

Silicate weathering is a temperature-dependent process that requires water and is sped up by high temperatures (Strefler et al., 2018). Therefore, warm to temperate and humid climates are ideal for implementing ESW (Brantley et al., 2008; Hartmann et al., 2013; Taylor et al., 2016). Croplands seem to be the most suitable targets to allow for cost-effective large-scale rapid deployments of ESW within decades (Beerling et al., 2018). As agricultural soils have been amended with carbonate rock powder to improve soil quality and productivity for a long time (Anda et al., 2013), they are easily accessible and infrastructures and agricultural machinery are already existing and available (Beerling et al., 2018; Strefler et al., 2018). Furthermore, the use of croplands for ESW would not compete with other land uses for resources. Some studies demonstrated that China, India and the United States present the highest CDR potential, followed by Brazil and Indonesia, which take advantage of their warm seasonally humid climate and large proportion of arable lands (Strefler et al., 2018; Beerling et al., 2020). European countries also bear an interesting potential estimated an order of magnitude lower than China, India and the USA primarily because of the smaller availability of agricultural lands (Beerling et al., 2020).

Weathering rates of minerals also depends on grain size (Strefler et al., 2018). Grinding the rocks/minerals to small particles increases the reactive surface area, which considerably enhances weathering rates compared to the natural, geological process (Lewis et al., 2021). For example, a grain size of 10 $\mu$m maximum is required for olivine ($(Mg,Fe)_2SiO_4$) dissolution within 1 or 2 years at typical pH for tropical soils (i.e. 4-6) (Hangx and Spiers, 2009), whereas a 20 $\mu$m-powder is needed for basalt to be dissolved within 50 years (Goll et al., 2021).

### Carbon sequestration potential of silicate materials

Ultramafic (e.g. olivine) and mafic (e.g. basalt), typified by low silica-content in the range 50-40 wt.% (Figure 3), silicates are the compositions targeted for large-scale ESW deployment (Schuiling and Krigsman, 2006; Kantola et al., 2017; Beerling et al., 2018; Lewis et al., 2021) as they typically have high weathering rates (Renforth, 2012) and carbon dioxide sequestration potential (Strefler et al., 2018). The latter is estimated to 1 g of $CO_2$ per g of olivine (Köhler et al., 2010) or 0.3 g of $CO_2$ per g of basalt (Strefler et al., 2018).

Owing to its rapid weathering ($10^{-10}$ to $10^{-12}$ mol $m^{-2}$ $s^{-1}$ at pH$\approx$8), olivine is regarded as a mineral of choice in ESW (Schuiling and Krijgsman, 2006; Köhler et al., 2010; ten Berghe et al., 2012; Hartmann et al., 2013; Taylor et al., 2016). However, the mineral unavoidably carries harmful trace elements that can be released in the environment during weathering and dissolution (Keller et al., 2018; Strefler et al., 2018). Recently, basalt has gained increased attention as this rock is poor in potentially toxic trace elements, thus minimising potential negative side effects associated with its use (Taylor et al., 2016; Beerling et al., 2018; Strefler et al., 2018). The dissolution rate of basalt ($10^{-10}$ to $10^{-12}$ mol $m^{-2}$ $s^{-1}$ at pH$\geq$4) is lower than that of olivine, but is still interesting (Brantley et al., 2008; Beerling et al., 2018). Importantly, basalt offers several co-benefits for crop productivity (Kelland et al., 2020) and soil health (Beerling et al., 2018). These aspects are discussed in more detail in the following section. Several authors argue that the slower weathering of basalt compared to olivine will be compensated by

enhanced carbon storage in plant biomass driven by the release of key nutrients (e.g., K, Ca and P) from the silicate rock (Anda et al., 2015; Goll et al., 2021).

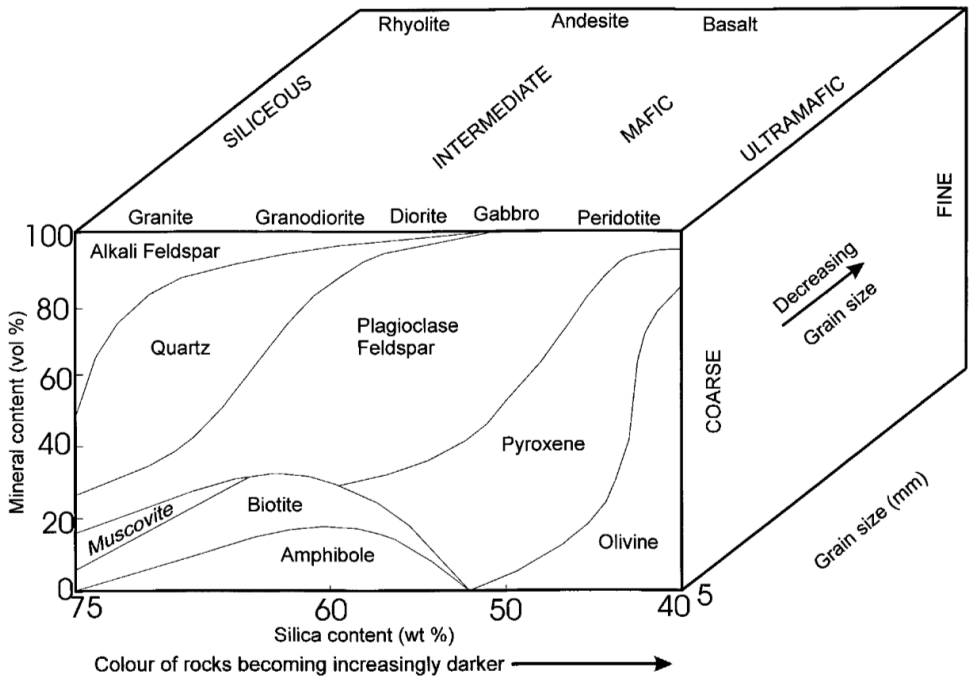


Figure 3: Classification of igneous rocks as a function of silica content, mineral content and grain size (Le Maitre, 1989; Thorpe and Browne, 1989).

### 2.2.2 Enhanced silicate weathering co-benefits

Soil productivity and health

Food security is a growing threat around the world because of declining soil quality and quantity (Van Straaten, 2006). Besides the potential for removing $CO_2$ from the atmosphere, ESW evokes various positive effects in croplands. By generating alkalinity, ESW may assist in buffering low soil pH, in turn improving crops nutrient uptake and yield. Furthermore, basaltic rocks can contain key plant nutrients, such as potassium or phosphorous in basaltic rocks, that are released during dissolution (Van Straaten, 2006; Hartmann et al., 2013). With the declining resources of macro-nutrients rich rocks (Manning, 2015), silicate rocks and minerals could be alternatives to reduce the demand for conventional fertilisers used to ameliorate soil fertility and crop production (Hartmann et al., 2013; Amann et al., 2020), helping to ensure long-term sustainability of rock supply (Van Straaten, 2006; de Oliveria Garcia et al., 2020). Slow geogenic nutrients release from silicate amendment is especially interesting in tropical regions where soils are in deficit for optimal plant growth, and nutrients leaching is an issue (Anda et al., 2009; Ciais et al., 2013; Hartmann et al., 2014; Goll et al., 2021).

Adding silicate rocks to soils may also encourage carbon storage in soils. This results from the weathering reactions and release of Si, Al, and other cations in the soil solution that may lead to the formation of secondary solid phases (such as clay minerals and iron oxy(hydrox)ides) that can stabilise organic carbon via physico-chemical interactions (Peña-Ramírez et al., 2009). In addition, increased organic carbon storage ameliorates soil structure and stability and resistance to erosion, thus contributing to alleviate soil degradation (Van Straaten, 2006; Beerling

et al., 2018). Moreover, a higher soil organic carbon content usually improves soil water retention (de Oliveira Garcia et al., 2020), thereby promoting plant growth and ESW potential for agriculture (Van Straaten, 2006; Kelland et al., 2020) and forestry (Peña-Ramírez et al., 2009).

Finally, silicates amendment weathering may also increase cation exchange capacity (CEC) (Gillman, 1980; Van Straaten, 2006; Shamshuddin and Kapok, 2010). An increased CEC may enhance nutrients retention and availability, in turn promoting plant growth. The cation exchange capacity of a soil can be seen as its ability to retain cations on the exchange complex that forms a reserve of nutrients available to the plant. The CEC of a soil (Figure 10) varies with the %wt. of clay, the type of clay, soil pH and the amount of organic matter. Each clay mineral (including amorphous solid phases) is characterised by a CEC that depends on its permanent charges - linked to cations substitutions in the clays -, and variable charges - controlled by chemical functions which can be protonated of deprotonated as a function of the pH (i.e. alcohol function). The point of zero charge (PZC) shows the pH at which a specific solid phase's surface is globally neutral. As a result, when the pH is higher than the PZC, the particles will be charged negatively and contribute to the CEC, whereas when pH $\leq$ PZC, the particle contribution will depend on its permanent charges. A higher specific surface area (SSA) also enhances the CEC as more exchange sites are exposed at the surface. For example, kaolinite has a relatively low CEC (3-15 $cmol_c\ kg^{-1}$), whereas allophanes have an important one (20-150 $cmol_c\ kg^{-1}$).

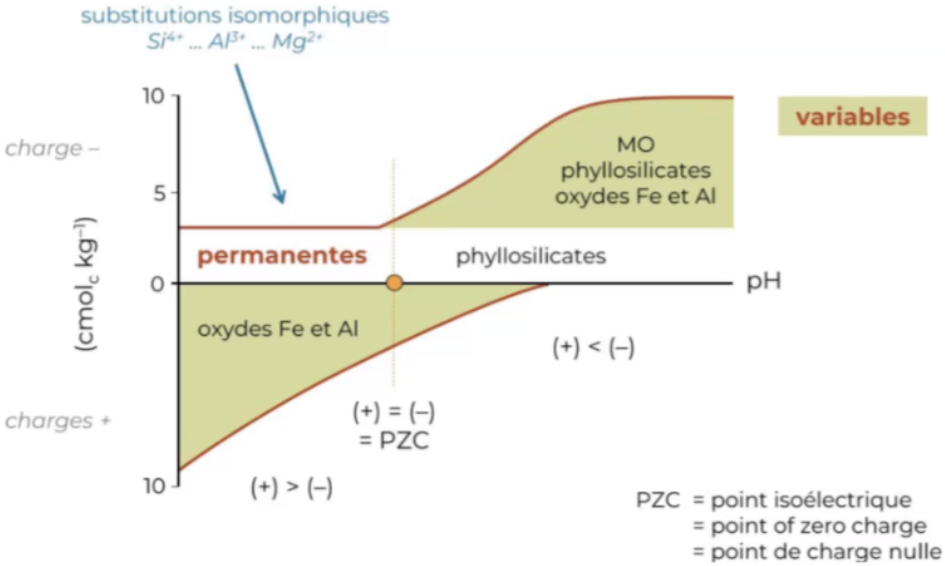


Figure 4: Schematic representation of the cation exchange capacity evolution as a function of pH. The point of zero charge highlights the pH at which the particle surface is globally neutral. Oxides of Fe and Al and organic matter mainly depend on variables charges to contribute to the CEC, hence, their contribution varies with pH.

Oxisols mostly consists in Fe and Al oxides and hydroxides as well as kaolinite, which are all characterised by a low CEC depending on variable charges. Silicates weathering may increase Oxisols' CEC following several mechanisms. Firstly, the increase in pH caused by ESW may be sufficient to exceed the PZC of some solid phases, enhancing their contribution to the soil's CEC. Second, the precipitation of secondary solid phases characterised by a high CEC or SSA may contribute (Shamshuddin and Kapok, 2010). Third, higher organic matter storage, through its stabilisation (Peña-Ramírez et al., 2009), means it will contribute more consequently to the

soil's CEC.

Another potential effect of silicate amendments to cultivated soils may be the reduction of nitrous oxide, a GHG, emissions (Kantola et al., 2017; Beerling et al., 2020; Goll et al., 2021). The role of silicic acid released during silicate weathering in strengthening plant resistance to pests and diseases is also recognised (Hartmann et al., 2013). Silicon can also increase crop resilience to drought by reducing leaf transpiration rates, which can increase water-use efficiency (Hartmann et al., 2013).

### Counteract ocean acidification

Enhanced silicate weathering would increase land-to-ocean fluxes of alkalinity and dissolved inorganic carbon, an effect that would aid in countering future ocean acidification caused by rising atmospheric $CO_2$ (Köhler et al., 2010; Hartmann et al., 2013; Taylor et al., 2016; Beerling et al., 2018; Strefler et al., 2018; Kelland et al., 2020). Moreover, ESW CDR potential might be enhanced through ocean processes including (i) the dissolution of silicate rocks/minerals in the ocean; (ii) increased $CO_2$ uptake by diatoms which are often limited by silicate availability, provided by the input of $H_4SiO_4$ from silicates materials dissolution (Dugdale and Wilkerson 1998); and (iii) enhanced gas exchanges between the atmosphere and the ocean because of increased alkalinity reducing the partial pressure of $CO_2$ ($P_{CO_2}$) in the surface ocean (Zeebe and Wolf-Gladrow, 2001).

All in all, ESW could address crucial $21^{st}$ century issues and gives the opportunity to align climate and agricultural policies (Figure 5). It supports several United Nations sustainable development goals (Beerling et al., 2020) including:

- Zero hunger (2) through enhancement of crop production, and thus food supply, thanks to geogenic nutrients release.
- Responsible consumption and production (12) by reducing agrochemical fertilisers use and encouraging recycling waste.
- Climate action (13) as it presents an interesting CDR potential of 2 to 4 Gt $CO_2$ $yr^{-1}$.
- Life below water (14) by offsetting ocean acidification and its impact on marine biodiversity.
- Life of land (15) with various positive effects on soil health like decreasing erosion and nutrients loss or enhancing water retention.

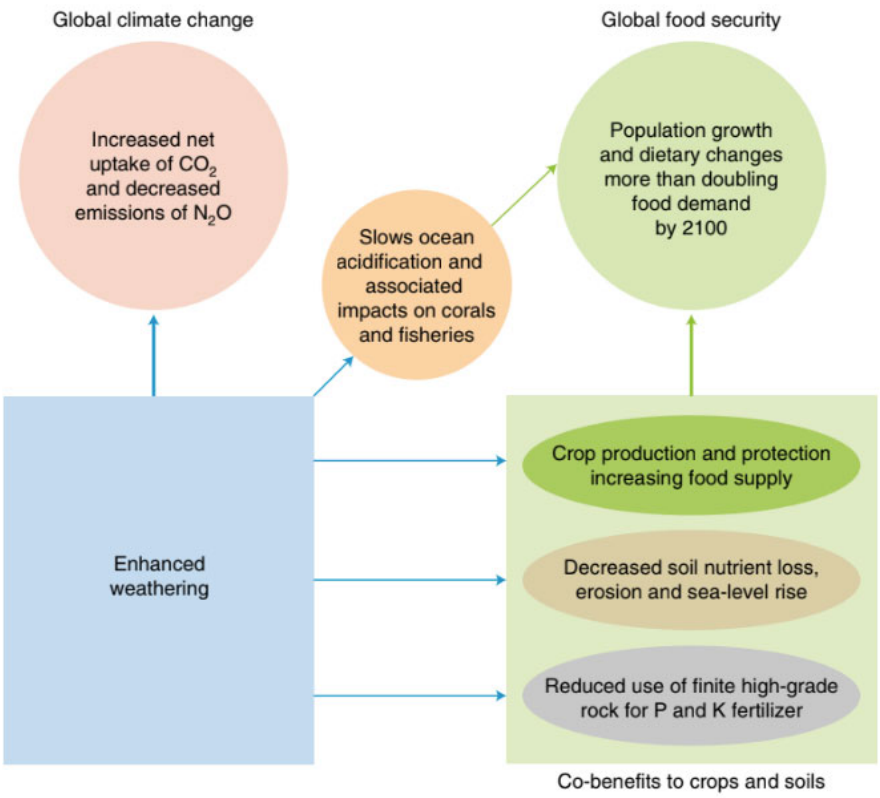


Figure 5: Illustration of potential co-benefits of large-scale deployment of enhanced silicate weathering. It could address crucial issues related to global climate change, food and soil security (Beerling et al., 2018).

### 2.2.3 Enhanced silicate weathering other considerations

It is behind the scope of this study to evaluate the techno-economic feasibility of ESW as a CDR technique. However, it is important to mention that the steps prior to the weathering of the silicate amendment itself, i.e. mining, crushing, transporting, and spreading the silicate material, require energy input and involve GHG emissions (Moosdorf et al. 2014; Beerling et al., 2018; Strefler et al., 2018). Moosdorf et al. (2014)'s study highlighs that rock grinding is a key step regarding GHG emissions that could offset the CDR benefits of ESW, whereas GHG emissions related to material mining and application are negligible. Greenhouse gas emissions of transport highly vary with the mean of transport, the distance, and the remoteness of the application location (Moosdorf et al., 2014; Strefler et al., 2018).

Regarding the comminution of the silicate materials, it is technically feasible to grind the rocks/minerals to particles smaller than 10 $\mu$m. However, the energy demand and costs required for the process increase with decreasing grain size (Beerling et al., 2018; Strefler et al., 2018). Moreover, grinding may be associated with a health hazard as small particles ($\leq$10 $\mu$m) can induce or exacerbate respiratory problems (Schenker et al., 2009). Therefore, grain sizes between 10 and 50 $\mu$m are seen as the most suitable to combine fast weathering rates, reasonable costs and energy demand and health considerations (Hartmann et al. 2013; Strefler et al., 2018). The use of renewable energy could also help reduce GHG emissions associated with this step (Moosdorf et al., 2014; Beerling et al., 2018). Moreover, the need for mining extension can also impact ecosystems and biodiversity, through the destruction of habitats, as well as

human health, with dust production. To obviate this need, the potential to use excess silicate materials such as iron and steel slag or basalt mine overburden has been brought forward in several studies (Renforth et al., 2011; Renforth, 2019; Beerling et al., 2020).

## 2.3 Reactive transport modelling

Reactive transport modelling (RTM) is a numerical tool enabling the simultaneous analysis of the biogeochemical reactions taking place in a porous medium and the solute transport and flow processes influencing these reactions (Steefel et al., 2005; Li et al., 2017). Complex natural Earth systems include various time- and space-dependent processes in interaction (Steefel et al., 2005). They are characterised by mass transport processes, such as diffusion or flow of gases, fluids (gases and liquids) and solids, during which chemical, biological and geochemical interactions occur (Steefel et al., 2005). These processes are often coupled, hence, the reactions taking place can modify the physical properties of the medium, inducing feedback on transport processes and thus, on biogeochemical reactions (Steefel et al., 2005). For example, in the case of ESW, weathering of silicate amendments may modify soil properties, through processes such as mineral dissolution or precipitation, in turn influencing flow patterns and chemical weathering reactions. Reactive transport models allow the study of such complex systems.

In essence, RTM couples a physically based model that describes fluid transport mechanisms, and geochemical calculations that characterise the thermodynamic state of dissolved species, minerals, and gases and account for the reactions kinetics framework (Steefel et al., 2015). The studied medium is modelled as a column of cells (or representative elementary volumes, REV) that mimics well-mixed flow through reactors (WMFRs) (Figure 6; Steefel et al., 2005; Steefel et al., 2015; Maher and Mayer, 2019). This means that in each of these WMFRs, the properties of the system are averaged to the same value and solid, liquid, and gaseous phases all coexist. The grid cells are linked through the flow of an aqueous solution described by Darcy's law, which states that the water flux is proportional to the product of the hydraulic gradient and the hydraulic conductivity (Maher and Mayer, 2019). To properly characterise the mass fluxes, the dispersivity and/or diffusion of dissolved species must be described (Maher and Mayer, 2019). In each cell, the evolution of geochemical species is determined by solving mass balance equations (Maher and Mayer, 2019).

As illustrated in Figure 6, a RTM considers a wide variety of reactions in the reaction network including (A) mineral dissolution and precipitation reactions, (B) homogeneous reactions within the aqueous phase, (C) surface complexation reactions, (D) ion exchange reactions, (E) exchanges between the gaseous and aqueous phases, and (F) homogeneous and heterogeneous reactions controlled by microorganisms (Steefel et al., 2015). These reactions are either kinetically- or equilibrium-controlled (Steefel et al., 2015). As a consequence, any study using RTM must rely on databases where the equilibrium constants and reaction rates are compiled for a variety of chemical reactions (Maher and Mayer, 2019). The rate values typically derive from experimental studies, but are not available or only loosely constrained for several solid phases and aqueous complexes (Maher and Mayer, 2019). In addition, reaction rates measured in the laboratory can differ up to five or six orders of magnitude from those observed in the field (Brantley et al., 2008). This probably reflects factors either affecting the amount of reactive surface of minerals available for reaction or regulating aqueous solution composition (Steefel et al., 2005; Steefel et al., 2015).

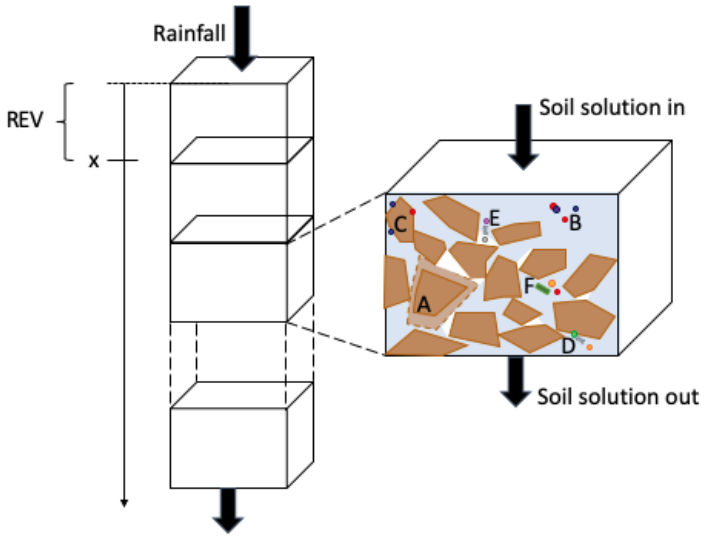


Figure 6: Schematic representation of a continuum RTM. The porous medium is represented as a series of control volumes (or REV) in which liquid, gaseous and solid phases coexist. Each cell is considered as a well-mixed flow reactor in which a variety of equilibrium or kinetically controlled reactions are taken into account including: (A) mineral dissolution and precipitation reactions, (B) homogeneous reactions within the aqueous phase, (C) surface complexation reactions, (D) ion exchange reactions, (E) exchanges between the gaseous and aqueous phases, and (F) homogeneous and heterogeneous reactions controlled by microorganisms. Flow in and out of each cell is governed by Darcy's law and the evolution of geochemical species is described through mass balance equations.

Since their development in the 1980s, RTM has been widely used to understand biogeochemical systems such as carbon sequestration (Xu et al., 2011; Brunet et al., 2013), chemical weathering and soil formation (Maher et al., 2009; Maher, 2011; Goddéris et al., 2013; Lawrence et al., 2014) and environmental bioremediation (Fang et al., 2009; Bao et al., 2014). They have also been used in a variety of scales including single pores, continuum and field to catchment scales (Steefel et al., 2015). The most commonly used reactive transport continuum-based codes include PHREEQC (Parkhurst and Appelo, 1999), HYDROGEOCHEM (Yeh and Tripathi, 1991), Crunchflow (Steefel and Lasaga, 1994) or Min3p (Mayer et al., 2002). They are typically used to describe the biogeochemical reactions that occur when an aqueous solution percolates through a porous medium such as a soil (Steefel et al., 2015; Li et al., 2017). Of note, models that fully integrate meteorological and climatic processes as well as interactions with vegetation are not available yet (Li et al., 2017).

## 2.4 Gaps in knowledge

First and foremost, an important limitation in ESW studies is the definition of solid phases weathering rates. High discrepancies between field experiments and laboratory measurements bring forward the impossibility to account for the manifold parameters influencing weathering rates such as the freshness and surface area of the reacting rock material, variations in soil solution composition and hydraulic properties, and the influence of biological activity (Brantley et al., 2008, Hartmann et al., 2009). How these factors will modulate through time the rate of chemical breakdown of the silicate rock material applied to planted soils with varying chemical, physical and biological properties, and under different climates, is unknown. Answering this outstanding question is critical for assessing the viability of terrestrial ESW as a NET and for

planning its implementation in croplands within the next few decades.

Furthermore, repeated addition of finely ground silicate rock/minerals may modify the soil texture, the proportion of sand-, silt- and clay-sized particles. Precipitation of secondary solid phases (e.g., clay minerals, carbonates, aluminium and iron (oxy)hydroxides, poorly crystallised aluminosilicates) in response to silicate weathering may similarly alter soil texture. It may also affect particle aggregation processes and therefore soil structure (i.e. the arrangement of individual soil particles – sand, silt and clay – into larger aggregates). Since texture and structure control the retention and flow of water in soil (Hillel, 1998), changes in these properties will alter water-rock/mineral interactions and water residence time and flow (Maher, 2011), with feedback on the silicate weathering rate, chemical element release, plant nutrient cycle and perhaps crop growth (Beerling et al., 2018). However, research on amending agricultural soils with silicate rocks/minerals is still patchy and even partly contradictory. New studies are urgently needed to fully ascertain the short- and long-term impacts of intentional silicate amendment on element biogeochemical cycles in the soil-plant system.

Poorly crystallised aluminosilicates (allophanes/imogolite) may precipitate in crop soils subjected to repeated silicate rock (in particular basalt) amendments (Crovisier et al., 1992). This raises an important question about the long-term efficacy of ESW because the formation of these compounds will hinder chemical weathering of powdered rock/mineral on soils reactions (Brantley et al., 2008; Beerling et al., 2020). Additionally, the build-up of "foreign" allophanes/imogolite (and also iron (oxy)hydroxides) could have a profound effect on the capacity of the soil matrix to exchange/retain ions, including essential plant nutrients (Harsh et al., 2002). On the other hand, newly-formed secondary solid phases can protect soil organic matter from microbial decomposition, thereby favouring organic carbon storage (Basile-Doelsch et al., 2020), i.e. a co-benefit of ESW both in terms of climate change and agricultural soil erosion (Smith et al., 2019).

Finally, biotic processes can induce feedback and play an important role in increasing $P_{CO_2}$ in the soil, which enhances weathering rates. These processes are poorly constrained and seldom included in studies as they are mostly discussed qualitatively. Following, Goll et al. (2021), biotic pathways could contribute up to 40-58% of the global CDR of ESW.

Only a couple of studies have used RTM to simulate the weathering of a silicate (basalt) powder added to soil (e.g. Beerling et al., 2020; Kelland et al., 2020; Lewis et al, 2021; Kantzas et al., 2022), but these suffer from important limitations. Notably, weathering is approached as a set of reactions isolated from the soil matrix itself. This neglects changes in the composition of the percolating soil solution as it constantly readjusts to the local physico-chemical conditions imparted by mineral dissolution/precipitation, ion exchange and surface reactions, and biologically-mediated $CO_2$ production. Another flaw is that allophanes are ignored in the secondary solid phases assemblage that may form upon basalt weathering. However, constraining the stability of these solid phases is essential as their formation may strongly impact weathering kinetics, and hence atmospheric $CO_2$ consumption (Brantley et al., 2008).

## 2.5 Research objectives

The deployment of ESW, alongside other strategies, over several decades is increasingly advocated in order to rapidly limit global warming and the dangerous temperature rise (Schuiling

and Krijgsman, 2006; Hartmann et al., 2013; Strefler et al., 2018; Canadell et al., 2021; IPCC, 2022a). However, the efficacy of ESW to remove CO2 from the atmosphere remains uncertain and its potential side effects are unconstrained. The technology is also brought forward for its suspected beneficial effects on soil fertility and crop productivity, but the results from existing studies are insufficient to confirm this claim. In addition, various modalities for implementing ESW are proposed; for example, some studies recommend adding a silicate powder as a thin layer to the soil surface (e.g., Beerling et al., 2020), whereas others advocate that the material should be incorporated into the plough mixing depth (Kelland et al., 2020; Lewis et al., 2021; Vienne et al., 2022). Similarly, the type of silicate to be used is still debated. Olivine was initially regarded as the mineral of choice for ESW, but now basalt is increasingly investigated as it may provide increased co-benefits to agriculture despite a lower carbon sequestration potential.

Clearly, efforts to provide a detailed assessment of the impact of ESW – and its different modalities – on weathering rates (and thus, CDR potential) and various soil properties are urgently needed. The general research objective of my master dissertation aims to contribute to address these issues. To do so, a hydrogeochemical modelling approach is adopted to predict the temporal evolution of weathering rates and $CO_2$ removal in a soil subjected to ESW. Different silicate application modalities are simulated in the model. We use the computer code CrunchFlow, an open-access and robust reactive-transport model, to perform the 1-D simulations.

The specific research objectives are as follows:

- (i) to model the effects of one and 30 annual applications of olivine and basalt on the physical and chemical properties of a highly weathered soil (Oxisol);
- (ii) to estimate the potential annual CDR and its temporal evolution after a single addition of basalt and olivine;
- (iii) to compare the influence of the application mode and the choice of silicate material on soil properties and potential CDR.

# 3 Material and methods

## 3.1 General approach

Here, model simulations are conducted with the software package CrunchFlow developed by Steefel and co-authors for simulating multi-component multi-dimensional reactive transport in porous media (Steefel and Lasaga, 1994). It has been used to investigate a variety of problems in the earth and environmental sciences (Steefel et al., 2015) such as chemical weathering (Perez-Fodich and Derry, 2019), contaminant reactive transport (Wanner et al., 2012) or carbon fluxes (Torres, 2014).

Several 1-D simulations for a 1-meter long soil profile, discretized as a series of 1000 cells of 1 mm length, are set up over decadal to century timescale. As ESW presents the biggest potential for warm and humid climatic conditions (Moosdorf et al., 2014; Strefler et al., 2018), this study focuses on the amendment of silicate material to a highly weathered soil, i.e. an Oxisol. These soils are predominantly located in the intertropical regions of the world (Van Wambeke et al., 1974). The coincidence between cropland areas in warm humid climates (Strefler et al., 2018) (Figure A.2), and worldwide Oxisol repartition (Figure A.3), suggests that these soils are interesting targets for ESW deployment. Moreover, with growing production requirements in the future, croplands are expected to expand (FAO, 2012) and the shortage of arable land means that less fertile sites will have to be found in the tropics for cultivation (Kantola et al., 2017). Oxisols being highly depleted, ESW could ameliorate their fertility and thus crop production.

Some studies recommend adding a silicate powder as a thin layer to the soil surface (e.g., Beerling et al., 2020), whereas others advocate that the material should be incorporated into the plough mixing depth (Kelland et al., 2020; Lewis et al., 2021; Vienne et al., 2022). The pros and cons of the two modalities have never been assessed. In order to contrast the behaviour of olivine and basalt in terms of their efficiency for $CO_2$ removal and potential effects on general soil properties, we tested the two forms of silicate addition in our simulations. The mixing soil depth was set at 20 cm, a common plough mixing depth (Kelland et al., 2020; Vienne et al., 2022). For each application modality, two silicate application rates were considered : (i) a single addition of 5000 g $m^{-2}$ (50 t $ha^{-1}$) of crushed silicate to the soil, i.e. an amount commonly referred to as a benchmark in ESW studies (Kelland et al., 2020; Goll et al., 2021, Lewis et al., 2021; Vienne et al., 2022) and (ii) a single addition of 150000 g $m^{-2}$ (1500 t $ha^{-1}$) of crushed silicates corresponding to 5000 g $m^{-2}$ added annually over 30 years. This duration was chosen because to have a significant effect on CDR, ESW should be deployed over several decades. Although the second scenario will not take place in the field, we deem it conceptually reasonable because our simulation results showed that the initial abundance of olivine and basalt decreases by less than one percent after one year (see section 5.1). In other words, most of the silicate material added to the soil will remain until the next amendment one year later. Thus, if ESW is pursued during 30 years, this would be equivalent to adding 150000 g $m^{-2}$ one time.

In summary, we performed the CrunchFlow simulations assuming four scenarios of powdered silicate application, with each scenario repeated twice for assessing the potential effect of ion exchange (noted here *"CEC"*) on soil mineralogy and solution composition : (i) M1/M1$_{CEC}$ - Oxisol with an overlying olivine layer; (ii) M2/M2$_{CEC}$ - Oxisol with olivine incorporated into the 0-20 cm top soil layer; (iii) M3/M3$_{CEC}$ - Oxisol with an overlying basalt layer and (iv)

M4/M4$_{CEC}$ - Oxisol with basalt incorporated into the 0-20 cm top soil layer. For each scenario, both application rates (5000 and 150000 g m$^{-2}$) are tested. The simulations for the application of 5000 g m$^{-2}$ are referred to as L-olivine and L-basalt for the low application rate, whereas H-olivine and H-basalt allude to high application rate simulations corresponding to 150000 g m$^{-2}$. The different model setups are detailed in Table 1.

Table 1: Summary of the different model setups. Each silicate amendment is simulated according to two modes and rates of application. For each simulation, a sensitivity analysis was performed regarding the solubility constant of allophanes.

| | Model M1/M1$_{CEC}$ | Model M2/M2$_{CEC}$ | Model M3/M3$_{CEC}$ | Model M4/M4$_{CEC}$ |
|---|---|---|---|---|
| Infiltrating solution composition | Rainfall (Table 5) | | | |
| $CO_2$ treatment | Fluid at equilibrium with atmospheric $CO_2$ at 414.24 ppmv | | | |
| Silicate amendment | Olivine | | Basalt | |
| Distribution method | Overlying layer | 0-20 cm | Overlying layer | 0-20 cm |
| Application rate [t ha$^{-1}$] | 50 (L) - 1500 (H) | 50 (L) - 1500 (H) | 50 (L) - 1500 (H) | 50 (L) - 1500 (H) |
| Allophane solubility constant (log K) | 10.96 - 7.02 | 10.96 - 7.02 | 10.96 - 7.02 | 10.96 - 7.02 |
| Basaltic rock composition | N/A | | Kelland et al. (2020) | |

## 3.2 Model parameters

Several parameters (Figure 7) need to be specified in order to start the stimulations in CrunchFlow. These includes the temperature of the system to be modelled, initial pH values of the infiltrating and soil solutions, soil porosity, soil mineralogical composition (including volume percentages (V%.) and mineral's SSA), aqueous chemistry, initial soil CEC (when this option is chosen), silicate (of known composition) application rate and relevant thermodynamic and kinetic data. The initial pH of the infiltrating and soil solution are computed by running presimulations tests. The pH calculated for the infiltrating solution is 8 and 8.3 when olivine and basalt, respectively, are added to the soil surface. The soil solution of the Oxisol has a pH value of 5.63. All simulations are performed at a temperature of 25 °C.

### 3.2.1 Bulk and mineralogical characteristics of the Oxisol and ground silicates

Oxisols

Oxisols are characterised by a low bulk density ranging between 1.0 and 1.3 g cm$^{-3}$ (Van Wambeke, 1974; El Swaify, 1980; Buol and Eswaran, 1999). According to equation 3, porosity ($Pt$) can be computed using soil bulk density ($Pb$) and mean particles density ($Pd$):

$$Pt = 1 - \frac{Pb}{Pd} \tag{3}$$

Using the Oxisol's mineralogical composition calculated in Alves and Otomoso (2009), mean particles density is set to 3.29 g cm$^{-3}$. Porosity is thus initially set to 65%, consistent with usual high porosity of Oxisols (Buol and Eswaran, 1999). The Oxisol quantitative mineralogical composition (Table 3) is based on the particle size distribution as stated in Buol and Eswaran (1999) with 60, 20 and 20%wt. of clay-, silt- and sand-sized particles, respectively. The silt and sand fractions in Oxisols are dominantly comprised of quartz grains (Herbillon, 1988). The mineralogical composition of the Oxisol's clay fraction corresponds to that determined by Alves and Otomoso (2009) for a Brazilian soil. The main minerals identified are kaolinite ($Al_2Si_2O_5(OH)_4$),

goethite (FeO(OH)), gibbsite ($Al(OH)_3$) and hematite ($Fe_2O_3$), consistent with the composition of a typical Oxisol (Herbillon, 1988; Buol and Eswaran, 1999). Due to the absence of hematite in the database, it is not included in the Oxisol final composition. Other minor solid phases such as anatase ($TiO_2$), rutile ($TiO_2$) and vermiculite ($Mg_{1.8}Fe_{0.9}AlSiO_{10}(OH)_2{\cdot}4H_2O$) are neglected in our simulations as these are unlikely to influence the results significantly.

### Olivine and basalt

The powdered olivine and basalt materials used as silicate amendments for simulating ESW in CrunchFlow are either added to the Oxisol surface or incorporated into the 0-20 cm top soil layer. In the first case, the porosity of the silicate deposit is set to 50%, a value representative of that measured for natural tephra deposits with comparable grain size characteristics (Biass et al., 2016). The silicate layer thickness (Table 2) is obtained by dividing the applied quantity (i.e. 50 and 1500 t) by the amendment density and the chosen porosity to obtain the volume of the amendment. In the second case, when the silicate powder is mixed within the top soil, we corrected the Oxisol's initial porosity by accounting for the volume occupied by the amendment. The initial volume percentage of the amendment is computed by dividing the amendment volume by the volume in which it is incorporated (0.2 $m^3$) (Table 2) .

Table 2: Layer thickness, when applied at the surface of the profile, and initial volume occupied and resulting Oxisol's porosity, when incorporated in the topsoil, for both silicate amendments and application rates.

| | | Surface | Incorporation | |
|---|---|---|---|---|
| Amendment | Application rate [t/ha] | Layer thickness [mm] | %V. occupied | Oxisol porosity [%] |
| Olivine | 50 | 3 | 0.7692 | 64.23 |
| | 1500 | 92 | 23.08 | 41.92 |
| Basalt | 50 | 3 | 0.8621 | 64.14 |
| | 1500 | 106 | 25.86 | 39.14 |

In our modelling, olivine corresponds to a Mg-rich and Fe-poor composition (i.e. 80% of forserite and 20% of fayalite). This choice is motivated by the thermodynamic and kinetic information available in CrunchFlow's database. The basalt composition (Table 3) is described by Kelland et al. (2020) for a rock sourced from the Cascade Mountain Range, Oregon, USA. Owing to their low contents compared to the other solid phases, and in order to simplify the model, ilmenite and apatite are excluded from the basalt composition. The alkali-feldspar ($K_{0.41}Na_{0.56}Ca_{0.03}Al_{1.03}Si_{2.97}O_8$) is replaced by a K-feldspar as this is the only feldspar type for which a full thermodynamic and kinetic description is available in CrunchFlow. Kelland et al. (2020) reports the presence of montmorillonite in the basalt, but we discarded this phase as it is a clay mineral produced by weathering and it occurs in minor contents.

Table 3: Description of the Oxisol and basalt compositions and initial mineral abundances used in the CrunchFlow simulations.

| | Mineral | Chemical formula | Layer | V%. Incorporation | |
|---|---|---|---|---|---|
| | | | | 50 t $ha^{-1}$ | 1500 t $ha^{-1}$ |
| Oxisol | Kaolinite | $Al_2Si_2O_5(OH)_4$ | | 10.98 | |
| | Quartz | $SiO_{2(s)}$ | | 15.98 | |
| | Gibbsite | $Al(OH)_3$ | | 6.450 | |
| | Goethite | $FeO(OH)$ | | 1.670 | |
| Basalt | Plagioclase | $Ca_{0.5}Na_{0.5}Al_{1.5}Si_{2.5}O_8$ | 15.29 | 0.2637 | 7.910 |
| | K-feldspar | $KAl_{1.03}Si_{0.97}O_8$ | 17.18 | 0.2963 | 8.888 |
| | Diopside | $CaMg_{0.7}Al_{0.6}Si_{1.7}O_6$ | 3.737 | 0.0644 | 1.933 |
| | Basaltic glass | $Na_{0.13}Ca_{0.08}Mg_{0.05}K_{0.10}Fe_{0.12}Al_{0.26}SiO_{2.86}$ | 13.10 | 0.2259 | 6.778 |
| | Olivine | $(Mg_{0.8}Fe_{0.2})_2SiO_4$ | 0.3076 | 0.0053 | 0.1590 |
| | Quartz | $SiO_{2(s)}$ | 0.2304 | 0.0040 | 0.1192 |
| | Calcite | $CaCO_3$ | 0.1465 | 0.0025 | 0.0758 |

The secondary solid phases allowed to precipitate in response to weathering of the silicate amendments are allophanes ($Al_2O_3(SiO_2)_{1.22}(H_2O)_{2.5}$), halloysite ($Al_2Si_2O_5(OH)_4$), amorphous silica ($Sio_{2(am)}$) and smectites ($K_{0.04}Ca_{0.5}$ $(Al_{2.8}Fe_{0.53}Mg_{0.7})(Si_{7.65}Al_{0.35})O_{20}(OH)_4$). These are the main solid products that can be formed in various proportions during weathering of silicates (Stefánsson and Gíslason, 2001; Aradottir et al., 2012). Smectite with a low Fe and Mg content is chosen so that saturation may be reached even at relatively lower concentrations of Fe and Mg in solution. The initial mineral abundances of the secondary solid phases in the soils are set to 0.0001% to allow for their precipitation, as recommended in CrunchFlow.

### 3.2.2 Thermodynamic properties

The quality of modelling results heavily depends on the quality of the thermodynamic database used (Oelkers et al., 2009; Aradottir et al., 2012). Many databases are available and it is essential to remain consistent between the selected thermodynamic database and each of the chosen solid phase throughout all simulations (Aradottir et al., 2012; Perez-Fodich and Derry, 2019). The main database used in this study is the Lawrence Livermore National Laboratory (LLNL) database, which regroups thermodynamic constants for aqueous, gaseous and solid species derived from the EQ3/6 package (Wollery, 1992). The latest is built upon the SUPCRT92 database (Aradottir et al., 2012). Table 4 summarises the solubility constants of reacting solid phases at 25 °C.

The chemical composition of the basaltic glass (the amorphous solid phase of the basaltic rock) is approximated using Oelkers and Gíslason (2001)'s composition: $SiAl_{0.36}Fe_{0.19}Mg_{0.28}Ca_{0.26}Na_{0.08}$ $K_{0.008}O_{3.31}$. The solubility of the aluminosilicate glass depends on its specific chemical composition, hence there is no absolute value for it. According to Paul (1977)'s theoretical approach, glass can be viewed as a mixture of oxides, of known solubilities (Table A.1). The solubility constant is then given by (Equation 4):

$$log(K)_{glass} = \sum_i log(K_i) + \sum_i x_i log(x_i) \tag{4}$$

where $x_i$ is the mole fraction of an oxide of the mixture and $K_i$ its solubility product. A similar approach for computing the solubility of aluminosilicate glass has been adopted in previous

studies (Bourcier et al., 1999; Leturcq et al., 1999; Techer et al., 2001; Aradottir et al., 2012).

### 3.2.3 Dissolution and precipitation kinetics

Mineral dissolution and precipitation kinetics rate laws are based on the transition state theory (TST) as defined in Lasaga (1981). The theory states that the reaction path includes a transition state, named the activated complex, at which the potential energy reaches its maximum value. The reaction rate is limited by the number of activated complexes formed and the rate at which they are decomposed to reach the final product (Aagard and Helgeson, 1982). The TST links the kinetics and thermodynamics driving force of geochemical processes by accounting for the effect of chemical affinity and restrictions imposed by chemical equilibrium between the activated complex and the reactants on the reaction rate (Aagaard and Helgeson, 1982; Yang and Steefel, 2008). In CrunchFlow, the rate law,is governed by Equations 5 and 6.

$$r = A_m k_m exp\left[\frac{-E_a}{RT}\right] \prod a_i^{n_i} \left[1 - exp(m_2 g)\right] \tag{5}$$

$$g \equiv \Delta G_r = RTln\left[\frac{Q}{K_{eq}}\right] \tag{6}$$

where $r$ [mol m$^2$ s$^{-1}$] is the net global reaction rate, $A_m$ [m$^2$ m$^{-3}$ porous media] is the mineral surface area, $k_m$ [mol m$^2$ s$^{-1}$] is the rate constant, $E_a$ [kcal mol$^{-1}$] is the activation energy, $R$ is the gas constant, $T$ [K] is the temperature, and $\prod a_i^{n_i}$ is the product of the activities of different species in the system raised to the power n$_i$. This term incorporates the inhibitory or catalysing effect of various ions in the solution on the dissolution rate and operates when the reaction is far from equilibrium (Aagaard and Helgeson, 1982; Steefel, 2008). $m_2$ is known as Temkin's average stoichiometric number, the ratio of the destruction rate of the activated complex engaged in the rate-limiting reaction step with the rate of the overall dissolution rate.

In equation 5, $g$ integrates the influence of chemical affinity on the reaction rate, as expressed via equation 6, where $\Delta G_r$ [kJ mol$^{-1}$] is the Gibbs free energy of the total reaction, $Q$ is the ion activity product and $K_{eq}$ is the equilibrium constant. Chemical affinity is responsible for slowing down aluminosilicates dissolution rate with time. When a silicate dissolves, a silica-rich weathered layer, probably amorphous silica (Feng, 1993; Wolff-Boenisch et al., 2004; Ma et al., 2017), may form on the reactive surface (Cailleteau et al., 2008). This phenomenon creates a diffusion barrier which reduces the affinity for dissolution and stabilises the solid phase (Cailleteau et al., 2008). In theory, chemical affinity influence is particularly important when approaching saturation with respect to precipitation of a secondary solid phase (Ma et al., 2017). The effect of affinity on dissolution rate may be significant in the case of volcanic glass. Chemical affinity is then defined in relation to the secondary phase (typically amorphous silica; Gin et al., 2016) that would precipitate upon dissolution. In Equation 5, the coefficient m2 is assumed to be equal to 1 for basaltic glass. Equation 7 illustrates the overall approach adopted for calculating the dissolution rate of basaltic glass (Gíslason and Oelkers, 2003), highlighting the promoting and inhibiting effects on the reaction rate of $H^+$ and $Al^{3+}$. However, Crunchflow only allows to define chemical affinity with respect to the solid phase dissolving, yet, in the case of volcanic glass, it cannot re-precipitate. The influence of chemical affinity on basaltic glass weathering rate thus is not taken into account.

$$r_{glass} = A_m k_m exp\left[-\frac{E_A}{RT}\right] \frac{a_{H^+}}{a_{Al^{3+}}^{-0.333}} \tag{7}$$

Dissolution rate constants are either compiled in Palandri and Kharaka (2004) or come from Kelland et al. (2020) for the basaltic rock components. Dissolution rate for olivine (forsterite endmember) originates from Pokrovsky and Schott (2000). Labradorite rate constant is used for plagioclase because its stoichiometry is closest to that documented in Kelland et al. (2020). Kinetics data for the precipitation of allophanes have not been reported in the literature and are assumed to be equivalent to $Si0_{2(am)}$ precipitation rate, as suggested by Perez-Fodich and Derry (2019).

The SSA of primary and secondary solid phases must also be defined in CrunchFlow. Using SSA values reported in the scientific literature resulted in numerical instabilities while performing the simulations and therefore, we followed Perez-Fodich and Derry (2019)'s approach where relatively low SSA values of 0.1 and 1 $m^2$ $g^{-1}$ are used for the primary and secondary solid phases, respectively, present in the system. We note that SSA of secondary solid phases can be several orders of magnitude higher than the chosen value. However, adjusting SSA produces the same effect on reaction rate as modifying the rate constant (Equation 5; Perez-Fodich and Derry, 2019). Thus, in order to limit numerical instabilities during computation, it is more appropriate to change the rate constants when it is necessary to compensate for the low SSA values. The decision is made *a posteriori*, i.e. based on an initial simulation and assessment of the geochemical meaning of the model outputs.

Table 4: Mineral dissolution reactions, specific surface area (SSA), thermodynamic equilibrium constants and kinetic rate constants used in the models.

| Mineral | Dissolution Reaction | SSA ($m^2\ g^{-1}$) | log $K_{m,eq}$ | log $k_m$ (mol $m^{-2}\ s^{-1}$) |
|---|---|---|---|---|
| Olivine ($Fo_{80}Fa_{20}$) | $(Mg_{0.8}Fe_{0.2})_2SiO_4 + 4\ H^+ \rightleftharpoons 1.6Mg^{2+} + 0.4\ Fe^{2+} + SiO_{2(aq)} + 2H_2O$ | 0.1 | 26.72[a] | -12.47[b] |
| Plagioclase ($An_{0.5}Ab_{0.5}$) | $Ca_{0.5}Na_{0.5}Al_{1.5}Si_{2.5}\ O_8 + 6\ H^+ \rightleftharpoons 0.5\ Ca^{2+} + 0.5\ Na^+ + 1.5\ Al^{3+} + 2.5\ SiO_{2(aq)} + 3\ H_2O$ | 0.1 | -20.11[c] | -10.91[d] |
| K-feldspar | $KAl_{1.03}Si_{0.97}O_8 + 12.12\ H^+ \rightleftharpoons K^+ + 1.03\ Al^{3+} + 0.97\ SiO_{2(aq)} + 6.06\ H_2O$ | 0.1 | -0.2753[e] | -12.41[f] |
| Diopside | $CaMg_{0.7}Al_{0.6}Si_{1.7}O_6 + 5.2\ H^+ \rightleftharpoons Ca^{2+} + 0.7\ Mg^{2+} + 0.6\ Al^{3+} + 1.7\ SiO_{2(aq)} + 2.6\ H_2O$ | 0.1 | 20.96[e] | -11.11[d] |
| Basaltic glass | $Na_{0.13}Ca_{0.08}Mg_{0.05}K_{0.10}Fe_{0.12}Al_{0.26}SiO_{2.86} + 1.72\ H^+ \rightleftharpoons 0.13\ Na^+ + 0.08\ Ca^{2+} + 0.05\ Mg^{2+} + 0.1\ K^+ + 0.12\ Fe^{2+} + 0.26\ Al^{3+} + SiO_{2(aq)} + 0.86\ H_2O$ | 1 | 5.31[g] | -14.97[h] |
| Calcite | $CaCO_3 \rightleftharpoons Ca^{2+} + CO_3^{2-}$ | 0.1 | 1.85[i] | -6.19[h] |
| Quartz | $SiO_{2(s)} \rightleftharpoons SiO_{2(aq)}$ | 0.1 | -3.75[j] | -13.99[d] |
| Kaolinite | $Al_2Si_2O_5(OH)_4 + 6\ H^+ \rightleftharpoons 2\ Al^{3+} + 2\ SiO_2 + 5\ H_2O$ | 1 | 6.81[i] | -13.18[d] |
| Gibbsite | $Al(OH)_3 + 3\ H^+ \rightleftharpoons Al^{3+} + 3\ H_2O$ | 1 | 7.76[e] | -11.5[d] |
| Goethite | $FeO(OH) + 3\ H^+ \rightleftharpoons Fe^{3+} + 2H_2O$ | 1 | 0.53[k] | -7.94[d] |
| Allophane | $Al_2O_3(SiO_2)_{1.22}(H_2O)_{2.5} + 6\ H^+ \rightleftharpoons 2\ Al^{3+} + 1.22\ SiO_{2(aq)} + 5\ H_2O$ | 1 | 10.96[l] | -12.23[m] |
| Halloysite | $Al_2Si_2O_5(OH)_4 + 6\ H^+ \rightleftharpoons 2\ Al^{3+} + 2\ SiO_{2(aq)} + 5\ H_2O$ | 1 | 10.32[n] | -12.89[h] |
| Smectite | $K_{0.04}Ca_{0.5}(Al_{2.8}Fe_{0.53}Mg_{0.7})(Si_{7.65}Al_{0.35})O_{20}(OH)_4 + 28.7\ H^+ \rightleftharpoons 0.04\ K^+ + 0.5\ Ca^{2+} + 3.15\ Al^{3+} + 0.53\ Fe^{2+} + 0.7\ Mg^{2+} + 7.65\ SiO_{2(aq)} + 16.35\ H_2O$ | 1 | 11.04[e] | -12.78[d] |
| Amorphous silica | $SiO_{2(am)} \rightleftharpoons SiO_{2(aq)}$ | 1 | -2.71[o] | -12.23[d] |

[a] Retrieved from Steffánsson, 2001.
[b] Retrieved from Povkrosky and Schott, 2000.
[c] Retrieved from Arnorsson and Stefánsson, 1999.
[d] Retrieved from Palandri and Kharaka, 2004.
[e] Default value from the LLNL database, based on the EQ3/6 package (Wollery, 1992).
[f] Retrieved from Kelland et al. (2020), based on data from Palandri and Kharaka, 2004.
[g] Retrieved from Aradottir et al. (2012), calculated following Paul (1997) theoretical approach.
[h] Default value from CrunchFlow.
[i] Calculated with SUPCRT92 package with data from Holland and Powell, 1998.
[j] Derived from Gunnarsson and Arnórsson (2000).
[k] Helgeson, 1978, derived from SUPCRT92 thermodynamic dataset (Johnson et al., 1992).
[l] Derived from Aradottir et al. (2012) with data from Stefánsson and Gíslason, 2001.
[m] Assumed to be equivalent to $SiO_{2(am)}$ dissolution rate (Perez-Fodich and Derry, 2019).
[n] Retrieved from THERMODDEM thermodynamic database (Blanc, 2012).
[o] Retrieved from the SUPCRTBL software package, an extended and modified thermodynamic dataset of SUPCRT92 (Zimmer et al., 2016).

### 3.2.4 Aqueous chemistry

At the time of writing, a typical and complete rainwater composition was not available for the region where Oxisols occur. In general, important chemical species (such as $Al^{3+}$, $SiO_2$, $Fe^{2+}$ and $Fe^{3+}$) required in CrunchFlow for describing the solution infiltrating the soil are missing. The rainwater composition used in all our simulations (Table 5) originates from White et al. (2009), who investigated weathering of a soil chronosequence in a Mediterranean climate. Similar to Perez-Fodich and Derry (2019), the concentrations reported by White et al. (2009) were divided by a factor of ten in order to match better the typical rainfall chemistry of southeast Brazil (from where our Oxisol originates) (Mimura et al., 2016).

Carbon dioxide concentration of the aqueous solution is assumed to be at equilibrium with a mean atmospheric concentration of 414.24 ppm (as in 2020) (National Oceanic and Atmospheric administration [NOAA]). The rainwater pH is computed using this concentration and the carbonate equilibrium system. In our simulations, the dissolved $CO_2$ concentration in the soil solution is assumed to be constant. In doing so, we ignore the dynamic inputs from microbial respiration of organic matter (Perez-Fodich and Derry, 2019). This is a limitation of CrunchFlow, which is discussed later in our document (see section 5.6). Oxygen in the infiltrating solution is considered at equilibrium with its partial pressure of 20% in the atmosphere, i.e. aerobic conditions are always maintained in the system.

Table 5: Aqueous chemistry and pH of the infiltrating rainfall used as initial and boundary conditions in the simulations (White et al., 2009; Perez-Fodich and Derry, 2019) and comparison with available rainwater chemistry for Southeast Brazil (Mimura et al., 2016)

| Species | Concentration (mol $L^{-1}$) Diluted by 10 x from White et al. (2009) as in Perez-Fodich and Derry (2019) | Concentration (mol $L^{-1}$) from Mimura et al. (2016) |
|---|---|---|
| $SiO_2$ (aq) | $9.0 \times 10^{-8}$ | N/A |
| $Al^{3+}$ | $2.0 \times 10^{-8}$ | N/A |
| $Ca^{2+}$ | $9.0 \times 10^{-6}$ | $39.8 \times 10^{-6}$ |
| $Mg^{2+}$ | $6.8 \times 10^{-6}$ | $18.9 \times 10^{-6}$ |
| $Na^{+}$ | $4.2 \times 10^{-5}$ | $34.3 \times 10^{-6}$ |
| $K^{+}$ | $1.6 \times 10^{-5}$ | $19.7 \times 10^{-6}$ |
| $Fe^{3+}$ | $1.0 \times 10^{-8}$ | N/A |
| $Fe^{2+}$ | $1.0 \times 10^{-6}$ | N/A |
| $Cl^{-}$ | $4.6 \times 10^{-5}$ | $23.6 \times 10^{-6}$ |
| $SO_4^{2-}$ | $1.6 \times 10^{-5}$ | $8.0 \times 10^{-6}$ |
| $NO_3^{-}$ | $1.0 \times 10^{-5}$ | $28.7 \times 10^{-6}$ |
| pH | 5.63 | 6.22 |

### 3.2.5 Ion exchange reactions and cation exchange capacity calculation

Ion exchange reactions in soils refer to ions (most often cations) exchanging between the surface of the exchange complex (or "exchanger", as represented by clay mineral surfaces and organic matter) and the soil solution. These reactions are rapid and reversible, i.e. they are at equilibrium and no kinetic considerations are required. An ion exchange reaction, expressed in the generic form in Equation 8, can be characterised with an equilibrium constant, $K_{eq}$ (Equation 9; Vanselow, 1932).

$$vACl_u(aq) + uBX_v(s) \rightleftharpoons uBCl_v(aq) + vAX_u(s) \tag{8}$$

$$K_{eq} = \frac{(BCl_v)^u (AX_u)^v}{(ACl_u)^v (BX_v)^u} \tag{9}$$

where $X$ designates the exchange site occupied by the cations $A^{u+}$ and $B^{v+}$ and the parentheses represent thermodynamic activities.

Ion exchange reactions are implemented in CrunchFlow either by listing specific exchangers or by considering exchange reactions on the bulk material (Steefel, 2008). As the majority of the soil's bulk phases are oxides, hydroxides or quartz, which contribute only slightly to the exchange capacity, we chose to specify exchangers. Thus, an equilibrium constant is required for each cation-solid phase pair. These constants are difficult to determine and available only for exchangers smectites and kaolinite, with an initial CEC of 9 and 115 meq 100 $g^{-1}$ mineral, respectively (Carroll, 1959). CrunchFlow then computes the soil solution chemistry taking into account ion exchange. Cation exchange capacity is computed as the sum of the charge equivalent concentrations of the cations present on the different exchange sites (i.e. smectites and kaolinite) (Equation 10; Voegelin et al., 2020).

$$CEC = \sum_i \sum_M z_M q(i)_M \tag{10}$$

where $z_M$ charge of cation $M$ and $q(i)$ is the concentration of cation $M$ on the exchange site $i$.

### 3.2.6 Model sensitivity analyses

A sensitivity analysis is performed regarding the solubility constant of allophanes. As opposed to our simulations first results, allophanes are expected to be the first secondary solid phase to precipitate during weathering of a basaltic glass (Crovisier et al., 1992). This difference could come from thermodynamic constant for the dissolution of allophanes as they range over several orders of magnitude (Lumsdon and Farmer, 1995; Su and Harsh, 1998; Stefánsson and Gíslason, 2001). Allophanes composition, which depends on the environment in which they are found and is characterised by the ratio Al:Si, influence their solubility. Consequently, allophanes of different composition, and whose solubility is constrained by different thermodynamic constants, can be found in a random Oxisol. To assess the impact of these different solubility constants on the resulting soil and aqueous solution composition, two values are tested. The initial solubility constant (10.96) corresponds to allophanes with a Al:Si ration of 1.64. A solubility constant (log K) of 7.02 is used for the sensitivity analysis, which corresponds to allophanes characterised by a ratio equal to 2 (Lumsdon and Farmer, 1995).

## 3.3 Model formulation

As mentioned in section 3.1, several 1-D simulation over a 1-m column discretized as a series of a thousand 1-mm cells are set up for simulating ESW in the Oxisol. When the silicate (olivine or basalt) is applied to the soil surface, a first series of cells is used to represent the amendment layer, the number of cells corresponding to the layer thickness (Table 2) and Figure 7; all the other cells below describe the Oxisol profile). When the ground silicate is incorporated into the soil (0-20 cm), the 200 first cells consist in a mixture of the amendment and the Oxisol; the

rest of the cells represent the deeper Oxisol properties (Figure 7).

We simulate chemical weathering over a period of one century. The outputs are analysed after one year, to assess the immediate effects of silicate amendment weathering on CDR and soil properties, after five and ten years (short-term), after 25 years (giving the effects by 2050 if ESW were implemented in 2025), 50 years (indicating the remaining effects at the end of the century) and 100 years (long-term).

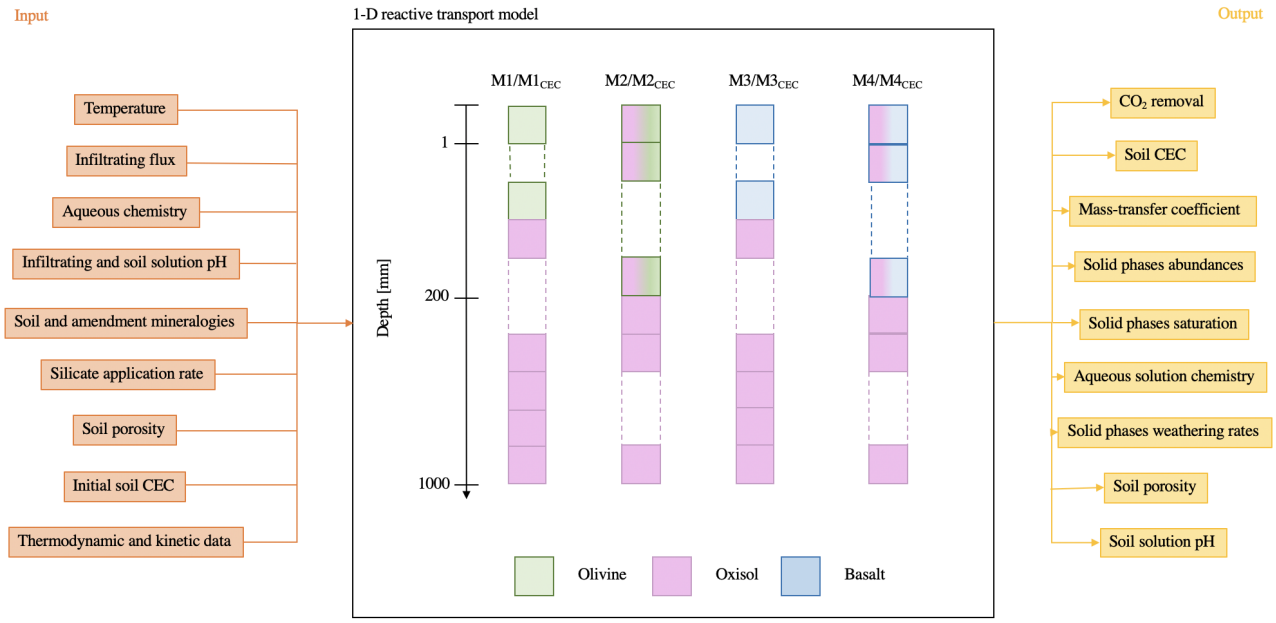


Figure 7: Schematic overview of the input needed (orange) to run the 1-D simulations in CrunchFlow and the output produced (yellow). The 1-D simulations consist in a column of 1000 1-mm cells. When the ground silicate is applied to the soil surface (models M1/M1$_{CEC}$ and M3/M3$_{CEC}$), a first series of cells consists in the amendment (green or blue); the rest of them corresponding to the Oxisol profile (pink). When the ground silicate is incorporated into the 0-20 cm soil layer (M2/M2$_{CEC}$ and M4/M4$_{CEC}$), the 200 first cells represent a mixture of the soil and the amendment (blue-pink or green-pink); the rest of the cells correspond to the Oxisol (pink).

### 3.3.1 Transport

The infiltrating rainwater flux is modelled using a vertical 1-D Darcy flow (Perez-Fodich and Derry, 2019). Rainwater infiltration flux results from a mass balance between rainfall and evapotranspiration (ET). Potential lateral runoff is not considered in CrunchFlow. Rainfall flux and ET values representative of a tropical climate are used. We chose a mean annual precipitation of 2.390 m yr$^{-1}$ (city of Manaus in the Amazon rainforest in northern Brazil) and a ET of 1.369 m yr$^{-1}$, as computed by Werth and Avissar (2004), for the Amazon basin. The resulting infiltrating rainfall flux is equal to 0.9313 m yr$^{-1}$. Precipitations in tropical climates are subject to a strong seasonality, but this is not taken into account in our model. Oxisols are characterised by a large amount of macropores enabling rapid movement of infiltrating rainwater through the profile (Buol and Eswaran, 1999). Thus, although mean annual precipitation is high, the soil is unsaturated and soil humidity is set to 50% in all the simulations.

## 3.4 Calculation of carbon dioxide removal

Annual CDR [g $CO_2$ $m^{-2}$ $yr^{-1}$] by ESW can be computed as the flux of $HCO_3^-$ and $CO_3^{2-}$ that balances the cations released during silicate minerals dissolution, integrated over the entire soil profile (Goddéris et al., 2013). The concentration [mol $L^{-1}$] of both species are summed over the soil weathering profile (1 m) and multiplied by the infiltrating water flux (931.3 L $yr^{-1}$) and the molar mass of $CO_2$ (44.01 g $mol^{-1}$) to obtain the mass of $CO_2$ captured [g $m^{-2}$ $yr^{-1}$]. However, the ocean carbonate equilibrium system reduces the efficiency of CDR through carbonates precipitation and deposition on the ocean floor (Equation 2; Beerling et al., 2020). The magnitude of this effect depends on ocean salinity, temperature and the surface ocean dissolved $CO_2$ concentration (Beerling et al., 2020). As suggested by Renforth (2012), to account for these processes in our CDR calculations, we multiply the annual CDR previously obtained by 0.85. Annual CDR is computed after 1, 5, 10, 25, 50 and 100 yr of weathering to analyse the temporal evolution.

# 4 Results

## 4.1 M1/M1$_{CEC}$ - Oxisol with an overlying olivine layer

### Soil solution pH

The soil solution pH (Figure 8) increases after olivine application. With L-olivine (Figure 8a), soil solution pH rises from an initial value of 5.63 to values close to 5.83 at the bottom (1 m) of the profile 1 yr after olivine application. Continuous water flow for the next 100 yr leads to a slight pH decrease with time along the soil profile (≈5.80 at 1 m depth after 100 yr). The addition of H-olivine to the soil (Figure 8b) results in a larger pH increase (≈+1.5) with values rapidly buffered around pH 7.10 within the topmost 10 cm of soil and regardless of weathering duration. Our results show no significant difference on soil solution pH evolution when including ion exchange reactions in any of the simulations.

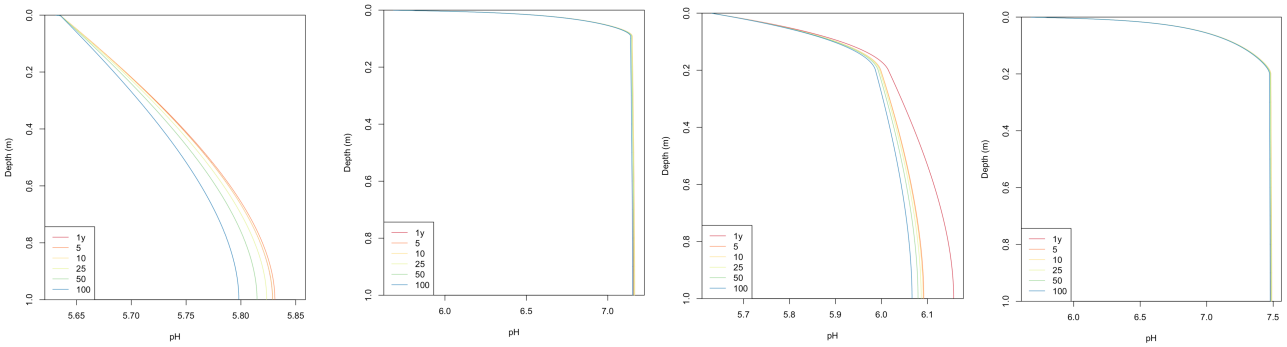


(a) M1/M1$_{CEC}$ (L) (b) M1/M1$_{CEC}$ (H) (c) M2/M2$_{CEC}$ (L) (d) M2/M2$_{CEC}$ (H)

Figure 8: Soil solution pH evolution as a function of depth after a single application of olivine to the soil surface (M1) of 5000 g m$^{-2}$ (8a) and 150000 g m$^{-2}$ (8b); and in the 0-20 cm layer (M2) of 5000 g m$^{-2}$ (8c) and 150000 g m$^{-2}$ (8d). The model results with and without ion exchange (CEC) do not differ.

### Primary and secondary solid phases abundances

Primary and secondary solid phases abundances evolution are not modified by the inclusion of ion exchange reactions in the simulations. The V%. of olivine in the amendment overlying layer (Figure 9) decreases by less than 2% after 100 yr of weathering for both application rates and modes. When 5000 g m$^{-2}$ of olivine is added to the soil (Figure 9a), ≈0.25 V%. of gibbsite precipitates and ≈0.68 V%. of kaolinite dissolves in the first 40 cm after 100 yr. The same observations are made for H-olivine (Figure 9b), with ≈0.2 V%. of gibbsite precipitating and ≈0.4 V%. of kaolinite dissolving between 10 and 20 cm depth. Goethite precipitation (≈2 V%.) occurs in the soil's first 2 mm in both simulations. Allophanes, halloysite, amorphous silica and smectite do not precipitate.

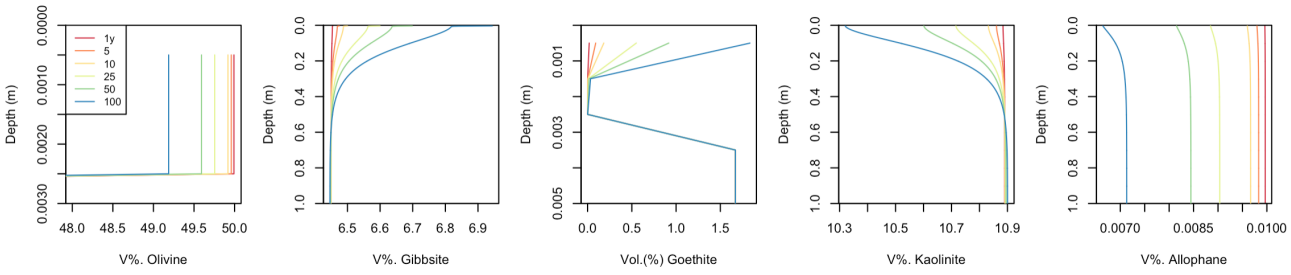


(a) M1/M1$_{CEC}$ (L)

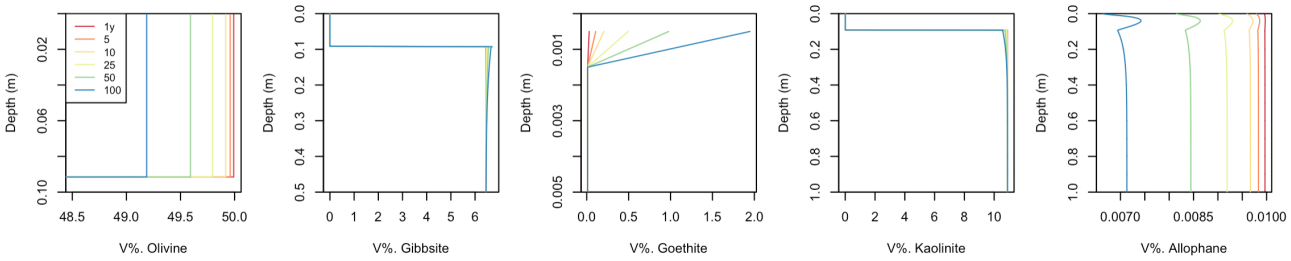


(b) M1/M1$_{CEC}$ (H)

Figure 9: Primary and secondary solid phases V%. evolution with soil depth and weathering duration after a single application of olivine of 5000 g m$^{-2}$ (9a) and 150000 g m$^{-2}$ (9a) to the soil surface (M1). The model results with and without ion exchange (CEC) do not differ.

### Soil porosity

Owing to the dissolution of kaolinite and olivine upon weathering, soil porosity slightly increases (≈+1% in 100 yr) in the amendment layer (Figure A.4). Gibbsite and goethite precipitation does not compensate for the effect of dissolution on soil porosity. Soil porosity remains constant along the rest of the soil profile.

### Aqueous species concentrations

The simulations always predict an increase in all dissolved species compared to the initial composition of rainwater, except for $Al^{3+}$ in the H-olivine scenario (Figure 10). Aqueous silica concentration increases with depth and reaches ≈ 4.45 $10^{-5}$ mol L$^{-1}$ at 1 m depth regardless of weathering duration. Aqueous silica, $Al^{3+}$ and Fe concentrations in the soil solution are not impacted by ion exchange reactions. L-olivine application induces a decrease in the free $Al^{3+}$ concentration from 1.9 $10^{-8}$ mol L$^{-1}$ at the top of the profile to 1.0 $10^{-8}$ mol L$^{-1}$ at 1m depth, in accordance with gibbsite precipitation (Figure 10a). With a higher quantity of olivine (Figure 10b), $Al^{3+}$ increases in the soil top most 10 cm (3.23 $10^{-8}$ mol L$^{-1}$ after 1 yr) and the concentration stabilises at 2.3 $10^{-8}$ mol L$^{-1}$ along the rest of the profile for all weathering durations.

For the other cations, i.e. $Fe^{2+}$, $Fe^{3+}$, $Ca^{2+}$, $Mg^{2+}$, Na+ and $K^{+}$, their concentrations increase with depth and decrease with time for L- and H-olivine (Figure 10a and 10b). The cations concentrations increase linearly up to 80 cm depth before stabilising, except for the H-olivine where Fe and $Mg^{2+}$ show a steeper and greater increase in the amendment layer (0-20 cm depth) and are stable downwards in the soil profile.

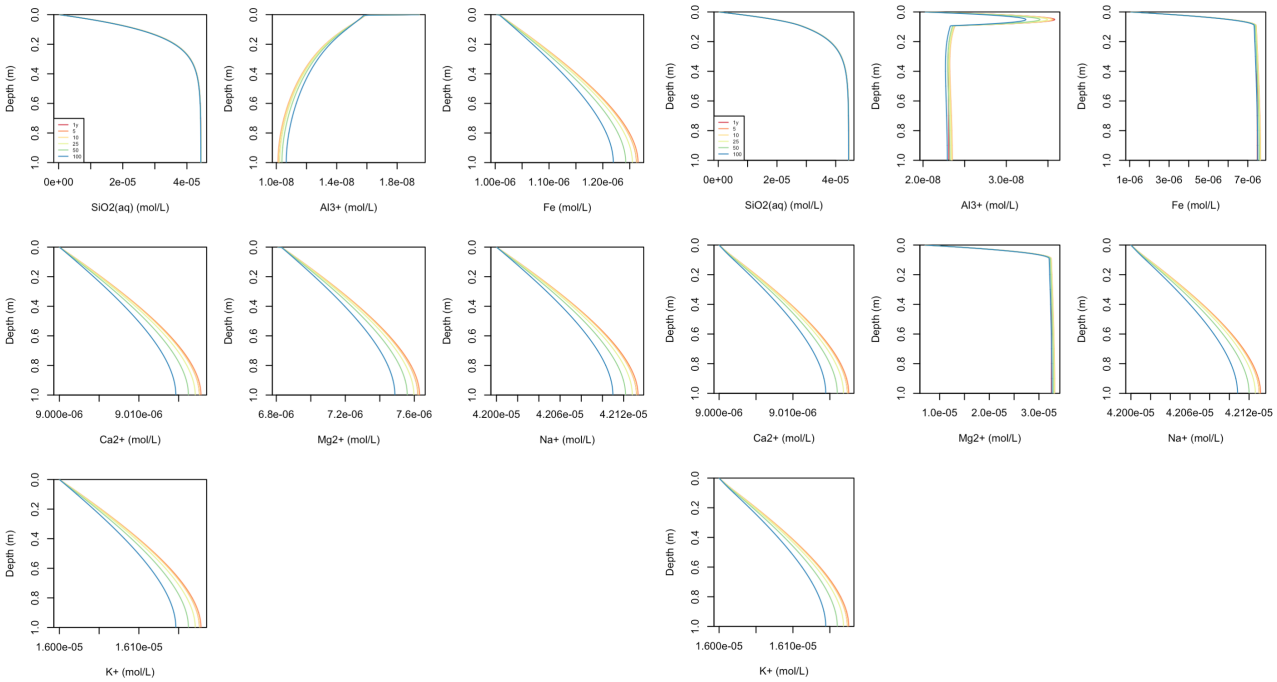


(a) M1 (L) (b) M1 (H)

Figure 10: Evolution with soil depth and weathering duration of the concentrations in solution of $SiO_{2(aq)}$, $Al^{3+}$, Fe, $Ca^{2+}$, $Mg^{2+}$, Na+ and $K^{+}$ after a single application of olivine of 5000 g $m^{-2}$ (10a) and 150000 g $m^{-2}$ (10b) to the soil surface without ion exchange reactions (M1).

### Ion exchange reactions and cation exchange capacity

As smectite does not precipitate after olivine application (Figure 9), ion exchange reactions can only occur on the exchange complex associated with kaolinite. These reactions modify the concentration distributions of $Ca^{2+}$, $Mg^{2+}$, Na+ and $K^{+}$ along the profile (Figure 11). For L- and H-olivine scenarios and all weathering durations, a higher concentration of $Ca^{2+}$, $Na^{+}$ and $K^{+}$ in the soil solution is predicted, in comparison with model M1, whereas $Mg^{2+}$ presents a lower concentration compared to simulations without ion exchange reactions.

When L-olivine is applied to the soil (Figure 11a), all dissolved cation concentrations peak around 20cm depth after 5 yr of weathering, and their concentrations along the entire weathering profile are the highest. Between 10 and 100 yr of weathering, a gradual decrease in the concentration of $Ca^{2+}$, Na+ and $K^{+}$ is then observed to reach a similar profile as for simulations without ion exchange (Figure 10a). The behaviour of $Mg^{2+}$ differs from that of the other alkaline and alkaline-earth cations: $Mg^{2+}$ decreases between 5 and 10 yr of weathering, indicating its fixation on the exchange complex, and then increases after 10 yr as olivine dissolution continues to release the cation.

With the addition of H-olivine to the soil (Figure 11b, the concentration of $Mg^{2+}$ increases with time and decreases with depth. The highest values ($\approx 3\ 10^{-5}$ mol $L^{-1}$) are found at $\approx$10 cm depth after 100 yr of weathering. Sodium concentration shows a decrease with time and it parallels the evolution observed for the simulations without ion exchange after 10 yr of weathering (Figure 10b and 11b). Calcium and $K^{+}$ concentrations evolve similarly with time and along the soil profile (Figure 11b). During the first years of weathering, their concentrations are higher at the top of the profile. As there is no other input of $Ca^{2+}$ and $K^{+}$ than rainfall, the

concentrations of these cations decrease with time and evolve with depth in a manner similar to that described when H-olivine is applied to the soil without ion exchange reactions (Figure 10b). Magnesium concentration increases with time and decreases with depth, showing a peak at 10 cm depth (Figure 11b).

Overall, kaolinite CEC remains stable around 2.7 $10^{-5}$ eqc $g^{-1}$ kaolinite. As kaolinite dissolves, especially at the top of the soil profile, soil CEC is expected to decrease.

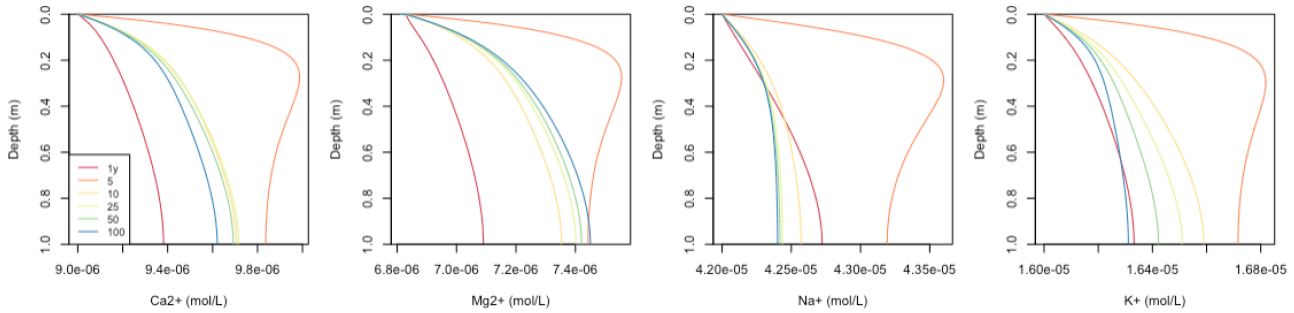


(a) $M1_{CEC}$ (L)

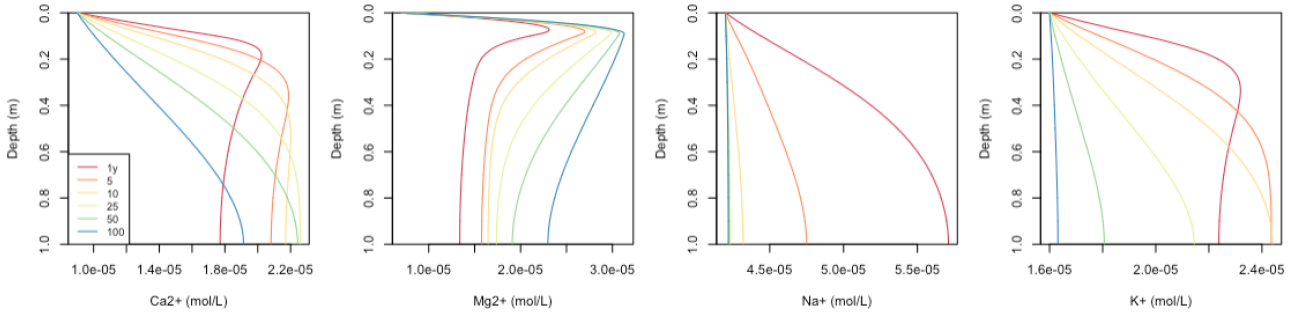


(b) $M1_{CEC}$ (H)

Figure 11: Evolution with depth and weathering duration of the concentrations in solution of $SiO_{2(aq)}$, $Al^{3+}$, Fe, $Ca^{2+}$, $Mg^{2+}$, Na+ and $K^{+}$ after a single application of olivine of 5000 g $m^{-2}$ (11a) and 150000 g $m^{-2}$ (11b) to the soil surface (M1) with ion exchange reactions (CEC).

## 4.2 M2/$M2_{CEC}$ - Oxisol with olivine incorporated into the 0-20 cm top soil layer

### Soil solution pH

The pH increase induced when the amendment is incorporated into the 0-20 cm layer of the topsoil is more important than when it is applied as an overlying layer for L- and H-olivine (Figure 8). For an applied quantity of 5000 g $m^{-2}$ (Figure 8c), below the topmost 20 cm, pH rises above 6.1 after 1 yr and continuous water flow leads to a decrease to values just below 6.1 after 100 yr. For H-olivine (Figure 8d), the pH increases up to ≈7.5 at the same depth and this value is sustained during 100 yr of weathering.

### Primary and secondary solid phases abundances

The weathering of olivine in the first 20 cm induces the precipitation of gibbsite (≈+0.4 V%. at the top of the profile) and the dissolution of kaolinite (≈-0.66 V%. at the top of the profile)

over the first 100 yr (Figure 12). Both phenomena occur over the 40 and 20 topmost cm of the profile for the L- and H-olivine application scenarios, respectively. The dissolution of kaolinite and precipitation of gibbsite are thus more important for the lower applied quantity. Similar to the results presented for models M1/M1$_{CEC}$, ≈+2 V%. of goethite precipitates at the top of the profile after 100 yr (Figure 12). No other secondary solid phases precipitate in the soil profile.

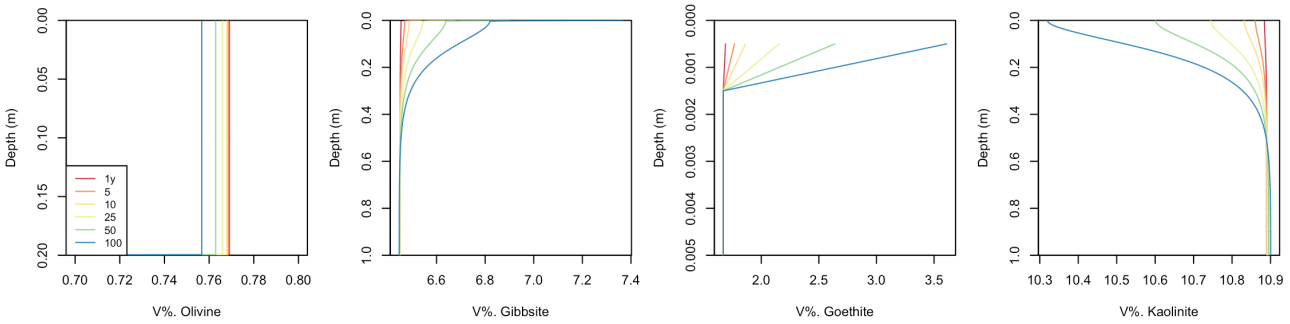


(a) M2/M2$_{CEC}$ (L)

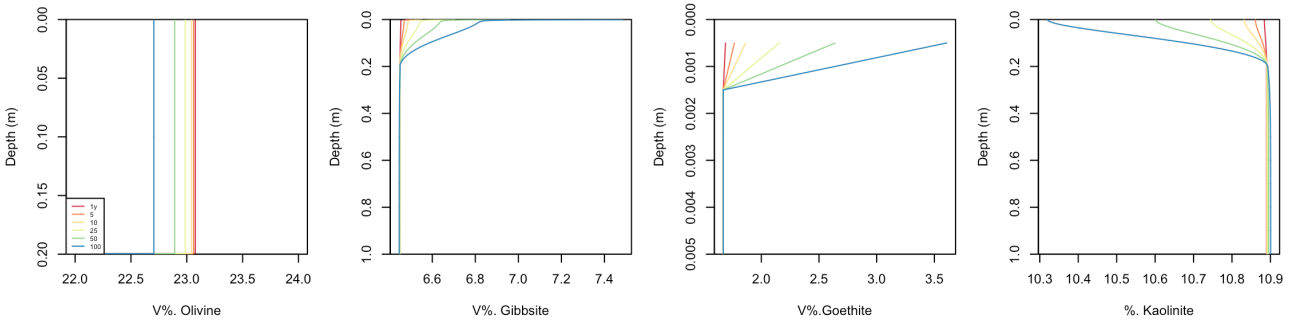


(b) M2/M2$_{CEC}$ (H)

Figure 12: Primary and secondary solid phases V%. evolution with soil depth and weathering duration after a single application of olivine of 5000 g m$^{-2}$ (12a) and 150000 g m$^{-2}$ (12b) incorporated into the 0-20 cm layer (M2). The model results with and without ion exchange (CEC) do not differ.

### Soil porosity

Following the application of L-olivine, porosity increases (≈+0.2%; Figure A.5) due to the dissolution of olivine and kaolinite, as observed for model M1 (Figure A.4). The dissolution of kaolinite being more important in the 20 first cm, the porosity increase is also greater in this layer. H-olivine increases the porosity by ≈0.5%, which is slightly superior to that of L-olivine.

### Aqueous species concentrations

Similar to the results presented in section 4.1, the concentrations of all aqueous species are predicted to increase compared with their initial concentrations in the rainfall, except for $Al^{3+}$ with L- olivine (Figure 13). For all simulations, $SiO_{2(aq)}$ concentration increases with depth and the concentration profiles resemble those described for model M1 (Figures 10 and 13). Iron concentration also shows a similar behaviour to that when olivine is applied to the soil surface. In contrast, the concentration of $Al^{3+}$ shows a different behaviour from that obtained in the previous model (Figures 13a and 13b). It decreases linearly before stabilising below 20 cm depth for L-olivine (Figure 13a) and increases linearly before stabilising below 20 cm depth for H-olivine (Figure 13b). The simulations predict a linear increase in $Ca^{2+}$, $Mg^{2+}$, Na+

and $K^+$ along the entire profile, except for $Mg^{2+}$ in the H-olivine scenario. In this case, $Mg^{2+}$ concentration increases up to 20 cm depth and is stable along the rest of the profile. All these species show a decrease in concentration with time along the soil column (Figures 13a and 13b).

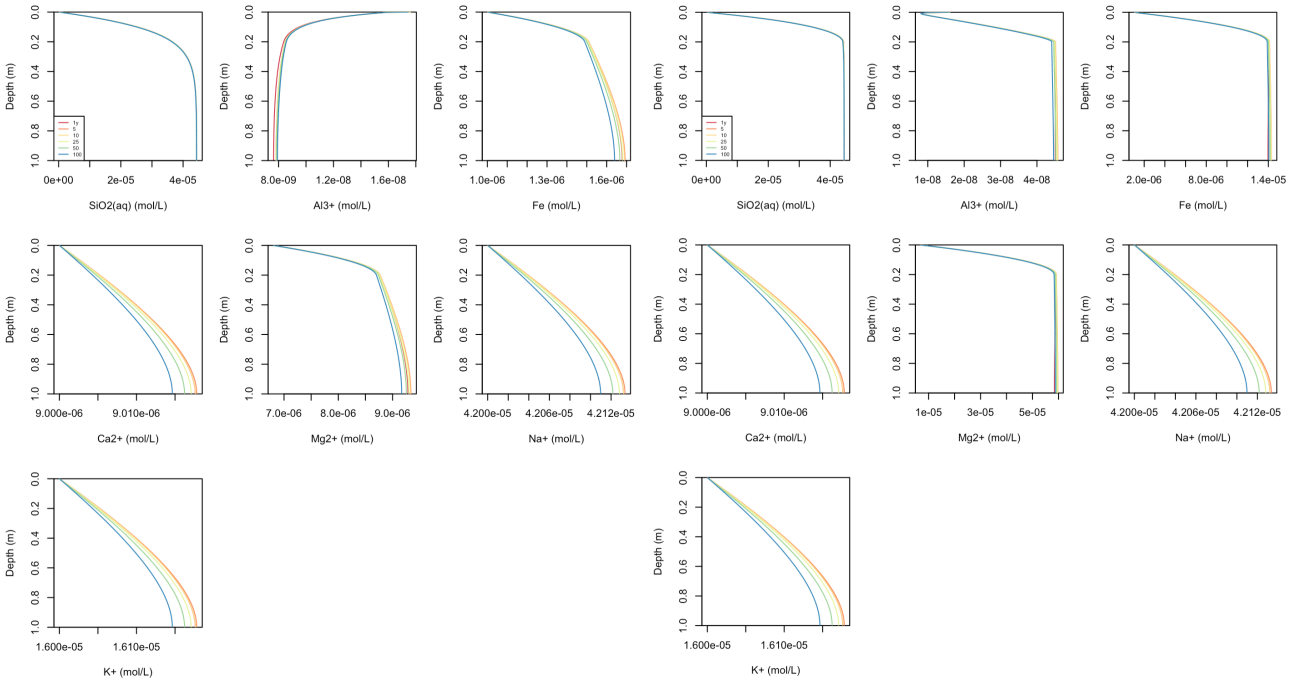


(a) M2 (L) (b) M2 (H)

Figure 13: Evolution with soil depth and weathering duration of the concentration in solution of $SiO_{2(aq)}$, $Al^{3+}$, Fe, $Ca^{2+}$, $Mg^{2+}$, Na+ and $K^+$ after a single application of olivine of 5000 g $m^{-2}$ (13a) and 150000 g $m^{-2}$ (13b) into the 0-20 cm top soil layer without ion exchange reactions (M2).

### Ion exchange reactions and Cation Exchange Capacity

When ion exchange reactions on kaolinite are included, the temporal and spatial concentration evolution of $Na^+$, $K^+$, $Ca^{2+}$ and $Mg^{2+}$ vary. For both application rates, the predicted results are similar to those found for surface application of olivine (Figures 11b and 14). Similarly, for all weathering periods and application scenarios, $Na^+$, $K^+$ and $Ca^{2+}$ concentrations are higher and $Mg^{2+}$ lower than without ion exchange reactions (Figures 13 and 14). Sodium concentration (Figure 14) increases during the first year of weathering and then decreases to reach the same evolution profile as for model M2 (Figure 13).

Magnesium concentration shows a concentration peak around 20 cm depth for both L- and H-olivine (Figure 14a and 14b). It decreases with depth and increases with time. The concentration stabilises at values around $\approx$8.0 $10^{-6}$ mol $L^{-1}$ (L-scenario) and $\approx$4.5 $10^{-5}$ mol $L^{-1}$ (H-scenario) at 1 m depth. With time, $K^+$ and $Ca^{2+}$ concentrations show similar patterns (Figure 14). They first increase during 5 yr (L-scenario) or 1 yr (H-scenario) of olivine weathering. Potassium and $Ca^{2+}$ then decrease progressively until 100 yr of weathering. For both ions, the concentrations peak at 20 cm depth, which also corresponds to the depth at which more $Mg^{2+}$ is released into solution.

On average, CEC remains stable around 1.8 $10^{-5}$ eqc $g^{-1}$ mineral, for L-olivine and decreases from 1.7 $10^{-5}$ to 9.0 $10^{-6}$ eqc $g^{-1}$ mineral, for H-olivine in 100 yr of weathering. As kaolinite

is expected to dissolve, soil CEC is predicted to decrease.

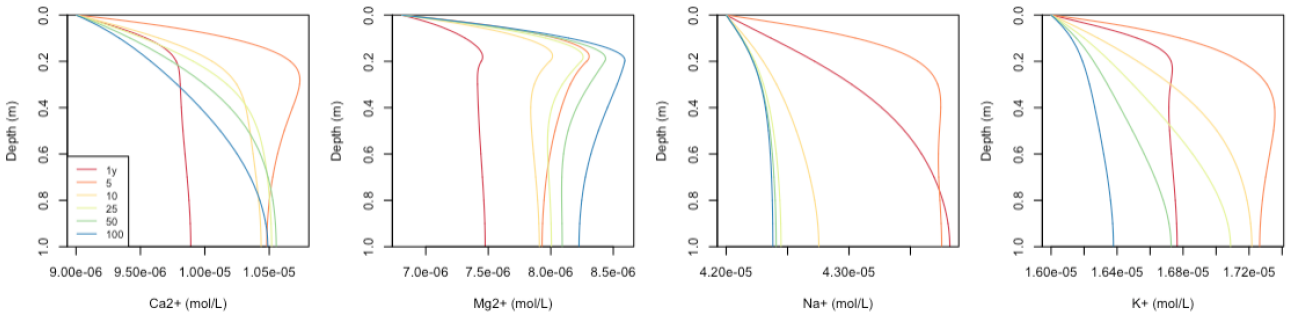


(a) $M2_{CEC}$ (L)

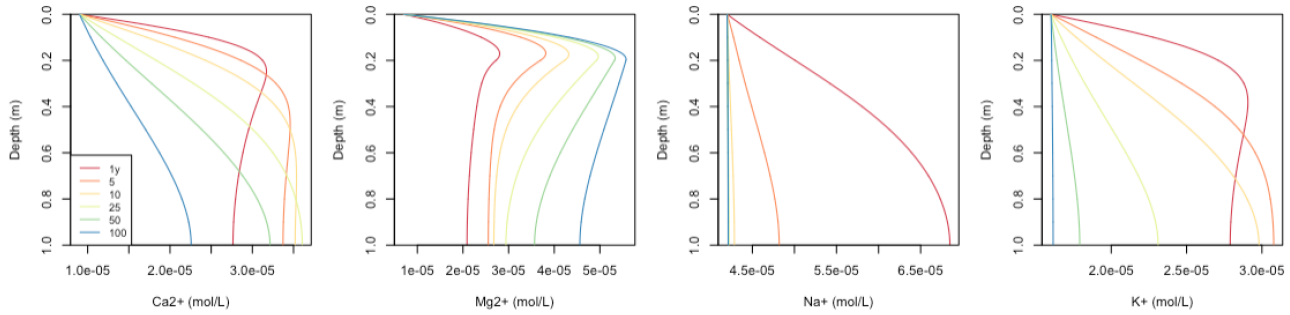


(b) $M2_{CEC}$ (H)

Figure 14: Evolution with depth and weathering duration of the concentration in solution of $SiO_{2(aq)}$, $Al^{3+}$, Fe, $Ca^{2+}$, $Mg^{2+}$, Na+ and $K^{+}$ after a single application of olivine of 5000 g $m^{-2}$ (14a) and 150000 g $m^{-2}$ (14b) into the 0-20 cm top soil layer (M2) with ion exchange reactions (CEC)

## 4.3 $M3/M3_{CEC}$ - Oxisol with an overlying basalt layer

### Soil solution pH

For an identical applied quantity of basalt to the soil surface, soil solution pH increase is greater compared to an amendment with olivine (Figure 15a, 15b, 8a and 8a), regardless of the application mode. This trend is more pronounced for the highest silicate load (150000 g $m^{-2}$). Application of 5000 g $m^{-2}$ of basalt (Figure 15a) leads to a pH increase up to ≈5.9 (≈5.83 for olivine) after 1 yr at the bottom of the soil profile, before decreasing to 5.8 after 100 yr. When 150000 g $m^{-2}$ of basalt is applied (Figure 15b), pH stabilises below 0.1 m depth at a value of ≈9.7 after 1 yr of weathering (≈7.1 for olivine). pH then decreases with time and continuous water flow to reach ≈7.6 after 100 yr.

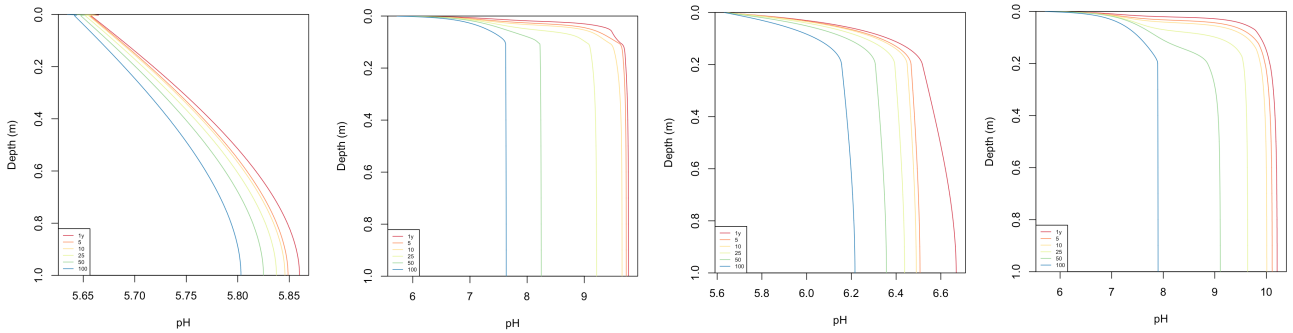


(a) M3/M3$_{CEC}$ (L) (b) M3/M3$_{CEC}$ (H) (c) M4/M4$_{CEC}$ () (d) M4/M4$_{CEC}$ (H)

Figure 15: Soil solution pH evolution as a function of soil depth and weathering duration after a single application of basalt to the soil surface (M3) of 50000 g m$^{-2}$ (15a) and 150000 g m$^{-2}$ (15b); and into the 0-20 cm top soil layer (M4) of 50000 g m$^{-2}$ (15c) and 150000 g m$^{-2}$ (15d). The model results with and without ion exchange (CEC) do not differ.

### Primary and secondary solid phases abundances

When basalt is applied to the soil surface, the solid phase that dissolves the most is plagioclase (Figure 16). Other constituting minerals also dissolve, i.e. olivine, K-feldspar and diopside, whereas quartz and basaltic glass remain inert. In total, in 1 yr, less than 0.5 V%. of the basaltic rock dissolves. K-feldspars are the only primary minerals that present a distinct weathering front which moves downward with time for H-basalt. In the top most 3 mm, similarly to the results obtained for olivine amendment, goethite precipitates (≈+2 V%.) for L- and H-basalt scenarios (Figure 16). Below the amendment layer, gibbsite precipitation (≈+1.5 V% between 2 and 6 mm depth) and kaolinite dissolution (≈-0.66 V%. in the top most 0-40 cm) are predicted after the application of L-basalt (Figure 16a). No other secondary solid phases precipitate after 100 yr of weathering.

The addition of 150000 g m$^{-2}$ produces contrasting results (Figure 16b). Both gibbsite and kaolinite show an accumulation peak (≈11 and 32 V%., respectively) at the interface between the amendment layer and the Oxisol, followed by the dissolution of gibbsite and the precipitation of kaolinite with time in the next 30 cm (Figure 16b). Moreover, there is a large precipitation of allophanes in the amendment layer (0-10cm, ≈+8 V%.). At the interface between the basaltic rock overlying layer and the soil, a slight accumulation of calcite is predicted during the first 5 yr of weathering and the precipitation (≈+4 V%.) of smectite is expected during the first 100 yr of weathering (Figure 16b). Other secondary solid phases do not form.

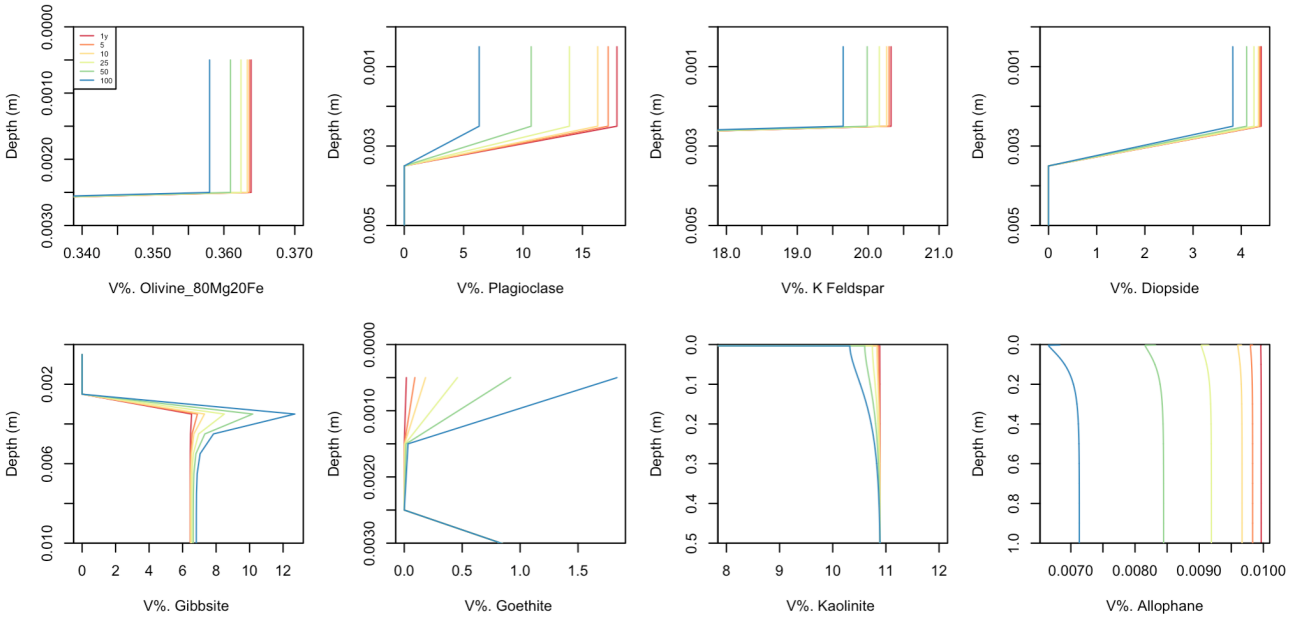


(a) M3/M3$_{CEC}$ (L)

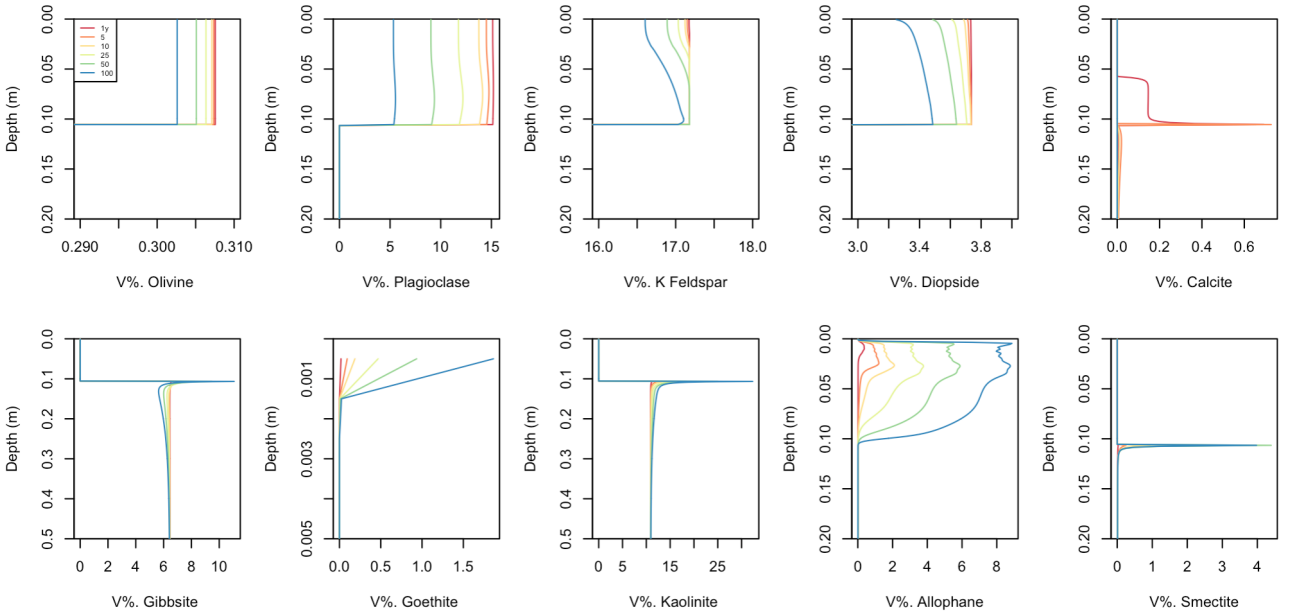


(b) M3/M3$_{CEC}$ (H)

Figure 16: Primary and secondary solid phases V%. evolution with soil depth and weathering duration after a single application of basalt of 5000 g m$^{-2}$ (16a) and 150000 g m$^{-2}$ (16b) to the soil surface (M3). The model results with and without ion exchange (CEC) do not differ.

### Soil porosity

For all simulations, soil porosity as a function of time and depth shows a similar evolution. The dissolution of plagioclase, K-feldspar, diopside and olivine (constituting minerals of the basaltic rock) results in an increase in porosity in the amendment layer (≈4 and 10 % for L- and H-basalt, respectively). In addition, for H-basalt (Figure A.6), a strong decrease in porosity (≈ 32%) is predicted at the interface between the amendment layer and the soil profile, probably reflecting precipitation of kaolinite, allophanes and smectite at this depth (Figure 12b), which does not occur for L-basalt. The porosity increase in the amendment layer is thus greater than

for olivine amendment, but the consequent decrease in porosity at the interface when H-basalt is applied is not observed with H-olivine addition.

### Aqueous species concentrations

For the L-basalt scenario (Figure 16a), $SiO_{2(aq)}$ concentration increases with depth and is constant during the 100 yr of weathering. Alumininum, which comes from the dissolution of plagioclases, K-feldspars, diopside and kaolinite, increases in solution after 1 yr of weathering, up to $\approx$1.2 $10^{-7}$ mol $L^{-1}$ in the top 3 mm. Aluminium concentration then decreases with time at this depth and remains stable downwards. Iron and $Mg^{2+}$ both come from olivine dissolution. Their concentrations increase with depth and slightly decrease with time, since olivine dissolution slows down. The same concentrations evolution are predicted for $Na^{+}$ (from plagioclase), $Ca^{2+}$ (from plagioclase and diopside) and $K^{+}$ (from K-feldspar).

When the applied basalt quantity increases, $SiO_{2(aq)}$ and $Al^{3+}$ exhibit the same evolution with depth and time. A concentration peak of both species is predicted in the amendment layer after 1 yr of weathering before decreasing and stabilising with depth. Iron and $Mg^{2+}$ concentrations remain close to zero during the 25 first years of weathering before increasing to $\approx$1.2 $10^{-6}$ and 1.3 $10^{-5}$ mol $L^{-1}$, respectively, after 100 yr of weathering. Calcium concentration decreases, whereas $Na^{+}$ concentration increases in the soil solution during the first 10 yr and then decreases with time. Finally, $K^{+}$ concentration increases with time along the entire soil profile.

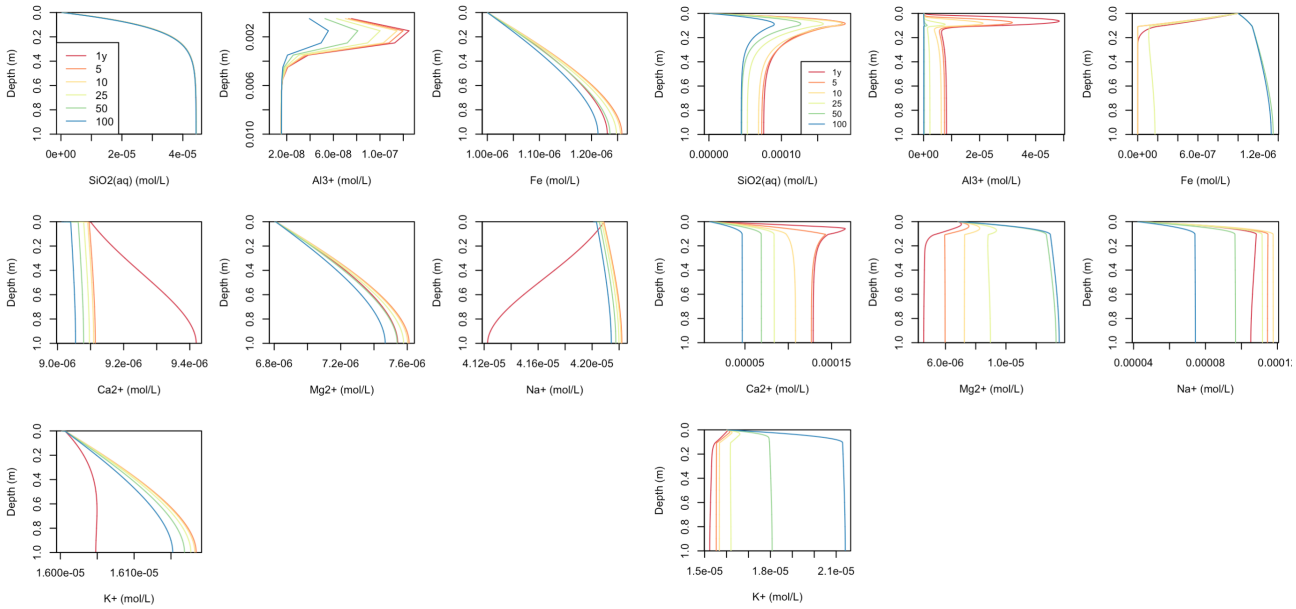


(a) M3 (L) (b) M3 (H)

Figure 17: Evolution with soil depth and weathering duration of the concentration in solution of $SiO_{2(aq)}$, $Al^{3+}$, Fe, $Ca^{2+}$, $Mg^{2+}$, Na+ and $K^{+}$ after a single application of basalt of 5000 g $m^{-2}$ (17a) and 150000 g $m^{-2}$ (17b) to the soil surface without ion exchange reactions (M3).

### Ion exchange reaction and Cation Exchange Capacity

The simulations for L-basalt weathering (Figure 18a) predicts similar concentration evolution for $Ca^{2+}$, $Mg^{2+}$, $Na^{+}$ and $K^{+}$ with ion exchange reactions to that obtained for L-olivine (Figure 11a). Kaolinite CEC is expected to remain stable (-8.3 $10^{-7}$ eqc $g^{-1}$ kaolinite) in the 0-20 cm

layer and, as kaolinite dissolves in the topmost 40 cm, soil CEC is expected to decrease in this layer. The addition of H-basalt shows very different results (Figure 18b). Calcium is released in larger quantity through the basaltic rock dissolution, thereby replacing $Mg^{2+}$, $Na^{+}$ and $K^{+}$ on the exchange complex. Magnesium and $K^{+}$ concentration in the soil solution decrease during the 100 yr of weathering. Calcium concentration peaks in the amendment layer during the first year of weathering and the concentration then progressively decreases with time along the entire soil profile. Sodium concentration increases during the first 10 yr of weathering and decreases until 100 yr of weathering.

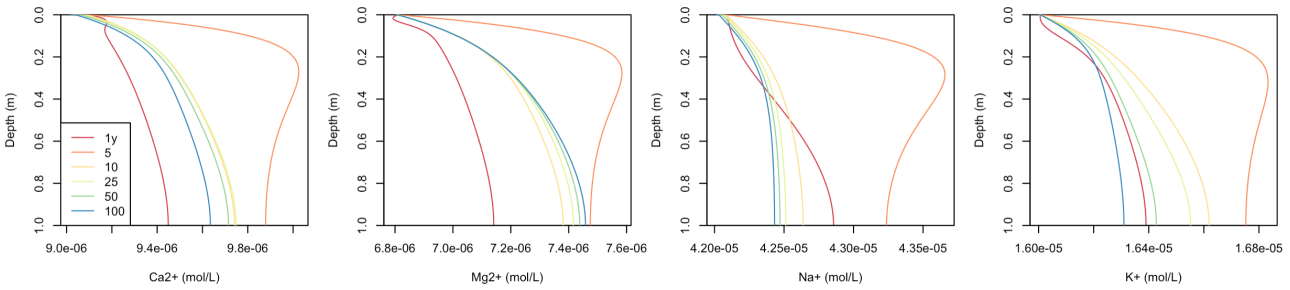


(a) M3$_{CEC}$ (L)

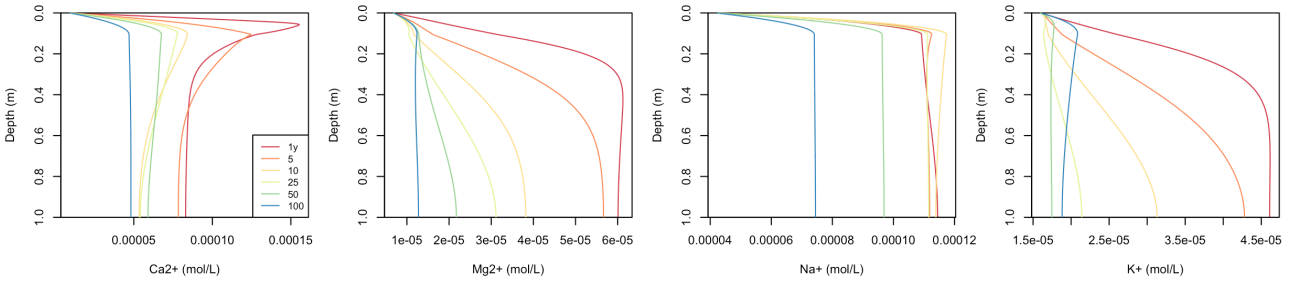


(b) M3$_{CEC}$ (H)

Figure 18: Evolution with depth and weathering duration of the concentration in solution of $SiO_{2(aq)}$, $Al^{3+}$, Fe, $Ca^{2+}$, $Mg^{2+}$, Na+ and $K^{+}$ after a single application of basalt of 5000 g m$^{-2}$ (18a) and 150000 g m$^{-2}$ (18b) to the soil surface (M3) with ion exchange reactions (CEC).

In the H-basalt scenario, smectite and kaolinite CEC increases with time (Figure 19), as opposed to results obtained for L- and H-olivine as well as L-basalt. The sum of their CEC increases from 2.5 $10^{-5}$ to 1.6 $10^{-4}$ eq g$^{-1}$ smectite and kaolinite at 11 cm depth after 100 yr of weathering and, as they precipitate at the same depth, soil CEC should increase even more in this layer.

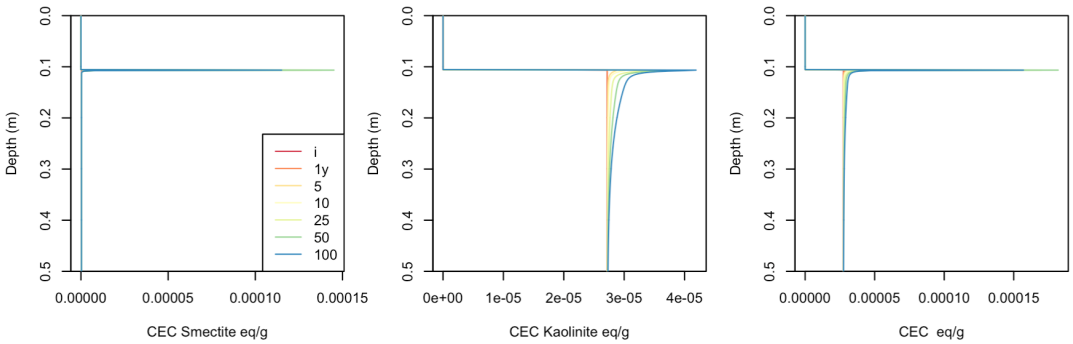


Figure 19: Cation exchange capacity of smectite (a), kaolinite (b), and their sum (c) as a function of depth and weathering duration after a single application of 150000 g m$^{-2}$ of basalt to the soil surface (M3) with ion exchange reactions (CEC).

## 4.4 M4/M4$_{CEC}$ - Oxisol with basalt incorporated into the 0-20 cm top soil layer

### Soil solution pH

The weathering of basal incorporated into the 0-20 cm depth layer induces a more important pH rise than when it is added to the soil surface (Figure 15). In the L-scenario (Figure 15c), pH stabilises below 20 cm at ≈6.7 after 1 yr (≈5.9 for L-basalt) and decreases to 6.2 after 100 yr of weathering. Similarly, in the H-scenario (Figure 15d), pH stabilisation occurs below 20 cm depth but at a value much higher than that obtained with lower basalt application rate, i.e. pH of 10.2 after 1 yr. The pH decreases with time to reach 7.9 after 100 yr.

### Primary and secondary solid phases abundances

The incorporation of basalt (L- and H-scenarios) into the soil leads to gradual dissolution of the primary minerals plagioclases, olivine, K-feldspar and diopside, similar to the results obtained when the silicate is applied to the soil surface (Figure 20). In H-basalt (Figure 20b), K-feldspar and diopside show a weathering front that moves downward with time. In both cases, goethite precipitates (≈+2 V%.) in the top 2 mm of the soil.

The effect of basalt addition on the dissolution of primary minerals and precipitation of secondary solid phases differs between the L- and H-scenarios. In the former (Figure 20a), only gibbsite precipitates, whereas kaolinite dissolves (≈-0.66 V%. in 100 yr at the top of the profile). The depth at which kaolinite dissolution occurs (0-40 cm) corresponds to the depth at which gibbsite starts to precipitate (≈7 V%. after 100 yr). At a higher basalt application rate (Figure 20b), calcite is predicted to precipitate at 20 cm depth during the first 25 yr of weathering. Between 0 and 60 cm, kaolinite abundance increases with time to reach ≈14.9 V%. after 100 yr and is steady in time in the rest of the soil profile. With time, gibbsite precipitates in the first 10 cm (≈9.5 V%.) and dissolves between 10 and 60 cm (≈5.7 V%.), i.e. the same depth at which kaolinite precipitates. Regarding the secondary solid phases, only smectites precipitate in the top most 20 cm.

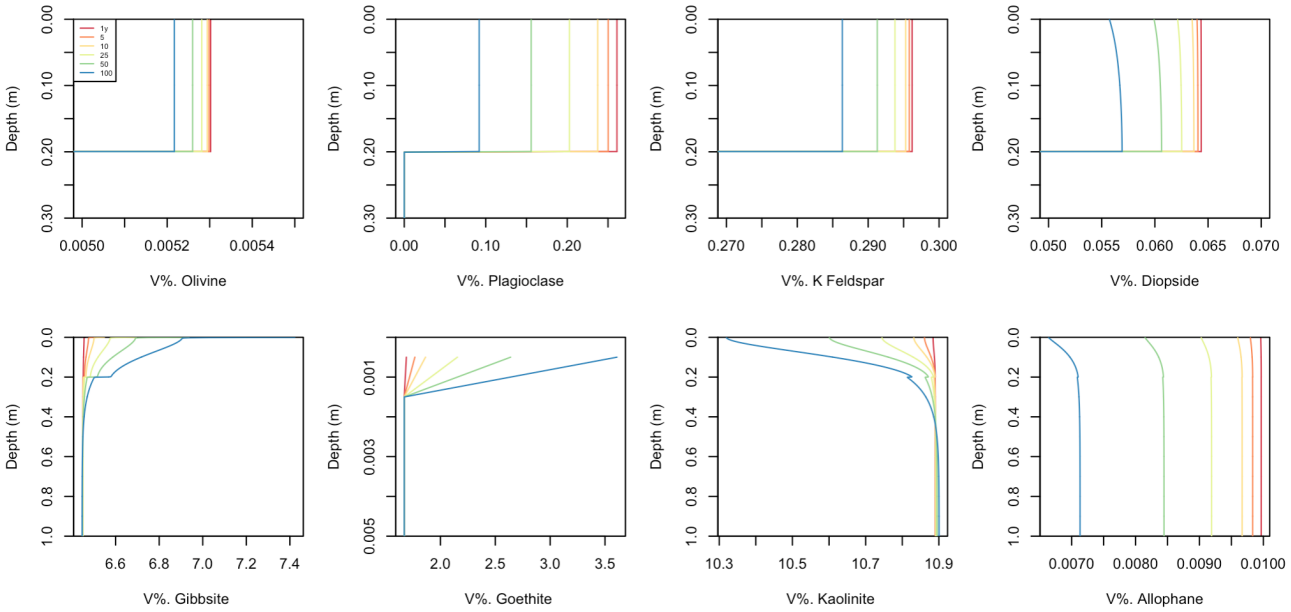


(a) M4/M4$_{CEC}$ (L)

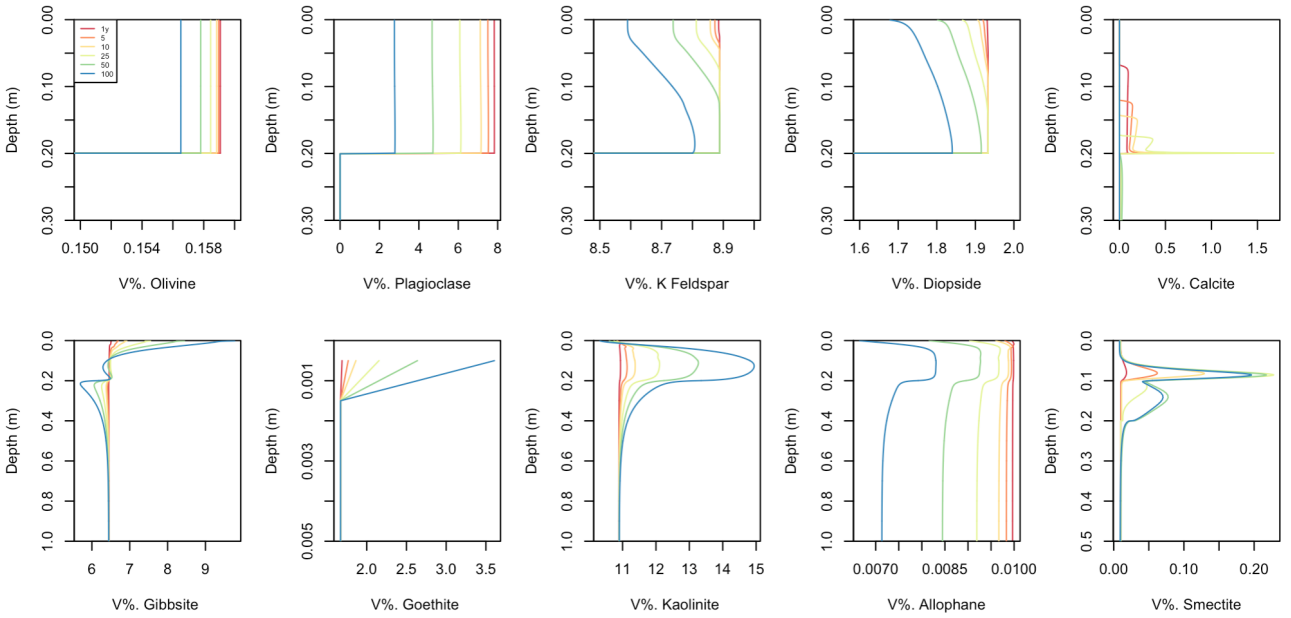


(b) M4/M4$_{CEC}$ (H)

Figure 20: Primary and secondary solid phases V%. evolution with soil depth and weathering duration after a single application of basalt of 5000 g m$^{-3}$ (20a) and 150000 g m$^{-2}$ (20b) incorporated into the 0-20 cm layer (M4). The model results with and without ion exchange (CEC) do not differ.

### Soil porosity

Simulations for both basalt application rates produce similar soil porosity along the soil weathering profile (Figure A.7). In the 0-20 cm topsoil layer, an increase in porosity is predicted by the models (≈0.3 and 3% in the L- and H-scenario, respectively), due to the dissolution of the basaltic rock components. Below the mixed layer, for the higher application rate, a slight decrease in porosity occurs due to kaolinite and smectite precipitation, whereas a small increase is predicted for the lower application rate because of kaolinite dissolution (Figure A.7). The predicted porosity increase is slightly higher compared to the results obtained with olivine addition.

### Aqueous species concentrations

When 5000 g $m^{-2}$ of basalt is incorporated (Figure 21a), in the topmost 40 cm, $SiO_{2(aq)}$ concentration decreases with time and increases with depth. The concentration in $SiO_{2(aq)}$ in the weathering profile remains low at all time. In the 10 first cm, free $Al^{3+}$ concentration decreases with depth and increases with time (Figure 21a). It stabilises below this depth and only decreases with time. Iron and $Mg^{2+}$ are released through olivine dissolution, thereby, their concentrations increase with depth and decrease with time (Figure 21a). As for the addition of basalt to the soil surface (Figure 17a), $Ca^{2+}$ concentration decreases strongly between 1 and 5 yr of weathering along the entire soil profile. Then, for all weathering durations, the concentration increases until 20 cm depth and decreases with time. Sodium and $K^{+}$ show similar concentration evolution. Their concentrations stabilise below 20 cm depth and decrease during the 100 yr of weathering.

With an increased quantity of basalt applied (Figure 21b), $SiO_{2(aq)}$ concentration peaks around 20 cm depth and decreases with time and depth. Aluminium concentration shows a slight peak at 20 cm depth, increases with depth and decreases with time to reach a concentration of 0 mol $L^{-1}$ after 100 yr of weathering. Iron, $K^{+}$ and $Mg^{2+}$ concentrations increase with time and are stable below 20 cm depth, regardless of weathering duration. Inversely, $Na^{+}$ concentration decreases with time and increases up to 20 cm depth. The Ca2+ concentration stabilises in the soil profile below 20 cm depth. During the 100 yr of weathering, the concentration decreases with time in the topmost 20 cm. Below 20 cm depth, the concentration decreases between 1 and 25 yr of weathering, increases from 25 to 50 yr of weathering and decreases again until 100 yr of weathering.

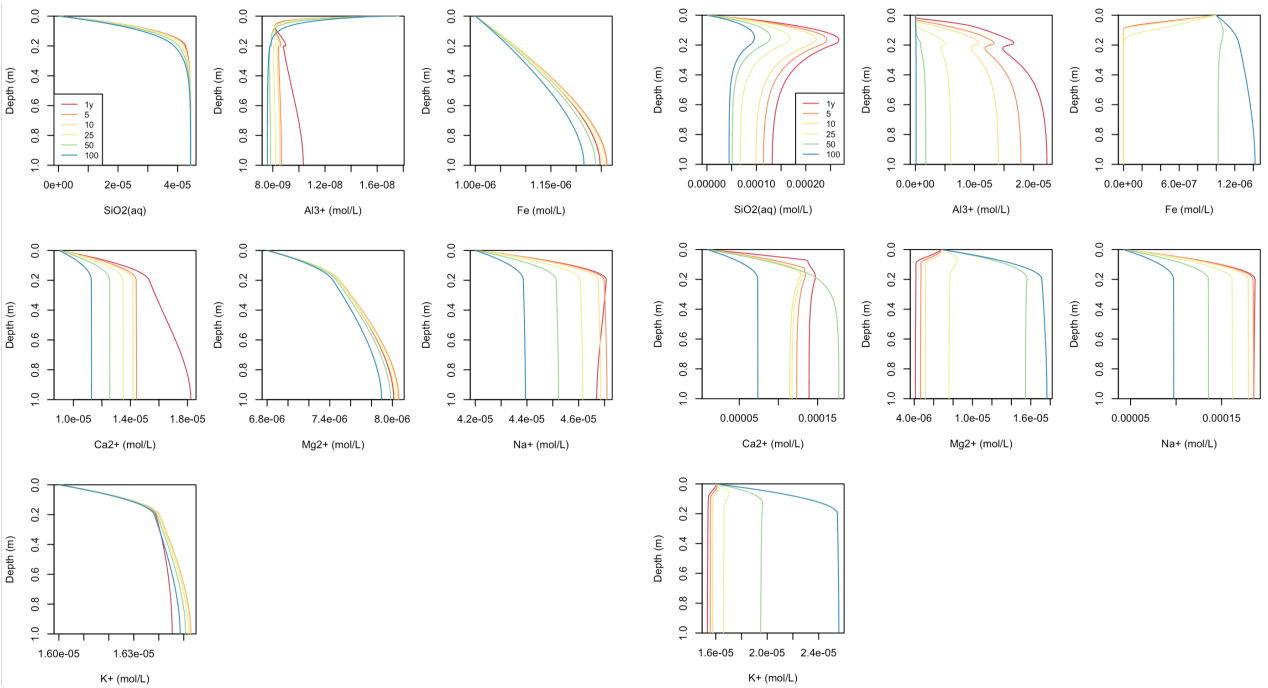


(a) M4 (L) (b) M4 (H)

Figure 21: Evolution with depth and weathering duration of the concentration in solution of $SiO_{2(aq)}$, $Al^{3+}$, Fe, $Ca^{2+}$, $Mg^{2+}$, Na+ and $K^{+}$ after a single application of basalt of 5000 g $m^{-2}$ (21a) and 150000 g $m^{-2}$ (21b) into the 0-20 cm soil layer (M4) without ion exchange reactions.

### Ion exchange reaction and Cation Exchange Capacity

For L- and H-basalt scenarios, with ion exchange reactions, $Ca^{2+}$ replaces $Mg^{2+}$, $K^{+}$ and $Na^{+}$ on the exchange complex. This explains why overall, $Mg^{2+}$, $K^{+}$ and $Na^{+}$ concentration are higher and $Ca^{2+}$ concentration lower with (Figure 22) than without (Figure 21) ion exchange reactions. The concentrations of all ions show a stabilisation below 20 cm depth for all weathering periods following L- and H-basalt application.

Regarding the application of L-basalt, the concentrations of all cations decrease with time along the entire soil profile (Figure 22a). Since no smectite precipitate, we only consider the CEC of kaolinite, which slightly decreases in the first 40 cm of the profile. Kaolinite is also expected to dissolve in the 0-40 cm top soil layer, hence soil's CEC will likely decrease with weathering duration. For the H-basalt scenario (Figure 22b), during the first 50 yr of weathering, the concentration of $Ca^{2+}$ increases and decreases between 50 and 100 yr of weathering. Similar to the L-basalt scenario, $Mg^{2+}$ and $Na^{+}$ concentrations decrease during 100 yr of weathering. Potassium concentration decreases during the first 50 yr and increases from 50 to 100 yr along the entire soil profile.

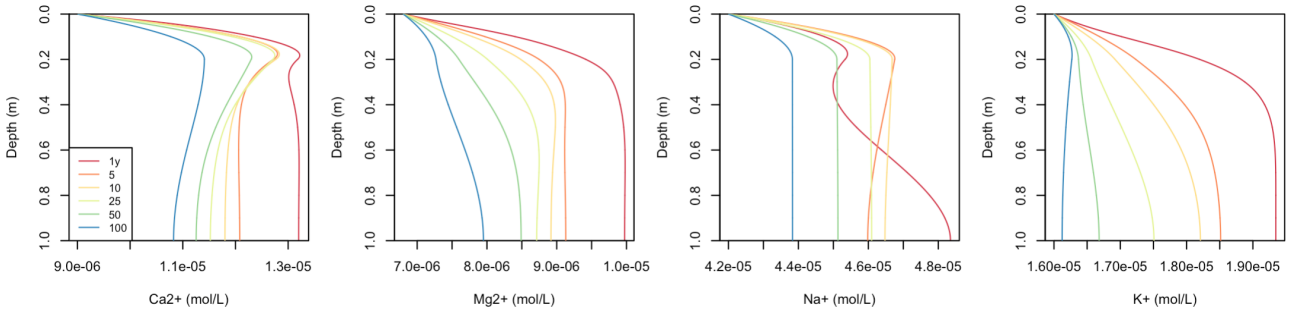


(a) M4$_{CEC}$ (L)

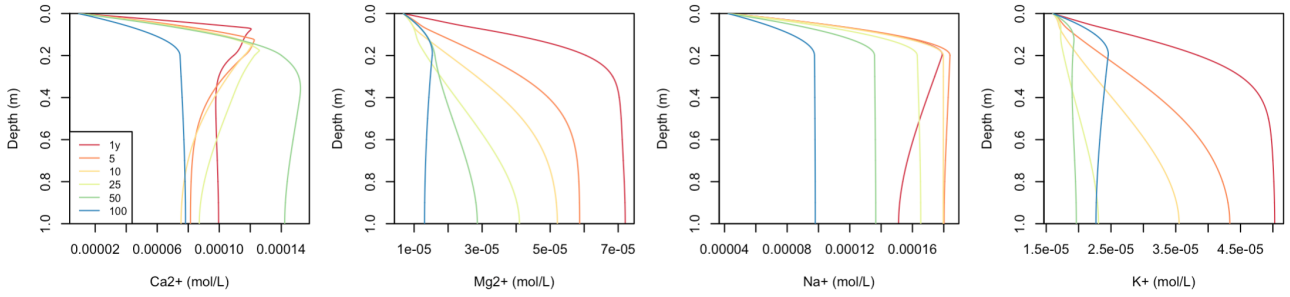


(b) M4$_{CEC}$ (H)

Figure 22: Evolution with depth and weathering duration of the concentration in solution of $SiO_{2(aq)}$, $Al^{3+}$, Fe, $Ca^{2+}$, $Mg^{2+}$, Na+ and $K^{+}$ after a single application of basalt of 5000 g m$^{-2}$ (22a) and 150000 g m$^{-2}$ (22b) in the top most 20 cm (M4) with ion exchange reactions (CEC).

When 150000 g m$^{2}$ of basalt is incorporated into the soil top most 20 cm, the CEC is calculated for kaolinite and smectite, since the latter is expected to precipitate. In 100 yr, their CEC increases in the 20 first cm from 2.3 $10^{-5}$ to 2.6 $10^{-5}$ eq g$^{-1}$ mineral (Figure 23). The increase is smaller than for the application of basalt to the soil surface (Figure 19), but occurs over a greater depth.

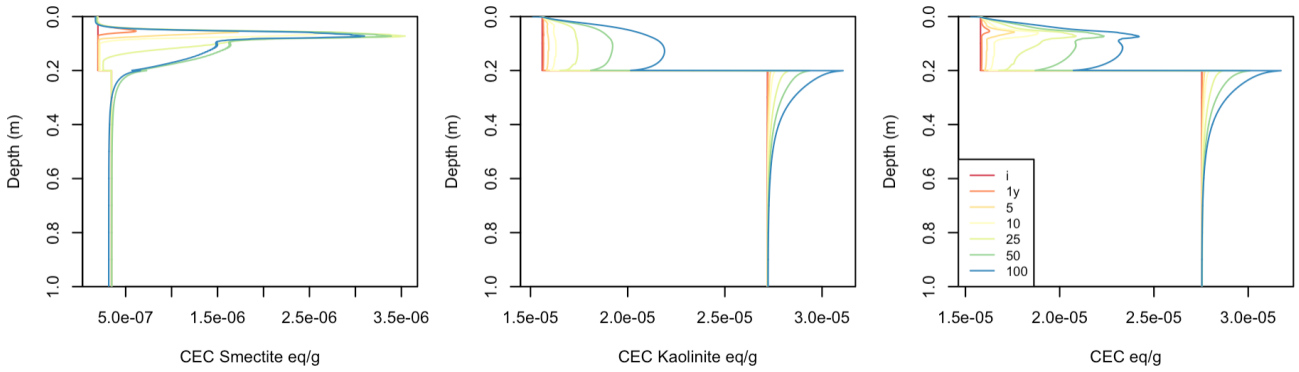


Figure 23: Cation exchange capacity of smectite (a), kaolinite (b) and their sum (c) as a function of depth and weathering duration after a single application of 150000 g $m^{-2}$ (ii) of basalt into the O-20 cm soil layer (M4) with ion exchange reactions (CEC).

## 4.5 Sensitivity analysis to allophanes solubility constant

To assess the influence of the solubility constant of allophanes on their precipitation upon weathering of basalt or olivine, we lowered their solubility using a solubility constant (log K= 7.02) reported for allophanes with a Si:Al ratio of 2 (Lumdson and Farmer, 1995). In doing so, allophanes were predicted to form along the entire soil profile in all models. This contrasts with our previous results, where only the application of H-basalt led to allophanes precipitation during weathering.

All models show that allophanes start precipitating at a certain depth, depending on the amendment, the applied quantity and the application mode. Allophanes V%. increases with time. The magnitude of their precipitation is most important where the amendment is applied and stable in the rest of the soil profile (Figure A.8). At the same depth at which allophanes start to precipitate, gibbsite dissolution occurs, and above this depth, gibbsite usually forms (Figure A.8). Due to allophanes precipitation, the concentration profiles of $SiO_{2(aq)}$ and $Al^{3+}$ are modified with depth and weathering duration compared to the initial results. For olivine and basalt amendments, $SiO_{2(aq)}$ concentration (Figure A.9) still increases with depth but decreases with time, in contrast to the previous models that considered a higher allophanes solubility (e.g. Figure 10a). When the applied quantity of basalt or olivine is higher, high concentrations of $Al^{3+}$ no longer build up at the top of the profile. The simulations show a decrease in $Al^{3+}$ (Figure A.9) at the same depth at which $Al^{3+}$ concentration peaked with the initial allophanes solubility constant (e.g. Figure 10b)

## 4.6 Carbon dioxide removal potential

For all simulations, the results with and without ion exchange (CEC) do not differ. Carbon dioxide removal potential upon basalt weathering is greater than that inferred for olivine, regardless of the application rate (126-758 and 125-266 g CO2 $m^{-2}$ $yr^{-1}$ for L-basalt and L-olivine, respectively, and 4231-1183 and 2172-4220 g CO2 $m^{-2}$ $yr^{-1}$ for H-basalt and H-olivine, respectively; Figure 25 and Table A.2). In L-olivine and L-basalt simulation, a decrease in annual CDR with weathering duration is observed (Figure 24). This decrease is more important following basalt application in the 0-20 cm layer (-62.2 % in 100 yr; Figure 24b) than for olivine amendment using the same application mode (-9.23% in 100 yr; Figure 24a). The same temporal evolution is observed when the silicates are applied on the soil surface with a decrease of -5.5% and -13.17%

in 100 yr for olivine and basalt, respectively. The results show that annual CDR decreases more rapidly when the amendment is incorporated into the soil than when it is spread on the surface.

H-olivine produces a rather stable annual CDR with weathering duration (Figure 24a). It slightly increases between 1 and 5 yr of weathering (+1.2% and +1% for M1 and M2, respectively) and decreases afterwards until 100 yr of weathering (-1.9% and -1.7% for M1 and M2). However, H-basalt leads to more unstable annual CDR evolutions with weathering duration for both application modes (Figure 24b). When basalt is added to the soil surface, annual CDR increases between 1 and 5 yr of weathering (+1.9%), decreases from 5 yr to 10 yr (-20.8%), rises again until 50 yr of weathering (+20%) and finally decreases until 100 yr of weathering (-31.7%). In contrast, when basalt is incorporated into the 0-20 cm layer, annual CDR strongly increases until 50 yr of weathering (+69%) and greatly diminshes until 100 yr of weathering (-41.5%).

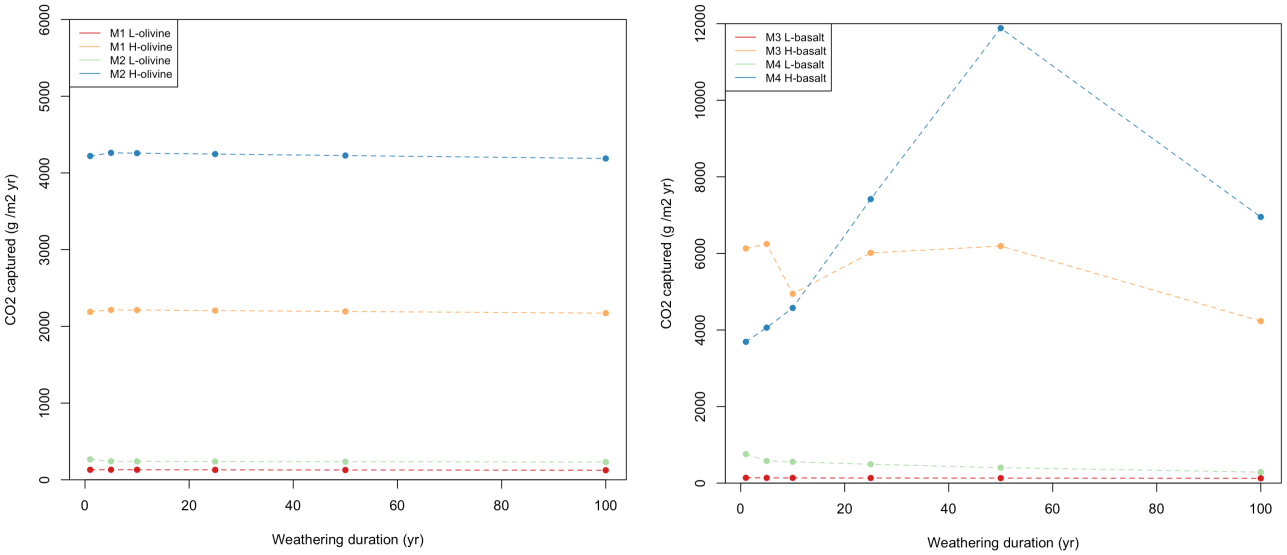


(a) Olivine

(b) Basalt

Figure 24: Evolution of annual CDR with weathering duration after a single application of olivine (24a) and basalt (24b) for both applications rates (L- and H-) and both application modes (on the soil surface and incorporated into the 0-20 cm layer). The model results with and without ion exchange (CEC) do not differ.

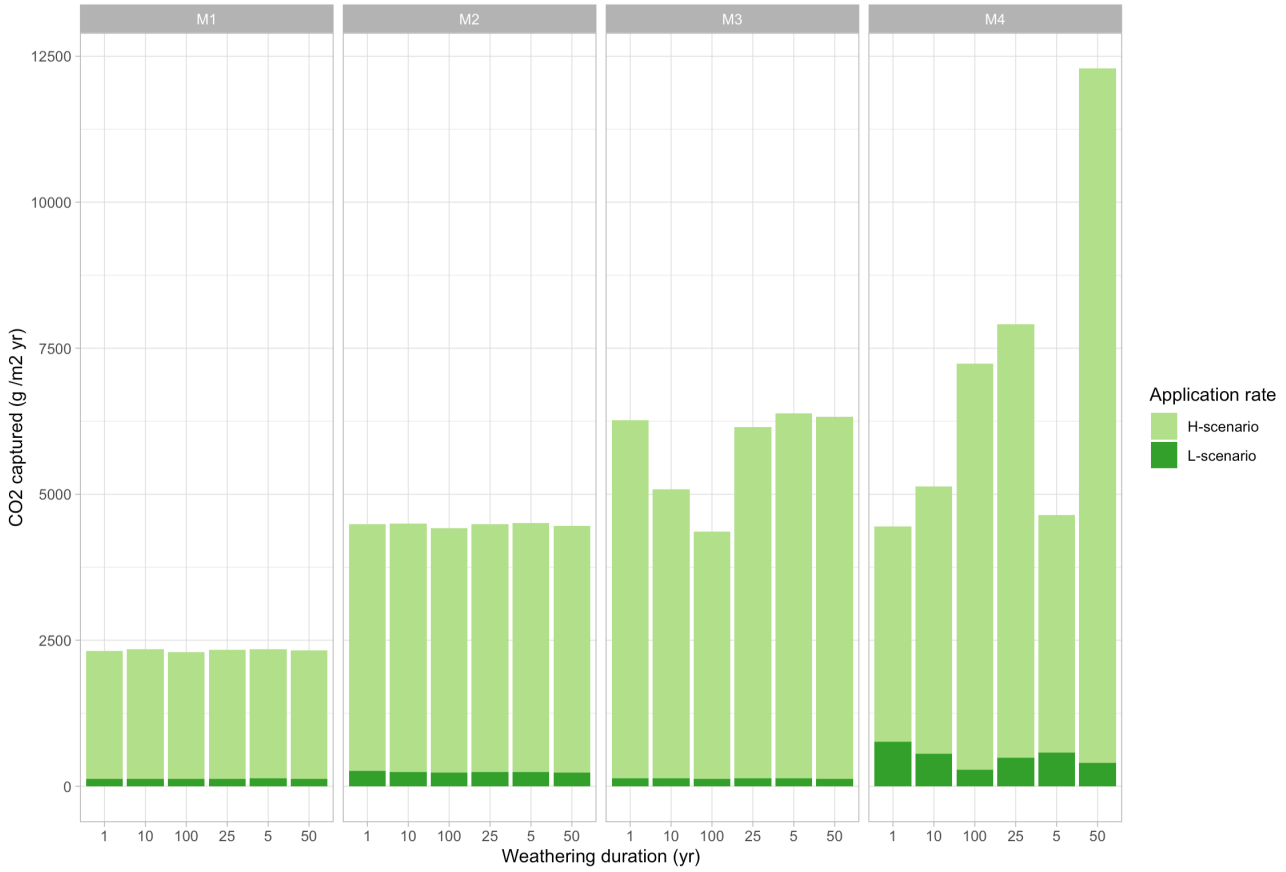


Figure 25: Comparison of annual CDR after a single application of olivine to the soil surface (M1) and into the 0-20 cm soil layer (M2); and of basalt to the soil surface (M3) and into the 0-20 cm soil layer (M4); for 5000 g $m^{-2}$ (L-) and 150000 g $m^{-2}$ (H-) application scenarios for different weathering durations.

# 5 Discussion

## 5.1 M1/M1$_{CEC}$ - Oxisol with an overlying olivine layer

The application of 5000 g m$^{-2}$ of olivine to the soil surface leads to a pH increase with depth (Figure 8a) as expected in studies as protons are consumed during silicate minerals dissolution (e.g. Gillman, 1980; Harley and Gilkes, 1999). Partial dissolution of kaolinite and olivine releases $SiO_{2(aq)}$, $Al^{3+}$ and $Mg^{2+}$ and Fe in the soil solution. Since the %V. of olivine decreases by 1.6% after 100 yr of weathering, our hypothesis to consider 30 annual applications as a single addition of a greater quantity of silicate is justifiable. As $Mg^{2+}$, $SiO_{2(aq)}$, as well as the cations provided by the infiltrating rainfall ($Na^+$, $K^+$ and $Ca^{2+}$) do not precipitate in any secondary solid phase, the concentrations of these species increase with depth because of leaching (Figures 10a and 9a). Since there is no other sources of $Na^+$, $K^+$ and $Ca^{2+}$ than rainfall and noting that the dissolved cation concentrations decrease with time, we conclude that losses through leaching exceed inputs from rainfall.

Despite the continuous precipitation of goethite in the top 3 mm of the soil driven by the release of Fe during olivine dissolution (Figure 9a), the depth over which the precipitation occurs is minute and Fe concentration still increases with depth (Figure 10a). With time, Fe concentration decreases along the entire profile, implying the quantity leached out of the soil is greater than that released during olivine dissolution (Figure 10a). Furthermore, olivine weathering rate slightly decreases with time and hence, the temporal evolution of $Mg^{2+}$ concentration follow that of Fe (Figure 17a). The decrease in chemical weathering rate with time can be explained by various factors, including the decrease of reactive surface area or the approach of equilibrium conditions due to increased solute concentrations (White and Brantley, 2003).

Owing to the low $SiO_{2(aq)}$ concentration in the soil top most 40 cm, the solution is undersaturated with respect to kaolinite (Figure 26), and thus, the clay mineral dissolves (Figure 9a). Kaolinite dissolution drives the release of $Al^{3+}$ into the soil solution which in turn, causes precipitation of gibbsite in the 0-40 cm layer (Figure 9a). Since $SiO_{2(aq)}$ concentration gradually increases with depth (Figure 10a), as olivine is dissolved and the specie is leached, kaolinite becomes stable below 40 cm (Figure 26). As a result, $Al^{3+}$ release is halted and gibbsite is no longer able to form (Figure 9a). It is worth noting that the decrease in $Al^{3+}$ concentration with depth (Figure 10) is likely the consequence of three factors: (i) the solubility of $Al^{3+}$ decreases with increasing pH (Harley and Gilkes, 1999), and here pH increases with depth; (ii) the supersaturation with respect to gibbsite in the first 40 cm of the soil profile removes $Al^{3+}$ from the soil solution as it percolates downward; and (iii) the stabilisation of kaolinite below 40 cm depth, thereby impeding $Al^{3+}$ addition to the soil solution. Although $SiO_{2(aq)}$ concentration increases with depth, allophanes remain below saturation, probably due to decreasing $Al^{3+}$ concentration in the soil solution (Figure 26). The saturation index (SI) of halloysite, amorphous silica and smectite are always negative and these phases cannot precipitate (Figure 26).

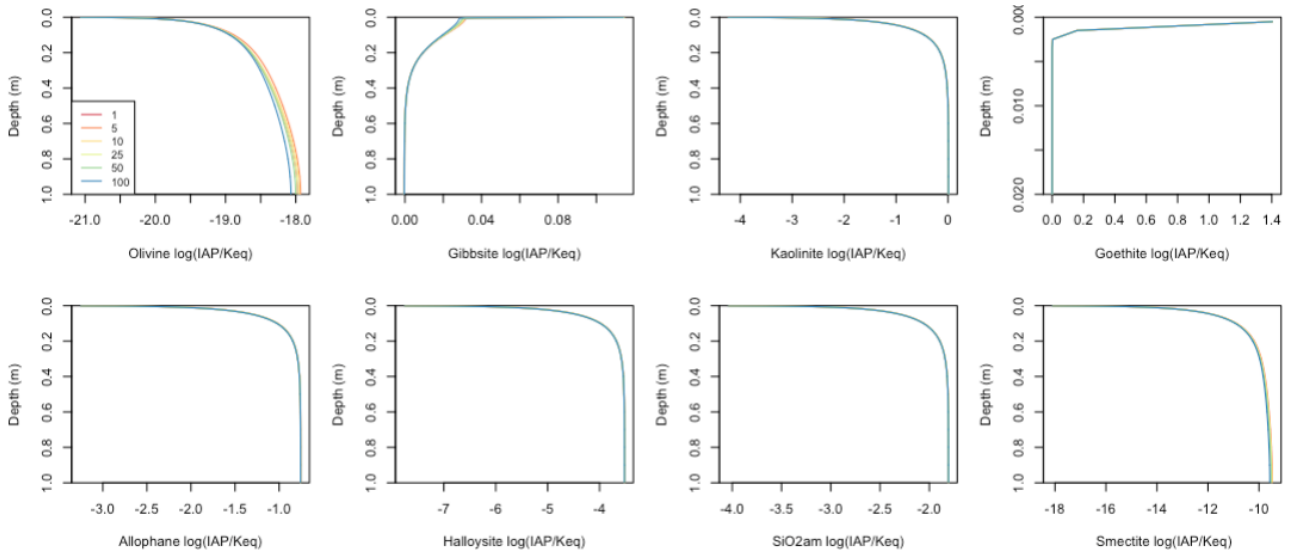


Figure 26: Evolution of the saturation index for primary and secondary solid phases as a function of soil depth and weathering duration after the addition of 5000 g $m^{-2}$ of olivine to the soil surface (M1). The model results with and without ion exchange (CEC) do not differ.

With time, continuous acidity input through infiltrating water flux results in a decrease in the soil solution pH (Figure 8a). This result highlights that for L-olivine, the amount of olivine dissolved is insufficient to buffer the pH against continuous acidity input by rainfall. A faster weathering rate or a higher quantity of olivine would be required to increase the quantity of olivine dissolved and stabilise the pH at a higher value. Thus, our results suggest that the co-benefits to agriculture brought by adding 5000 g $m^{-2}$ of olivine are questionable. Specifically, the pH increase is small (5.63 to 5.7 in the 0-20 cm layer) and there is a limited input of the plant nutrients, apart from a small quantity of $Mg^{2+}$, from olivine dissolution. Clearly, the use of olivine for ESW in tropical soils will not re-establish their $K^+$ depletion (Beerling et al., 2020). Asher (1978) estimated that a minimal concentration of 10-100 $10^{-5}$ and 0.5-1000 $10^{-5}$ mol $L^{-1}$ of $K^+$ and $Ca^{2+}$ respectively are required for the adequate growth of many plants species. However, after olivine application and over 100 yr of weathering, concentrations of $K^+$ and $Ca^{2+}$ never exceed 1.62 $10^{-5}$ and 9.02 $10^{-6}$ mol $L^{-1}$, respectively. The $SiO_{2(aq)}$ released via silicate dissolution may benefit plants as uptake of Si enhances resistance to diseases and drought- and salinity-related stresses (Hartmann et al., 2013).

### Effect of a higher silicate application rate on soil properties

H-olivine increases the soil pH up to neutral values (≈7.1) below the topmost 10 cm over 100 yr of weathering (Figure 8b). Although the dissolution rate of olivine is not affected by the mass load applied to the soil (Figures A.10 and A.11), a higher amount dissolves and more protons are consumed. As a result, the acidity brought by the rain is neutralised. For the same reasons, greater concentrations of Fe and $Mg^{2+}$ are released into the solution. In contrast with the lower olivine amendment, Fe and $Mg^{2+}$ loss through leaching and minor goethite precipitation are balanced by inputs from dissolution (Figure 10b).

The low concentration of $SiO_{2(aq)}$ drives kaolinite dissolution in the 10-20 cm layer, i.e. below the amendment (Figure 10b and 9b). The concomitant release of $Al^{3+}$ also allows gibbsite to precipitate (Figure 9b). The steep decrease in $Al^{3+}$ concentration below 10 cm depth is in agree-

ment with (i) the steep increase in pH to 7.1 at the same depth, which reduces $Al^{3+}$ solubility (Harley and Gilkes, 1999); (ii) precipitation of gibbsite between 10 and 20 cm depth and (iii) stabilisation of kaolinite below 20 cm depth due to increased $SiO_{2(aq)}$ concentration. As a result, $Al^{3+}$ concentration is the highest in the 0-10 cm layer (Figure 10b), although the maximum value decreases with time as the rate of kaolinite dissolution slows down (Figure A.11). Less kaolinite dissolution and gibbsite precipitation occur compared to L-olivine. This is explained by smaller dissolution and precipitation rates (Figures A.10 and A.11), respectively, a result that reflects the pH-dependence of silicate mineral dissolution rates and minimum values at near-neutral pH conditions (Harley and Gilkes, 1999).

H-olivine ESW may produce significant beneficial effects on crop productivity. The availability of nutrients for plants is greatly impacted by soil pH. Key plant nutrients include macronutrients (e.g. N, K, Ca, Mg, P, S), required in plant tissues at concentrations higher than 0.1% dry weight, and additional micronutrients (B, Cl, Co, Fe, Mn, Mo, Ni, Zn), that are needed in smaller amounts (Harley and Gilkes, 1999). The pH values for which the bioavailability of these nutrients is optimum are within the range 6.2-7.3 (except Mo for which an alkaline pH is required (McCauley, 2009); Figure 25). Thus, the near-neutral pH values produced in H-olivine may be favourable to crop growth. However, the constant supply of $Mg^{2+}$ from olivine dissolution may interfere with $Ca^{2+}$ uptake by the plants (ten Berghe et al., 2012; Beerling et al., 2018), eventually leading to $Ca^{2+}$ deficiency since its leaching is not replenished by chemical weathering. While kaolinite dissolution releases $Al^{3+}$ in solution, the low solubility of the cation at near-neutral pH values prevents the build-up of potentially phytotoxic concentrations (i.e. 7.5 $10^5$-1.1 $10^4$ mol $L^1$ at pH<5; Blasberg Pahlsson, 1990).

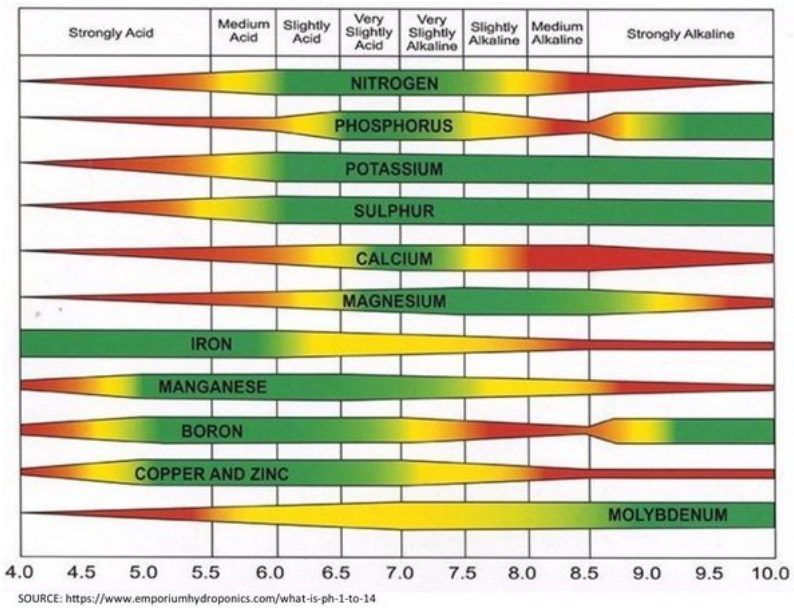


Figure 27: Nutrients availability as a function of pH. N, P, K, S, Ca and Mg are key macronutrients for plants and Mn, B and Mo are micronutrients required in smaller concentrations (Harley and Gilkes, 1999). The pH at which the availability of an element is maximum is shown in green.

### Effect of ion exchange reactions on the soil solution chemistry

As mentioned in section 4.1, ion exchange reactions modulate the concentration distributions of $Ca^{2+}$, $Mg^{2+}$, $Na^{+}$ and $K^{+}$ in the soil solution. Prior to olivine addition (L and H scenarios),

$Ca^{2+}$, $K^+$ and to a lesser extent $Na^+$ dominate the soil exchange complex, but as weathering progresses with time, $Mg^{2+}$ becomes the main cation on the exchange complex and $Ca^{2+}$, $K^+$ and $Na^+$ are released into the solution (Figures 10 and 11). The concentration of a cation present on the exchange complex depends on both its concentration in solution and affinity for the exchange complex. Calcium typically shows the highest affinity for the exchange complex, followed by $Mg^{2+}$, $K^+$ and $Na^+$.

The concentrations of $Ca^{2+}$, $K^+$ and $Na^+$ in the soil solution increase in the first 5 yr of L-olivine weathering (Figure 11a). This reflects replacement on the exchange complex of these cations by $Mg^{2+}$, which is continuously released from olivine dissolution. The magnitude of this process is most important near the surface, where olivine has been applied. Thus, inclusion of ionic exchange reactions in the ESW simulations reveals that more $Ca^{2+}$ and $K^+$ may become available to crops in the first years following olivine amendment because of preferential adsorption of $Mg^{2+}$ on the exchange complex (ten Berghe et al., 2012). However, this effect halts once the exchange complex has been saturated with $Mg^{2+}$. As a result, after 5 yr of weathering, the concentrations of $Ca^{2+}$ and $K^+$ decrease and return to low levels (Figure 10a). Magnesium concentration behaves differently as olivine dissolution continuously adds an excess of the cation to the soil solution. Olivine dissolution rates slows down with time, explaining the decrease in $Mg^{2+}$ in the soil solution between 5 and 10 yr of weathering, as fixation on the exchange continues. The slight increase in dissolved $Mg^{2+}$ noticed until 100 yr of weathering results from a reduced CEC as the amount of kaolinite decreases due to its progressive dissolution during ESW.

Similar processes are identified in the case of the H-olivine scenario, although timing differs. Thus, as a higher amount of $Mg^{2+}$ is released from dissolution, the maximum concentrations of $Ca^{2+}$, $K^+$ and $Na^+$ in the soil solution are reached earlier, i.e. after 1 yr of weathering (Figure 11b). Compared to the H-olivine model without ion exchange reactions, the concentration of $Mg^{2+}$ increases more slowly, because of its preferential adsorption on the exchange complex, but still reaches the same maximum concentration after 100 yr of weathering (Figure 11b). The quantity of $Mg^{2+}$ released thus exceeds the amount captured on the exchange complex. Below 10 cm depth, $Mg^{2+}$ concentration decreases since it is still fixed on the exchange complex but less $Mg^{2+}$ from olivine dissolution reaches these depths. Magnesium concentration increases with time all along the soil profile because, with kaolinite dissolution, the number of exchange site decreases but $Mg^{2+}$ continues to be released by olivine dissolution.

Even though kaolinite CEC predicted decrease is substantial ($\approx$1%), soil CEC is predicted to decrease in both the L- and H-olivine scenarios due to kaolinite dissolution and absence of other secondary clay mineral precipitation (Figure 9). Thus, ESW may eventually reduce the soil's capacity to retain plant nutrients, i.e. a decrease in chemical fertility. While goethite and gibbsite will form upon olivine weathering (Figure 9), they do not contribute to the CEC. These oxides are characterised by a low CEC ($<$5 cmolc $kg^{-1}$), but which strongly depends on variable electrical charges. The solution pH obtained after olivine application is always lower than the PZC of goethite and gibbsite (8.5-9.5) and therefore, these minerals carry a net negative charge (i.e. an anion exchange capacity) (Sposito, 2016).

## 5.2 M2/M2$_{CEC}$ - Oxisol with olivine incorporated into the 0-20 cm top soil layer

The pH increase following olivine application is more important when L-olivine is incorporated in the 0-20 cm layer (6.16 at 1 m depth after 1 yr) than when it is spread over the soil surface (5.83 at 1 m depth After 1 yr) (Figure 8). We suggest that, as the olivine is distributed over a greater depth, the interactions between the mineral and the percolating solution are longer which explains why more olivine is dissolved. With time, continuous acidity input though infiltrating water flux also leads to a decrease in soil solution pH (6.07 after 100 yr).

As for model M1, 1.6% of L-olivine dissolves in 100 yr of weathering, hence, our modelisation of 30 annual applications of L-olivine as a single addition of H-olivine also seems justifiable when the silicate is incorporated (Figure 12a). Iron and $Mg^{2+}$ are released in greater quantity by olivine partial dissolution in the top most 20 cm, which explains the increase in their concentrations in this layer (Figure 13a). Below 20 cm depth, their concentrations are relatively stable with time and depth, showing that the higher input by olivine dissolution nearly balances the loss through leaching and minute goethite precipitation (Figure 12a). The concentration profiles of $Ca^{2+}$, $Na^{+}$ and $K^{+}$ with weathering duration and depth are the same as for model M1 because the only input of those cations is rainfall (Figure 10a and 13a). The application mode of olivine thus has no impact on their concentration in the soil solution. Lastly, soil porosity is also expected to increase.

Aqueous silica is also released through olivine dissolution (Figure 13a). Similar to model M1, owing to the low $SiO_{2(aq)}$ concentration in the soil solution in the top most 40 cm, the solution is undersaturated with respect to kaolinite (Figure A.12), and consequently, the mineral dissolves (Figure 12a). This dissolution occurs over the same depth as the increase in concentration in $SiO_{2(aq)}$ (0-40 cm). Once $SiO_{2(aq)}$ concentration reaches $\approx$4.4 $10^{-5}$ mol $L^{-1}$, kaolinite stabilises. Aluminium is released during kaolinite dissolution, driving the supersaturation with respect to gibbsite in the 0-40 cm layer (Figure A.12). The dissolution of kaolinite is thus coupled with a precipitation of gibbsite at the same depth (Figure 12a). Below 40 cm depth, there is almost no $Al^{3+}$ left in the soil solution because of gibbsite precipitation above this depth alongside the stabilisation of kaolinite and pH increase with depth (Figure 13a). The magnitude of this decreases is stronger for model M2 because the precipitation of gibbsite as well as the pH increase with depth are more important. The precipitation of other secondary solid phases (i.e. halloysite, amorphous silica, smectite and allophanes) cannot occur because their SI are negative (Figure A.12), probably because of the small concentration in $SiO_{2(aq)}$ in solution.

The benefits of L-olivine incorporation for soil fertility and crop productivity in comparison with model M1 are uncertain. The slightly higher pH increase to slightly acid values in the 0-20 cm layer ($\approx$6) may improve the bioavailability of key plant nutrients (Figure 27). This mode of application thus presents an opportunity to decrease the quantity of olivine needed to reach near-neutral pH values. Higher concentrations of $Mg^{2+}$ and Fe are reached in the 0-20 cm layer. However, as more olivine dissolves, the higher input of $Mg^{2+}$ may enhance the imbalance in plant nutrition between $Ca^{2+}$ and $Mg^{2+}$ (ten Berghe, 2012), as $Ca^{2+}$ concentration in the soil solution remains unchanged between M1 and M2. The deficit of $Ca^{2+}$ and $K^{+}$ is still not solved by olivine incorporation, since the actions are only provided through rainfall.

### Effect of a higher application rate on soil properties

H-olivine increases the soil pH up to neutral values (7.5) below the topmost 20 cm over 100 yr of weathering (Figure 8). A higher amount of olivine dissolves compared to when it is spread on the soil surface or for L-olivine incorporated, thereby consuming a higher amount of protons. The pH is stable over time showing that the acidity brought by rain is neutralised over 100 yr of weathering. Owing to the higher quantity of olivine dissolved, $Mg^{2+}$ and Fe reach higher concentrations and loss through leaching and goethite precipitation are balanced by inputs from olivine dissolution (Figure 13b). For the same reason, $SiO_{2(aq)}$ concentrations increases faster and reaches 4.4 $10^{-5}$ mol $L^{-1}$ at 20 cm depth. As a consequence, kaolinite dissolution and concomitant $Al^{3+}$ release and gibbsite precipitation occur in the 0-20 cm layer, a thinner depth than for L-olivine (Figure 12b). Since less gibbsite precipitates, the concentration of $Al^{3+}$ increases up to 20 cm depth, because of leaching and kaolinite dissolution (Figure 13b). Below 20 cm depth, $Al^{3+}$ concentration is stable probably because the loss through leaching, reduced solubility and gibbsite precipitation is balanced by the inputs of the cation.

The beneficial effects of the incorporation of H-olivine are similar to those brought forward for its application to the soil surface. The pH increase is slightly higher (7.5 and 7.1 when incorporated and on the soil surface, respectively) and within the optimal pH range for nutrients bioavailability. Consequently, H-olivine incorporated will also be favourable to plant growth. However, as mentioned for L-olivine, the quantity of olivine dissolved increases with the incorporation of the silicate and thus, $Ca^{2+}$ deficiency in plants may be enhanced compared with the application to the soil surface.

### Effect of ion exchange reactions on the soil solution chemistry

The dynamic of ion exchange reactions are the same as those observed for model M1. $Na^+$, $K^+$ and $Ca^{2+}$, which are initially present on the exchange complex, are gradually replaced by $Mg^{2+}$, which is released during olivine dissolution. Therefore, their concentration are higher than without ion exchange reactions, whereas $Mg^{2+}$ concentration is lower (Figures 13 and 14). The concentrations of $Na^+$, $K^+$ and $Ca^{2+}$ in the soil solution increase in the first 5 yr of L-olivine weathering (Figure 14a), reflecting replacement on the exchange complex of these cations by $Mg^{2+}$. The magnitude of this process is more important in the 0-20 cm layer, where olivine is applied. The inclusion of ion exchange reactions in the simulations shows that more $Ca^{2+}$ and $K^+$ may become available to crops in the first years of weathering. However, once the exchange sites have been saturated, the concentrations of $Na^+$, $K^+$ and $Ca^{2+}$ decrease with time along the entire weathering profile to reach profiles similar to those observed for the simulations without ion exchange reactions, because there are no new input of these cations on the long term apart from rainfall (Figures 13 and 14). Similar dynamics are identified for the H-olivine scenario with a different timing. The maximum concentrations of $Na^+$, $K^+$ and $Ca^{2+}$ are reached more rapidly (i.e. after 1 yr of weathering) because more $Mg^{2+}$ is released from the outset of the weathering period and thus the exchanges on the exchange complex occur more rapidly (Figure 14b).

In contrast with the results obtained for model M1 where $Mg^{2+}$ concentration increased only occurred for H-olivine, here, $Mg^{2+}$ concentration increases along the entire soil profile, regardless of the applied quantity (Figure 14b). The quantity of $Mg^{2+}$ captured on the exchange complex is thus partial and does not significantly reduce the concentration in the soil solution

due to the higher quantity of olivine dissolved. Magnesium concentration decreases with depth as less $Mg^{2+}$ from olivine dissolution reaches these depths and loss through fixation on the exchange complex and leaching continue.

For both application modes and rates, kaolinite CEC is expected to remain low and substantially decrease. Moreover, as the mineral dissolves, the soil's capacity to retain cations from leaching may be reduced. The incorporation of olivine does not lead to an increase in pH to values higher than goethite and gibbsite PZC. As for model M1, both minerals will thus not contribute to the CEC but have an anion exchange capacity (Sposito, 2016).

## 5.3 M3/M3$_{CEC}$ - Oxisol with an overlying basalt layer

L-basalt leads to a higher pH increase (5.87 at 1 m depth) than L-olivine (5.83 at 1 m depth) after 1 yr of weathering when both silicates are applied to the soil surface (Figures 15a and 8a). Although the basaltic rock has a smaller weathering rate than olivine, plagioclase, which is the main dissolving mineral in the basalt, has a higher weathering rate than olivine (Figure 28) and is very abundant initially. As a result, its dissolution consumes more protons and the pH rises to a higher value after one year of weathering. However, with time, pH decreases to reach same value (5.8) for L-olivine and L-basalt after 100 yr of weathering. While olivine weathering rate remains stable with weathering duration (Figure A.10), plagioclase weathering rate decreases strongly with time (Figure 28), and thus the quantity of plagioclase dissolved decreases rapidly. The amount dissolved is not sufficient to buffer the pH against continuous acidity input.

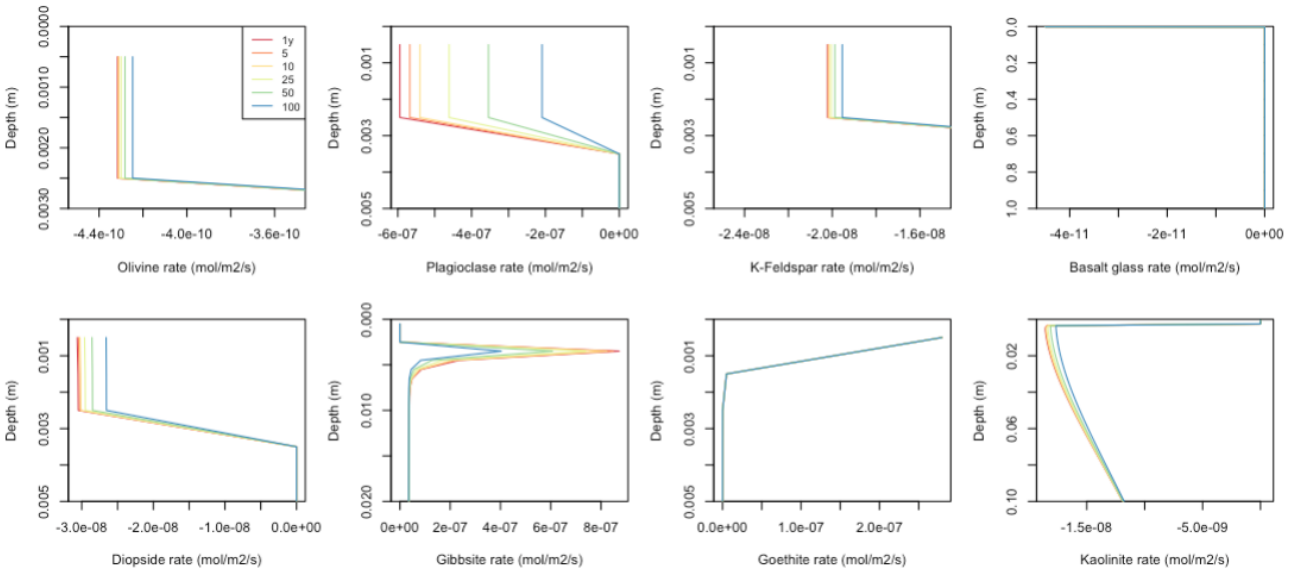


Figure 28: Evolution of the weathering rate of primary and secondary solid phases weathering rate as a function of depth and weathering duration after the application of 5000 g $m^{-2}$ of basalt to the soil surface (M3). The model results with and without ion exchange (CEC) do not differ.

Among the basaltic rock components, the soil solution is undersaturated with respect to plagioclase, K-feldspar, diopside, olivine and basaltic glass (Figure A.13). However, basaltic glass dissolution is not observed during 100 yr of weathering because its weathering rate remains close to 0 during the entire weathering duration (Figure 28). The assumption to consider 30 annual applications as one application of 30 times the quantity is justified because in 1 yr of weathering, less than 0.5 V%. of the basaltic rock dissolves (Figure 16a). Aqueous silica, $Ca^{2+}$,

$Na^+$, $K^+$, $Mg^{2+}$ and $Al^{3+}$ are released during the dissolution of the basaltic rock minerals (i.e. plagioclase, K-feldspar, olivine and diopside). As for models M1 and M2, the low concentration of $SiO_{2(aq)}$ in the top most 40 cm of the soil profile drives the undersaturation with respect to kaolinite (Figure A.13), which dissolves (Figure 16a). Below 40 cm depth, due to the increase in $SiO_{2(aq)}$, kaolinite stabilises (Figure A.13). The $Al^{3+}$ released through plagioclase, K-feldspar and diopside dissolution causes the precipitation of gibbsite below the basalt layer (3-6 mm, SI>0; Figure A.13), in turn driving the strong decrease in the concentration of $Al^{3+}$ below this depth. As more $Al^{3+}$ is released, gibbsite precipitation is more important than when we apply olivine to the Oxisol (Figure 16a). In contrast with M1 and M2, gibbsite precipitation is not linked to kaolinite dissolution. $Al^{3+}$ concentration is constant with depth and weathering duration (Figure 17a), hence, the loss through precipitation of gibbsite above this depth and leaching balances the input by primary solid phases dissolution. Other aluminosilicates cannot precipitate because their saturation index are negative, probably due to the lack of $SiO_{2(aq)}$ in the soil solution. (SI<0; Figure A.13).

Iron released during olivine dissolution drives the precipitation of goethite in the top 3 mm of the soil (Figure 16a). Goethite precipitation occurs over a minute depth, hence, iron concentration still increases with depth, similarly to $Mg^{2+}$, also released by olivine dissolution and which do not precipitate in any secondary solid phase. $Mg^{2+}$ and Fe concentration slowly decrease with weathering durationmeaning the quanitty of the species leached exceed the input by dissolution (Figure 17a). The same dynamics are observed for $K^+$ (from the dissolution of K-feldspar), $Ca^{2+}$ and $Na^+$ (mainly released through plagioclase dissolution). Despite being released during the dissolution of the basaltic rock, $K^+$ and $Na^+$ concentrations are equal to those observed following the application of olivine. Regarding $Ca^{2+}$, its concentration is higher after 1 yr of weathering of L-basalt (≈9.41 $10^{-6}$ mol $L^{-1}$ at 1m depth) than for L-olivine (≈9.02 mol $L^{-1}$ at 1m depth), but reaches the same concentration after 5 yr of weathering. The quantity released of each cation thus is insufficient to exceed the loss through leaching.

Our results suggest that the potential co-benefits for agriculture of L-basalt and L-olivine are similar. As expected in studies, pH increases following basalt application (Shamshuddin et al., 2011; de Oliveira Garcia et al., 2020). However, it does not reach near-neutral values and thus the optimal pH range for nutrients bioavailability in the 0-20 cm layer and strongly decreases with time. Because of leaching, the quantity of $Ca^{2+}$ and $K^+$ released through basalt dissolution does not lead to a significant increase in their concentration in the soil solution compared with concentrations produced solely by rainfall input. As a result, the concentrations of both cations remain inferior to that suggested by Asher (1978) for adequate plants growth. A single application of basalt thus is not sufficient to replenish K-deprived soils.

### Effect of a higher application rate on soil properties

H-basalt increases the soil solution pH up to alkaline values (9.7 after 1 yr of weathering) below 10 cm depth after one year of weathering because of the higher quantity of protons consumed in agreement with the higher amount of basaltic rock dissolved (Figure 15b). However, continuous acidity input through rainfall provokes an important pH decrease (-22%) along the entire soil profile to reach neutral values after 100 yr. The strong decrease in the basaltic constituting solid phases weathering rates cause the quantity of protons consumed during weathering to be insufficient to buffer the pH at a higher value (Figure A.14).

Aqueous silica and $Al^{3+}$ are released in bigger quantities than for the smaller application rate since more material dissolves (Figure 17b). As a result, $SiO_{2(aq)}$ is not limiting anymore for the precipitation of secondary solid phases. The soil solution is supersaturated with respect to kaolinite and allophanes, in addition to gibbsite, in the 10 topmost cm of the soil profile (Figure 29). Only allophanes precipitate in the 0-10 cm layer because there is no kaolinite or gibbsite in the amendment layer (Figure 16b). Kaolinite and gibbsite precipitate at the interface between the amendment layer and the Oxisol profile (Figure 16b). Between 10 and 30 cm depth, gibbsite dissolution is accompanied by kaolinite precipitation (Figure 16b). This result shows that $Al^{3+}$ became limiting for the precipitation of gibbsite (SI<0; Figure 29) but enough $Al^{3+}$ and $SiO_{2(aq)}$ cause the precipitation of kaolinite. Because of the precipitation of the 3 secondary solid phases, a strong decrease is observed in $SiO_{2(aq)}$ and $Al^{3+}$ concentrations below 20 cm depth (Figure 17b). With time, their concentrations decrease all along the profile because the dissolution rates of the providing minerals decrease (Figure A.14) and leaching continues at the same speed. It is interesting to see that after 100 yr of weathering, $Al^{3+}$ concentration reaches 0 along the entire profile, highlighting that it is the limiting element for the precipitation of more secondary solid phases as some $SiO_{2(aq)}$ remains. This result may also be due to the neutral to alkaline pH reached below the amendment layer (Figure 15b).

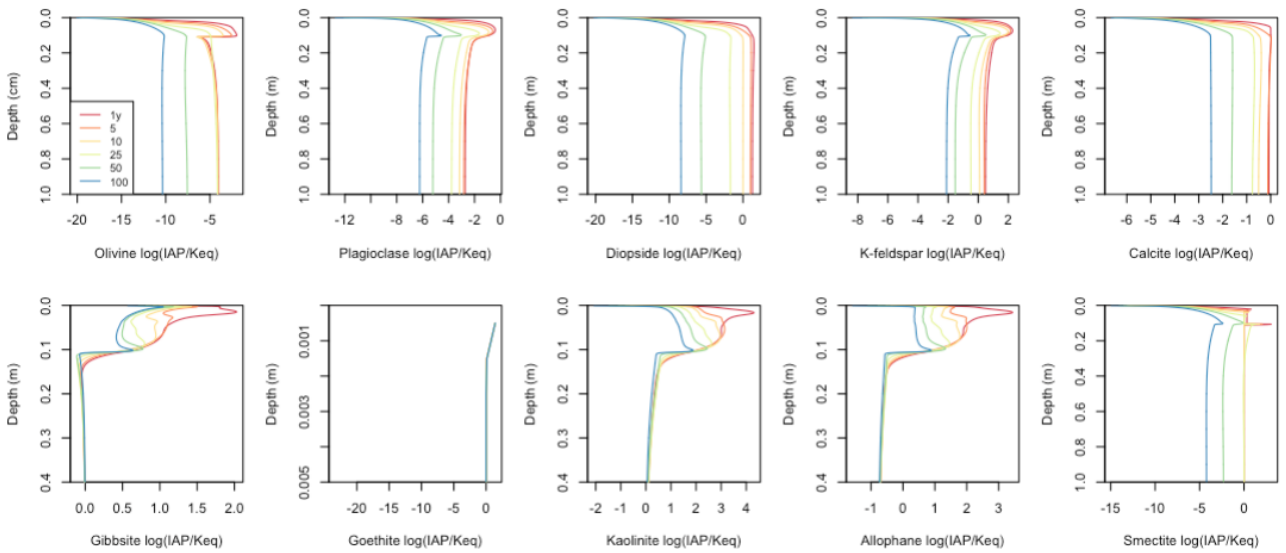


Figure 29: Evolution of the saturation index of primary and secondary solid phases as a function of soil depth and weathering duration of after the application of 150000 g $m^{-2}$ of basalt to the soil surface (M3). The model results with and without ion exchange (CEC) do not differ.

As for all simulations, olivine dissolution releases Fe and $Mg^{2+}$ in the soil solution. The released Fe at the top of the profile drives the supersaturation of the soil solution with respect to goethite (Figure 29), and thus, the clay mineral precipitates (Figure 16b). It has been showed in the previous models that this precipitation is minute and does not induce a decrease in Fe concentration in the rest of the soil profile. The decrease in Fe concentration with depth is thus due to another process. Owing to the more important concentration in $SiO_{2(aq)}$, $K^+$ and $Ca^{2+}$, the soil solution is supersaturated with respect to smectite (Figure 29). As a result, the aluminosilicate precipitates at the interface between the amendment layer and the soil profile, where most species are released by dissolution of the basaltic rock (Figure 16b). This precipitation is especially important during the first 10 yr of weathering. Afterwards, smectite weathering rate is equal to 0 (Figure A.14) and its saturation becomes negative by 50 yr of weathering (Figure

A.14). A decrease in smectite V%. is showed between 50 and 100 yr of weathering (Figure 16b). As a result, $Mg^{2+}$ and Fe concentrations decrease with depth during the first years of weathering before increasing to reach similar profiles as for H-olivine after 100 yr (Figures 10b and 17b).

Among the dissolving minerals of the basaltic rock, plagioclase remains the main dissolving phase and is the main source of $Ca^{2+}$ and $Na^{+}$ (Harley and Gilkes, 1999). Calcium and $Na^{+}$ concentrations increase during the first years of weathering but, as plagioclase weathering rate strongly decreases with time (Figure A.14), their concentration diminishes along the entire soil profile with weathering duration (Figure 17b). Calcite is expected to precipitate because of the high $Ca^{2+}$ concentrations and important amount of $CO_3^{2-}$ in the soil solution driven by the alkaline pH reached (SI>0 at 10 cm depth; Figure 29). During the first 5 years of weathering, $Ca^{2+}$ concentration thus decreases with depth between 10 and 20 cm because of smectite and calcite precipitation, whereas $Na^{+}$ does not precipitate and its concentration remains stable with depth (Figure 17b). Similarly, $K^{+}$, which is released by K-feldspar dissolution, in the soil solution remains low during the first 10 years of weathering because it precipitates in smectite and the quantity released is smaller than for $Ca^{2+}$ (Figure 17b). Potassium concentration then increases with time along the entire profile because (i) smectite precipitation slows down; and (ii) K-feldspar dissolution increases with weathering duration since the weathering front moves downward (Figure 16b), hence, a higher weathering rate is sustained over a deeper depth (Figure A.14).

H-basalt produces more significant benefits for crop productivity and soil fertility than H-olivine. The strongly alkaline pH reached after 1 yr of weathering, may enhance the bioavailability of phosphorus, which limits plant growth due to its important immobility in a wide range of ecosystems (de Oliveira Garcia et al., 2020). Moreover, as pH decreases to reach neutral values after 100 yr of weathering, it enters the optimal pH range for $K^{+}$, $Ca^{2+}$ and $Mg^{2+}$ bioavailability. Repeated addition of 5000 g $m^{-2}$ of basalt during several decades, which is simulated here with H-basalt, could thus be favourable to crop growth. Furthermore, large quantities of $Ca^{2+}$ and $K^{+}$ are released into the soil solution by dissolution of the basaltic rock. After 1 yr of weathering, the concentrations of the interesting elements for plants in the 0-20 cm layer are the following : 1.7 $10^{-4}$ mol $L^{-1}$ of $SiO_{2(aq)}$, 1.5 $10^{-4}$ mol $L^{-1}$ of $Ca^{2+}$, 5.5 $10^{-6}$ mol $L^{-1}$ of $Mg^{2+}$ and 1.6 $10^{-5}$ mol $L^{-1}$ of $K^{+}$, given that $Mg^{2+}$ and $K^{+}$ concentrations increase with time. Calcium concentration is in the minimal concentration range for adequate plant growth proposed by Asher (1978). However, $K^{+}$ remains insufficient and a higher weathering rate or applied quantity would be required to re-establish $K^{+}$ depletion in tropical soils (Beerling et al., 2020). Repeated basalt addition during several decades could thus help provide a slow-release geogenic fertiliser for K-depleted tropical soils and reduce the quantity of conventional fertilisers used, but not be used on its own. Calcium and $Mg^{2+}$ concentrations in the soil solution increase in the same way, hence $Ca^{2+}$ deficiency in plants nutrition could be avoided with H-basalt (ten Berghe et al., 2012). Besides, plants disease and stress resistance may be enhanced in comparison with H-olivine because $SiO_{2(aq)}$ is present in higher concentrations in the soil solution.

An issue that may arise following the application of H-basalt is the expected important decrease in soil porosity (≈-32%) at the interface between the basalt layer and the soil profile. The aqueous chemistry of the soil solution is largely controlled by the dissolution and precipitation of primary and secondary solid phases, respectively, and both processes strongly depend on the hydrological dynamics in the soil profile (Goddéris et al., 2006). The decrease in porosity may

hinder water flow through the soil profile, thereby creating a concentration peak of solute in the amendment layer and decreasing the weathering rates of dissolving silicates material, or it could enhance the interactions between the aqueous solution and solid phases and increase the quantity of material dissolved. The change in porosity could also impact water retention and thus plant growth. It is difficult to precisely predict the consequences of a porosity decrease without a precise pore size distribution.

### Effect of ion exchange reactions on the soil solution chemistry

The addition of ion exchange reaction in the model simulating H-basalt brings out interesting results. Calcium is released in larger quantity through the basaltic rock dissolution, thereby replacing $Mg^{2+}$, $Na^{+}$ and $K^{+}$ on the exchange complex. As a result, inclusion of ionic exchange reactions in the ESW simulations reveals that more $Mg^{2+}$ and $K^{+}$ may become available to crops following basalt amendment because of preferential adsorption of $Ca^{2+}$ on the exchange complex. The concentrations of $Mg^{2+}$ and $K^{+}$ then decrease with time as their inputs decrease and the loss through leaching remains stable. The concentration decrease of $Ca^{2+}$ below 10 cm depth observed after 1 yr of weathering is more important than for the simulation without ion exchange as, in addition to precipitating in calcite and smectite, it is fixated on the exchange complex (Figures 17b and 18b). $Ca^{2+}$ concentration decreases with time along the entire profile because (i) it is increasingly fixed on the exchange complex as soil's CEC is expected to increase; (ii) the dissolution rates of the source minerals decrease with weathering duration; and (iii) continuous leaching. Nevertheless, $Ca^{2+}$ concentration remains at the same level as for H-basalt without ion exchange and are thus sufficient for plant growth, indicating that the amount released largely exceed the amount captured by the exchnage complex.

An increase in the soil's CEC is expected after the addition of H-basalt to the soil surface, as opposed to the results for the application of L- and H-olivine and L-basalt scenarios. The model takes into account smectite, as it precipitates, and kaolinite to compute the CEC (Figure 16b). Both minerals CEC depends mainly on variable electrical charge. With the important pH increase expected, the number of deprotonated chemical functions is expected to rise, hence, their CEC is expected to increase (Figure 19). Moreover, smectite and kaolinite both precipitate at the interface between the amendment layer and the soil profile (10-20 cm). Consequently, the soil's CEC is predicted to increase the most at this depth. While the pH increase associated with H-basalt ensures the bioavailability of the nutrients released during dissolution, an increase in the CEC in the top most 20 cm is interesting for crop productivity as the soil capacity to retain nutrients against leaching will be enhanced (Shamshuddin et al., 2011) at the depth at which nutrient uptake by plants occur. A high CEC is even more beneficial in high leaching environment such as Oxisols in tropical environments.

The increase in soil CEC could be even higher than the one predicted here. For instance, gibbsite, goethite and allophanes are also predicted to precipitate (Figure 16b) but are not taken into account in the computation of the CEC. While goethite and gibbsite are characterised by a low CEC ($<5$ cmolc $kg^{-1}$), the solution pH obtained following H-basalt application is superior to their PZC (8.5-9.5) in the first years of weathering. Allophanes have a large CEC (20-150 cmolc $kg^{-1}$) and the pH of the soil solution would also reach values superior to their PZC (8-9). The inclusion of allophanes could thus enhance significantly the soil CEC with a marginal contribution of gibbsite and goethite.

## 5.4 M4/M4$_{CEC}$ - Oxisol with basalt incorporated into the 0-20 cm top soil layer

The application of L-basalt into the 0-20 cm soil layer leads to a rapid pH increase to neutral values in the 20 to most cm, whereas when L-basalt was applied to the soil surface pH remained acidic (Figures 15c and 15a). Although the weathering rates of the dissolving minerals are slightly smaller than in model M3 (Figures 28 and 30), more minerals dissolve and thus more protons are consumed. We suggest that this is due to increased reactive surface area and interactions between the percolating solution and the dissolving minerals as they are spread over a wider depth. With time, pH also decreases along the entire soil profile because of the decreasing weathering rates and continuous acidity input by the infiltrating solution.

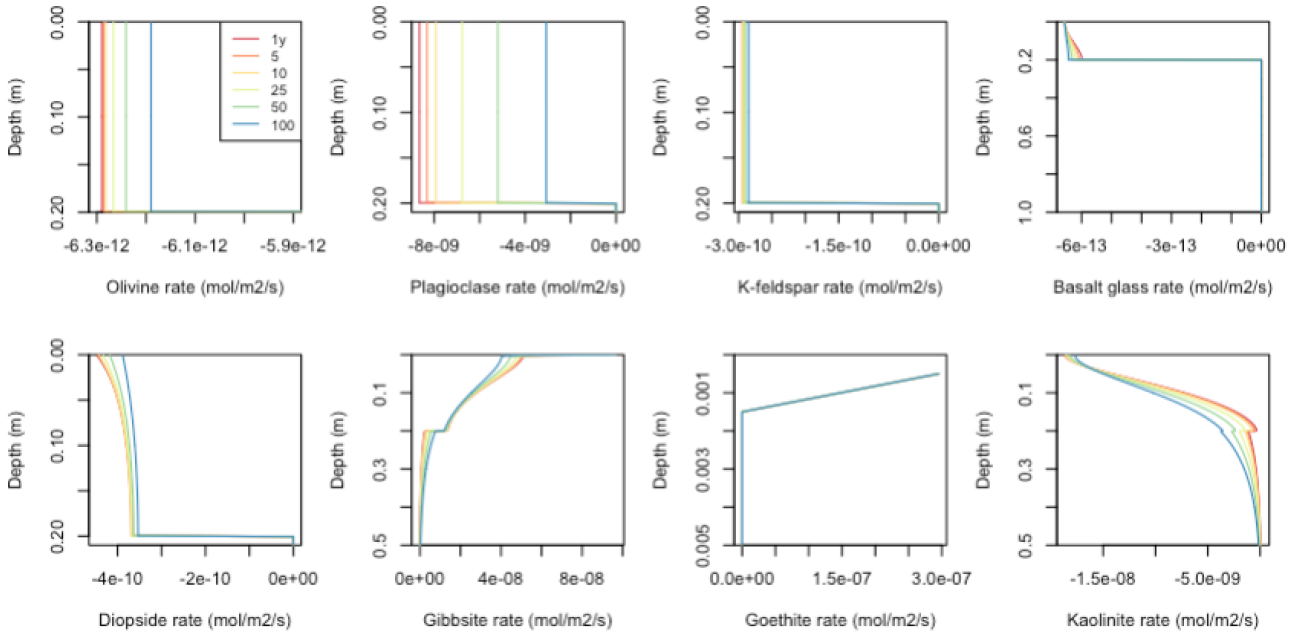


Figure 30: Evolution of the weathering rates of primary and secondary solid phases as a function of soil depth and weathering duration after the application of 5000 g m$^{-2}$ of basalt into the 0-20 cm soil layer (M4). The model results with and without ion exchange (CEC) do not differ.

In the basaltic rock, olivine, plagioclase, K-feldspar and diopside dissolve (Figure 20a). The soil solution is undersaturated with respect to basaltic glass (Figure A.15) but its dissolution is not observed in 100 yr because is weathering rate remains close to 0 (Figure 30). Aqueous silica and $Al^{3+}$ are released during the dissolution of the basaltic rock. The low $Si0_{2(aq)}$ concentration in the soil solution in the top most 40 cm drives the undersaturation with respect to kaolinite in this soil layer (Figure A.15), in turn causing the release of $Al^{3+}$ during its dissolution. Gibbsite precipitates in the 0-40 cm because of the $Al^{3+}$ released by all the dissolving solid phases (Figure 20a). Aqueous silica concentration gradually increases with depth as the specie is released during dissolution and leached (Figure 21a), hence, kaolinite stabilises below 40 cm depth (Figure A.15). Aluminium concentration decrease with depth may be the consequence of the following factors : (i) the increasing pH with depth reduces $Al^{3+}$ solubility (HArley and Gilkes, 1999); (ii) gibbsite precipitation removes the specie from the percolating water; and (iii) less $Al^{3+}$ from the basaltic rock dissolution occurring in the 0-20 cm reaches these depths (Figure 21a). Other secondary solid phases cannot precipitate because their saturation index are negative (Figure A.15).

Although Fe released during olivine dissolution causes goethite to precipitate continuously (Figure 20a), the precipitation occurs over a minute depth and Fe concentration still increases with depth (Figure 21a). Magnesium concentration evolution with depth follows that of Fe because it does not precipitate in any secondary solid phase. With time, Fe and $Mg^{2+}$ concentrations decrease along the entire profile, implying that the quantity leached out of the soil is greater than that released during olivine dissolution. Calcium, $Na^+$ and $K^+$ do not precipitate in any secondary solid phase either following L-basalt application. Their concentration thus increase in the 0-20 cm and are stable downward, meaning that the quantity leached balances the inputs (Figure 21a). With time, $Ca^{2+}$ and $Na^+$ concentrations decrease with time along the entire profile because plagioclase weathering rate decreases with time (Figure 30), whereas the concentration of $K^+$ remains rather stable, accordingly with a stable K-feldspar weathering rate (Figures 21a and 30).

The incorporation of L-basalt enhances its potential beneficial effects for agriculture. For the same quantity applied, the higher pH increase allows for neutral values to be reached, within the optimal pH range for nutrients bioavailability. The important quantity of $Ca^{2+}$ released lead to a suitable concentration in solution (1.1-1.6 $10^{-5}$ mol $L^{-1}$) for plant growth (Asher, 1978) and prevent from plants nutrition imbalance to be reached. However, a single addition of L-basalt into the 0-20 cm top soil layer still is insufficient to replenish $K^+$ in deprived soils.

### Effect of a higher application rate on soil properties

H-basalt leads to a pH increase up to strongly alkaline values (10.2) which then decreases to alkaline value in 100 yr of weathering as acidity input continues. Since a higher amount of the basaltic rock dissolves, more $SiO_{2(aq)}$, $Al^{3+}$, $Mg^{2+}$, Fe, $Ca^{2+}$, $Na^+$ and $K^+$ are released into the soil solution (Figure 21b). In the top most 10 cm of the soil, high $Al^{3+}$ release causes the precipitation of gibbsite (Figure A.16). Owing to $SiO_{2(aq)}$ concentration increasing with depth, the soil solution reaches saturation with respect to kaolinite in the 10-60 cm soil layer (Figure A.16). Kaolinite precipitation causes the decrease in concentration in $SiO_{2(aq)}$ and $Al^{3+}$ with time and depth, the latter in turn driving the dissolution of gibbsite between 20 and 60 cm (Figures 20b, 21b and A.16). Owing to the incorporation of H-basalt, kaolinite is authorised to precipitate at the top of the profile and the precipitation of allophanes does not occur because of the insufficient subsisting $Al^{3+}$ concentration after kaolinite precipitation (Figures 21b and A.16). Aqueous silica thus is not the limiting element for the precipitation of allophanes in this case.

The higher concentrations of $K^+$, $Ca^{2+}$, Fe and $Mg^{2+}$ lead to a more significant precipitation of smectite in the incorporation layer (0-20 cm) (Figures 20b and A.16). Consequently, $K^+$, Fe and $Mg^{2+}$ concentration remain low along the entire profile during the first 25 yr of weathering (Figure 21b). Calcium concentration still increases with depth because the quantity released largely exceeds the amount that precipitates in smectite (Figure 21b). With weathering duration, smectite approaches equilibrium and the soil solution becomes undersaturated with respect to the clay mineral after 50 yr of weathering (Figure A.16). As a result, smectite dissolves between 50 and 100 yr of weathering and the concentrations of $K^+$, $Mg^{2+}$ and Fe increase along the entire soil profile (Figures 21b and 20b). The increase in $K^+$ concentration is greater than that of $Mg^{2+}$ and Fe because it also comes from the increase in dissolved K-feldspar with time. The downward displacement of the weathering front means that higher weathering rates are maintained over a greater depth and therefore more K-feldspar dissolves (Figures 20b, A.16

and A.17). Finally, the increase in $Ca^{2+}$ concentration in the soil solution observed between 25 and 50 years of weathering (Figure 21b) is due to the dissolution of calcite that precipitated beforehand, driven by the important amount of $Ca^{2+}$ and $CO_3^{2-}$ in the soil solution (Figure (Figure 20b, 21b and A.17). Calcium concentration decreases with time, implying that the quantity leached is superior to the inputs by smectite and plagioclase dissolution.

The alkaline pH reached with H-basalt are superior to the optimal range for nutrients bioavailability (Figure 27). While an alkaline pH enhances potassium and phosphorus mobility, which are limiting for plant growth especially in tropical environments (de Oliveira Garcia et al., 2020), it may limit the availability of other key plant nutrients such as $Ca^{2+}$ or $Mg^{2+}$. H-basalt weathering still provides large quantities of $K^+$, $Mg^{2+}$ and $Ca^{2+}$ to the soil solution which is favourable to plant growth. However, the maximum concentration of $K^+$ remains inferior to the minimum stated by Asher (1978) for adequate plant growth. As all cations are released continuously, nutrition imbalance in plants between $Ca^{2+}$ and Mg2+ should not be problematic (ten Berghe et al., 2012).

#### Effect of ion exchange reactions on the soil solution chemistry

The inclusion of ion exchange in the simulations of L-basalt and H-basalt incorporated into the soil produces similar results to that of H-basalt applied to the soil surface. Calcium replaces $Mg^{2+}$, $K^+$ and $Ca^{2+}$ on the exchange complex because of the high quantity released. Consequently, additional $K^+$ and $Mg^{2+}$ are available to plants during the first years of weathering. With time, the concentration profiles of all species approach those without ion exchange because the exchange sites are saturated with $Ca^{2+}$ and all the K+, $Mg^{2+}$ and $Na^+$ initially present have been released.

The application of H-basalt also leads to an increase in soil's CEC for two reasons (Figure 23): (i) kaolinite and smectite CEC is expected to increase ($\approx$+11%) owing to the alkaline pH reached causing additional exchange sites to be deprotonated; and (ii) the precipitation of smectite and kaolinite at the top of the profile. The soil capacity to retain nutrients from leaching may thus be enhanced following repeated basalt application. The increase in soil CEC is expected in the entire 0-20 cm layer, whereas when H-basalt is applied to the soil surface, it is predicted to occur only at 10 cm depth. However, since no allophanes precipitate, the increase in CEC might be in reality smaller here than when H-basalt is applied to the soil surface. This effect is difficult to estimate without running simulations with allophanes considered in ion exchange reactions.

## 5.5 Carbon dioxide removal potential

The annual CDR following olivine addition remains relatively stable with time (Figures 24a and 25; Table A.2), probably because the rate of olivine weathering decreases little with weathering duration (Figure A.10 and A.11). As olivine dissolves at a slower rate than plagioclase, which is the main dissolving phase in basalt, more reactive surface area might remain available over a longer period of time. In contrast, annual CDR using basalt decreases more importantly with weathering duration. This may be due to the combined effect of significant reduction in plagioclase weathering rate with time (e.g. Figure 28) and shrinking of the reactive surface area following rapid dissolution in the first years of weathering.

Our modelling results indicate higher CDR in L-basalt than in L-olivine, regardless of the application mode (i.e. surface vs. incorporation) and weathering duration. This contrasts with previous claims that the $CO_2$ sequestration potential per mass of silicate is higher for olivine than for basalt (Köhler et al., 2010; Strefler et al., 2018). The apparent discrepancy probably originates from the high weathering rate of abundant (30.6 %V.) plagioclases (log k= -10.91 mol $m^{-2}$ $s^{-1}$; Table 4) during the first years of basalt weathering (e.g. Figure 28) compared to that inferred for olivine (log k = -12.47 mol $m^{-2}$ $s^{-1}$; Table 4) over the same period (Figures A.10 and A.11). The same discrepancy is observed for the H-scenarios involving basalt and olivine applied to the soil surface, for all weathering durations. However, when H-olivine is incorporated into the first 20 cm of the soil, its potential CDR is higher than that of H-basalt during the first 5 yr of weathering. We suggest that the initial low CDR of H-basalt is due to calcite precipitation during the first 5 years of weathering, driven by the alkaline pH reached (Figure 20b), which removes $CO_3^{2-}$ from the soil solution, and thus decreases the computed CDR. As calcite dissolves in the following years, H-basalt annual CDR increases importantly. This results highlight the important control of carbonates on $CO_2$ sequestration on a shorter timescale. Since more basalt and olivine dissolve when the silicate is incorporated into the 0-20 cm soil layer, annual CDR is more important for the simulations when the material is incorporated, except for H-basalt during the first 5 years for the same reason. The incorporation of the silicate amendment into the soil thus seems to favourably enhance CDR by ESW and makes it possible to sequester higher amounts of $CO_2$ while applying less silicates into the soil.

A wide range of CDR values are reported for ESW in soils (e.g. Beerling et al., 2018; Amann et al., 2020; Goll et al., 2021; Vienne et al., 2022). However, a comparison is difficult because these estimates correspond to various environmental settings, silicates composition and application modalities. Regarding the use of olivine for ESW, no study evaluate its CDR potential using RTM. Köhler et al. (2010)'s study estimates a CDR potential of 84 g $CO_2$ $m^{-2}$ $yr^{-1}$ following the application of 303 g $m^{-2}$ of olivine to the soil surface in the Amazon river catchment, whereas Strefler et al. (2018)'s shows a $CO_2$ sequestration potential of 12 000 g $m^{-2}$ following the application of 15000 g $m^{-2}$ to croplands. Both studies are solely based on the extrapolation of laboratory weathering rates. Our simulations for L-olivine consider an intermediate application rate of 5000 g $m^{-2}$ and the resulting CDR estimates (125-266 g $CO_2$ $m^{-2}$ $yr^{-1}$) are within the wide range of estimations proposed by these two studies.

For ESW involving basalt addition at a rate similar to our L-scenario, CDR is expected to vary between 45 and 1572 g $CO_2$ $m^2$ $yr^1$ following estimates based on basalt weathering rates (Beerling et al., 2018; Goll et al., 2021). Our Crunchflow simulations suggest CDR values of 126-758 g $CO_2$ $m^{-2}$ $yr^{-1}$, i.e. estimates that fall within previous suggestions. Only a few authors have applied a reactive transport model to assess the CDR potential of ESW. The closest study is that of Vienne et al. (2022) who used PHREEQC to reproduce results obtained from a mesocosm experiment in which 5000 g $m^{-2}$ of crushed basalt were incorporated into the first 20 cm of a Belgian alkaline soil. This setup, including basalt composition, is similar to the conditions imposed in our M4 simulation. Vienne et al. (2022) predict a CDR in the range 183-448 g $CO_2$ $m^2$ $yr^1$ after 1 and 5 yr of weathering, respectively. Our M4 model output (Figure 24b and 25; Table A.2) indicates a much more efficient CDR in the first year of weathering (758.1 g $CO_2$ $m^{-2}$ $yr^{-1}$), but a roughly comparable value is obtained after 5 yr of weathering (579.7 g $CO_2$ $m^{-2}$ $yr^{-1}$). The difference might be due to variations in our modelling approach and parameters since we simulate the amendment of a tropical Oxisol, whereas Vienne et al. (2022) applies basalt to a temperate soil.

Röckstrom (2017) indicates that an annual $CO_2$ sequestration objective of 5 Gt $yr^{-1}$ should be reached by 2050 for CDR methods to contribute significantly to climate change mitigation. Although Röckstrom considers the deployment of various NETs, we can place our results in a context where ESW in highly weathered soils would be the main strategy adopted to remove $CO_2$ from the atmosphere. Our H-scenario simulations represent 30 annual applications of olivine or basalt. If ESW were to be deployed in 2025 and basalt or olivine were applied every year from 2025 to 2055 (during 30 years), the CDR of ESW observed in 2056 would correspond to that of our H-scenario simulations after 1 yr. The sequestration potential of ESW in 2056 would then be on the orders of 2190 and 6130 g $CO_2$ $m^{-2}$ for olivine and basalt, respectively, when applied to the soil surface; and 4220 and 3690 g $CO_2$ $m^{-2}$ for olivine and basalt incorporated into the 0-20 cm layer (Table 6). To reach Röckstrom's proposed objective of 5 Gt $CO_2$ $yr^{-1}$, ESW would have to be deployed over a ≈1.2-2.3 $10^6$ $km^2$-area. This surface area for ESW implementation is largely inferior to that corresponding to warm and humid croplands worldwide (5.1 $10^6$ $km^2$; Strefler et al. 2018). The annual amount of rock needed for ESW would be 6-11.5 Pg of olivine and 4-7 Pg of basalt. Globally, the industries extract ≈50 Pg $yr^{-1}$ of rock for construction, ≈17 Pg $yr^{-1}$ for raw mineral materials and ≈7 Pg $yr^{-1}$ for the cement industry (Beerling et al., 2018). Thus, the silicate amounts required for ESW in soils appear to constitute a relatively small fraction (5.5-15.5%) of what is extracted annually.

Table 6: Evaluation of annual $CO_2$ removal potential after 30 annual applications of 5000 g $m^{-2}$ of olivine to the soil surface (M1) or into the 0-20 cm soil layer (M2) and of basalt to the soil surface (M3) or into the 0-20 cm soil layer (M4); the area of deployment required to reach an annual sequestration of 5 Gt $CO_2$; and the subsequent amount of silicate needed.

| Model and simulation | CDR [g $CO_2$ $m^{-2}$ $yr^{-1}$] in 2056 | Area of deployment [$km^2$] to reach 5 Gt $CO_3$ $yr^{-1}$ CDR objective (Röckstorm, 2017) | Amount of silicate rock/mineral needed [Pg $yr^{-1}$] |
|---|---|---|---|
| M1 H-olivine | 2188 | 2.3 $10^6$ | 11.5 |
| M2 H-olivine | 4220 | 1.2 $10^6$ | 6 |
| M3 H-basalt | 6129 | 0.8 $10^6$ | 4 |
| M4 H-basalt | 3690 | 1.4 $10^6$ | 7 |

## 5.6 Limitations and perspectives

There are limitations to our modelling approach for assessing the CDR potential and side effects on soil of ESW using crushed olivine and basalt. Firstly, we considered a constant annual flow of infiltrating water. However, the rainfall pattern in tropical climates is characterised by a strong seasonality marked by alternating dry and wet periods. Thus, water flow is likely to vary throughout a year, and this could impact the dynamics of dissolution and precipitation of solid phases. For example, the soil solution may become more concentrated during dry months, possibly favouring saturation with respect to some secondary solid phases. Depending on kinetics, once formed, these materials may remain stable (or dissolve slowly) when the soil solution becomes diluted during the wet season. In addition, the hydrological conditions present in the soil profile exerts a major control on weathering rate (Goddéris et al., 2010). For instance, with a smaller water flow, water residence time in the soil profile is increased. Enhanced silicate-water interaction may either increase cation concentration enough to reach solution saturation with respect to other aluminosilicates phases (Perez-Fodich and Derry, 2019) or amplify weathering (Kantola et al., 2017). In contrast, high flow periods would favour undersaturation and dissolution of primary or secondary solid phases that were formed during the dry season. Pref-

erential flow paths in the soil profile also may influence weathering rates (Amann et al., 2020; Perez-Fodich and Derry, 2019), but representing this effect in a reactive transport model is a major challenge that has not yet been satisfactorily addressed.

Another potential issue relates to how our model deals with $P_{CO_2}$ in the soil. We have assumed a soil $P_{CO_2}$ at equilibrium with $CO_2$ in the atmosphere. However, due to plant root and soil microorganism respiration, soil $P_{CO_2}$ may be up to 100 times higher compared to atmospheric levels (Berthelin 1988; Perez-Fodich and Derry, 2019). An increase in soil $P_{CO_2}$ will lead to lower pH values in the soil solution, thereby affecting the carbonate equilibrium system but also enhancing the dissolution of most silicate solid phases. In order to assess how this may alter the weathering of olivine and basalt additions, it would be necessary to reproduce the Crunchflow simulations with a higher $P_{CO_2}$.

Although CrunchFlow offers the possibility to include ion exchange reactions in the equilibrium calculations, the thermodynamic data are limited and only a couple of solid phases (kaolinite, smectite) can be considered to represent the soil CEC and thus, exchange reactions. As a result, the simulations cannot account for the formation of a new CEC when other aluminosilicates form, notably the allophanes. Yet, allophanes have a large CEC (20-150 cmolc $kg^{-1}$) that becomes effective at pH values above their PZC (i.e. 8-9). Our model outputs highlight the possibility for allophane to precipitate in response to basalt addition to soil. Even at solution pH values below allophanes' PZC, a fraction of the potential CEC may be able to accommodate cation exchange reactions. In addition, when allophanes behave as an anion exchange complex (i.e. at pH $<$ PZC), key plant nutrients such as phosphate and sulphate may bind strongly to their surfaces, considerably reducing bioavailability. If this were to occur, ESW using basalt could have a detrimental effect on soil chemical fertility, an outcome that would contradict the common claim that ESW will bring co-benefits to soil quality. The model also does not deal with CEC associated with soil organic matter. Soil organic matter is characterised by a low PZC (3-3.5) and a very large CEC (200-400 cmolc $kg^{-1}$), thereby forming a substantial portion of the CEC. Since some authors suggest that ESW will foster organic matter stabilisation (e.g. Peña-Ramírez et al., 2009; de Oliveira Garcia et al., 2020), more investigations are needed to assess repercussions on ion exchange dynamics, and subsequent ion concentrations in the soil solutions. In addition, the presence of dissolved organic matter may also influence the fate of $Al^{3+}$ in solution, which in turn can have an effect on the rate at which aluminosilicate phases dissolve as water flows through the soil.

Furthermore, we could not simulate repeated annual application of silicates to the soil with CrunchFlow. For instance, it was not possible to take the physical and chemical characteristics of the soil profile obtained after one year of weathering (i.e. solid phase abundances, porosity and aqueous chemistry) and add a new amount of amendment to it in order to simulate several annual applications. We thus chose to simulate 30 annual applications of 5000 g $m^{-2}$ of silicates as one addition of 150000 g $m^{-2}$. Although our results show that this assumption is justifiable due to the slow dissolution of silicates (section 5), it would be better to be able to carry out simulations closer to what will occur in practice.

An important source of incertitude in reactive transport models relates to the choice of appropriate thermodynamic and kinetic data, which ultimately control weathering rates (Goddéris et al., 2006). Most of the thermodynamic and kinetic parameters derive from controlled dissolution experiments in the laboratory, although it has long been emphasised that weathering

rates of silicates in the field are several orders of magnitude lower (Brantley et al., 2008). Large uncertainties surround the precipitation kinetics of amorphous or poorly crystallised silicates such as allophanes (Goddéris et al., 2006). In our study, we followed Perez-Fodich and Derry (2019) by using thermodynamic and kinetic parameters describing $SiO_{2(am)}$ to represent allophanes. However, our sensitivity analysis (section 4.5) highlights that changing slightly the solubility of allophanes in the ESW simulation with basalt produces different results. In order to improve our capacity to correctly assess the consequences of basalt-induced ESW on CDR and soil properties, new studies are required to better constrain field weathering rates and amorphous silicates solubility and dissolution/precipitation kinetics.

Another improvement to our modelling approach, would be to integrate biological dynamics and feedbacks such as soil-plants interactions. Numerous studies argue that plants and microorganisms could contribute to accelerate weathering and thus CDR potential of ESW (Lawrence et al., 2014; Kantola et al., 2017; Perez-Fodich and Derry, 2019; de Oliveira Garcia et al., 2020; Goll et al., 2021). For instance, nutrients uptake by plants acts as a sink for the species released during dissolution and thus, could enhance the dissolution of primary solid phases (Kantola et al., 2017; de Oliveira Garcia et al., 2020). Infiltrating water flux and $P_{CO_2}$ in a soil also depend on the standing vegetation type (Goddéris et al., 2006; Goddéris et al., 2010). While biological processes cannot be implemented with CrunchFlow, these dynamics may be integrated through the coupling of the ecohydrological model EcH2O-iso with the reactive transport code Witch, used to simulate chemical weathering along soil profiles, for example (Kuppel, 2019).

Several authors (e.g., ten Berghe et al. 2012) questions the environmental and health risks potentially associated with the use of olivine in ESW as its dissolution may generate elevated concentrations of Ni in the soil solution, with detrimental effects on plants. Although the increase in pH brought by silicate addition should limit the bioavailability of Ni (Kantola et al., 2017), its release may set a limit to the amount of olivine that can be applied for ESW purpose (ten Berghe et al., 2012). This effect could be tested in Crunchflow by modelling the temporal evolution of dissolved Ni upon olivine dissolution, knowing the content of Ni in olivine and choosing an appropriate set of thermodynamic and kinetic parameters.

Finally, our study focuses on the amendment of basalt and olivine to an Oxisol. Other materials for ESW such as mixtures of silicate materials to combine advantages from each of them (Strefler et al., 2018), or excess industrial silicate materials to avoid the need for new mining (Beerling et al., 2020) have also been brought forward and could be tested with RTM, pending on the availability of quantitative mineralogical compositions and adequate thermodynamic and kinetic data. The near-future deployment of ESW in temperate croplands in Europe and the USA is also regarded by some as a real possibility and trials at the crop field scale have just begun (Renforth, 2012; Kantola et al., 2017; Beerling et al., 2020; Kantzas et al., 2022). Typical soils of these regions are Luvisols, classified as Alfisols in the United States soil taxation system (Figure A.2). Clearly, the application of CrunchFlow (or another powerful RTM) to explore ESW in Luvisols treated with olivine or basalt would provide interesting insights that be used to inform strategies for ESW deployment in temperate crop soils. Luvisols clay-fraction is mostly composed of kaolinite, illite and smectite (Conde Bueno et al., 2009). Based on the results of our simulation, H-olivine should induce the dissolution of kaolinite and the precipitation of gibbsite and goethite because of the low $SiO_{2(aq)}$ concentration in solution. In contrast, kaolinite, smectite and allophanes precipitation could be observed following H-basalt application. As a result, soil's CEC may increase and the important amount of key plant nutrients

(i.e. $K^+$, $Ca^{2+}$, $Mg^{2+}$) released during the dissolution should be better retained by the soil. A pH increase should also be expected following H-olivine and H-basalt application and thus, nutrients bioavailability may be enhanced, regardless of the applied material.

# 6 Conclusion

In this study, we used CrunchFlow, a robust RTM, to investigate the effect of crushed silicate addition to an Oxisol to enhance chemical weathering and atmospheric CDR. We tested two silicate compositions, namely olivine and basalt, and two application rates (L- and H-) either added to the soil as a top layer or mixed into the first 20 cm of the soil profile. The simulation results suggest that the CDR potential of ESW in tropical Oxisols is in the range 2172-4188 and 4231-6951 g $CO_2$ $m^{-2}$ $yr^{-1}$ after 30 annual applications of olivine and basalt, respectively, subjected to 100 years of weathering. If ESW were to be deployed extensively across the tropics, this would represent about 3.3-10.4% of the current global anthropogenic emissions (estimated to 3.4 $10^9$ t $CO_2$ $yr^{-1}$ by Ritchie et al., 2020). According to our results, the CDR efficacy of ESW is enhanced when the crushed silicate is incorporated into the top soil layer rather than when it is applied to the soil surface.

The model outputs indicate that repeated application of basalt to an Oxisol is associated with a higher annual CDR compared to olivine, regardless of the weathering duration considered. This probably reflects the presence of abundant plagioclases in basalt that weather quickly. However, the rate of plagioclase weathering decreases with time, thereby gradually slowing down CDR. Such an effect does not affect olivine dissolution and CDR is predicted to remain stable over time when the silicate is added to the Oxisol.

Our calculations show that ESW with olivine and basalt induces a significant increase in the soil solution pH due to proton consumption during silicate dissolution. This effect is much more pronounced in the case of basalt addition as alkaline pH values are predicted to develop as weathering proceeds. The increase in pH in the H-basalt scenario is such that calcite can precipitate, providing a temporarily carbon sink in the soil. Based on our results, we anticipate that basalt application may lead to higher co-benefits for soil fertility (and potentially crop yields) than using olivine for ESW. Basalt dissolution releases significant concentrations of $K^+$, $Ca^{2+}$ and $Mg^{2+}$ into the soil solution. As the pH of the later rises to near-neutral values, these nutrients will be readily available to crop plants. Thus, the application of crushed basalt on Oxisols would help relieve $K^+$ depletion commonly observed in Oxisols. In contrast, an imbalance in plant nutrition may arise following repeated olivine addition due to the continuous $Mg^{2+}$ release that may interfere with $Ca^{2+}$ uptake by plants.

Our modelling study is the first to explicitly consider the potential impact of silicate addition on soil CEC. The deployment of ESW with basalt in Oxisols over several decades induces an increase in CEC due to precipitation of smectite, a secondary solid phase characterised by a relatively high CEC. The development of a new CEC in response to ESW would decrease nutrient leaching, which is particularly important in tropical environments, and thereby increase soil chemical fertility. However, this beneficial effect is not observed when olivine is used for ESW and, in fact, a decrease in CEC may occur due to the dissolution of the Oxisol kaolinite during weathering. As with the CDR efficacy, the improvement of soil fertility is maximised when crushed basalt is ploughed into the top 20 cm of soil.

While our modelling study sheds new light on the factors that modulate the potential of ESW to remove $CO_2$ from the atmosphere and improve soil fertility, it also contains simplified assumptions and limitations. For instance, calculations should be reproduced at higher soil $P_{CO_2}$ to account for plant and microorganism respiration. We also did not represent the likely sea-

sonal variations in the water flux infiltrating into the soil. Some uncertainties also remain regarding the robustness of the kinetic and thermodynamic parameters used for simulating the weathering of olivine and basalt. In theory, and pending further work, these aspects could be dealt with in Crunchflow.

Finally, any ESW study based on an RTM would certainly benefit from a comparison with data acquired through a long-term in situ ESW experiment. For example, this would allow us to validate the silicate weathering rates inferred theoretically and better assess the actual co-benefits of ESW to soil fertility. Nevertheless, RTM offers a unique tool for exploring ESW in soils under various environmental conditions, soil properties and silicate application modalities.

# References


Aagaard, P., & Helgeson, H. C. (1982). Thermodynamic and kinetic constraints on reaction rates among minerals and aqueous solutions; I, Theoretical considerations. American Journal of Science, 282(3), 237–285.

Alves, M. E., & Omotoso, O. (2009). Improving Rietveld-Based Clay Mineralogic Quantification of Oxisols Using Siroquant. Soil Science Society of America Journal, 73(6), 2191–2197.

Amann, T., Hartmann, J., Struyf, E., De Oliveira Garcia, W., Fischer, E. K., Janssens, I., Meire, P., & Schoelynck, J. (2020). Enhanced Weathering and related element fluxes - A cropland mesocosm approach. Biogeosciences, 17(1), 103–119.

Anda, M., Shamshuddin, J., & Fauziah, C. I. (2015). Improving chemical properties of a highly weathered soil using finely ground basakt rocks. CATENA, 124, 147–161.

Anda, M., Shamshuddin, J., & Fauziah, C. I. (2013). Increasing negative charge and nutrient contents of a highly weathered soil using basalt and rice husk to promote cocoa growth under field conditions. Soil and Tillage Research, 132, 1–11.

Anda, M., Shamshuddin, J., Fauziah, C. I., & Omar, S. R. S. (2009). Dissolution of ground basalt and its effect on oxisol chemical properties and cocoa growth. Soil Science, 174(5), 264–271.

Aradóttir, E. S. P., Sonnenthal, E. L., & Jónsson, H. (2012). Development and evaluation of a thermodynamic dataset for phases of interest in CO2 mineral sequestration in basaltic rocks. Chemical Geology, 304–305, 26–38.

Bao, C., Wu, H., Li, L., Newcomer, D., Long, P. E., & Williams, K. H. (2014). Uranium Bioreduction Rates across Scales: Biogeochemical Hot Moments and Hot Spots during a Biostimulation Experiment at Rifle, Colorado. Environmental Science and Technology, 48, 10116–10127.

Basile-Doelsch, I., Balesdent, J., & Pellerin, S. (2020). Reviews and syntheses: The mechanisms underlying carbon storage in soil. Biogeosciences, 17, 5223–5242.

Beerling, D. J., Leake, J. R., Long, S. P., Scholes, J. D., Ton, J., Nelson, P. N., Bird, M., Kantzas, E., Taylor, L. L., Sarkar, B., Kelland, M., DeLucia, E., Kantola, I., Müller, C., Rau, G., & Hansen, J. (2018). Farming with crops and rocks to address global climate, food and soil security. Nature Plants, 4(3), 138–147.

Beerling, D. J., Kantzas, E. P., Lomas, M. R., Wade, P., Eufrasio, R. M., Renforth, P., Sarkar, B., Andrews, M. G., James, R. H., Pearce, C. R., Mercure, J. F., Pollitt, H., Holden, P. B., Edwards, N. R., Khanna, M., Koh, L., Quegan, S., Pidgeon, N. F., Janssens, I. A., ... Banwart, S. A. (2020). Potential for large-scale CO2 removal via enhanced rock weathering with croplands. Nature, 583(7815), 242–248.

Berner, R. A. (1992). Weatehring, plants, and the long-term carbon cycle. Geochimica et Cosmochimica Acta, 56(8), 3225–3231.

Berthelin, J. (1988). Microbial weathering processes in natural envi- ronments. In A. Lerman & M. Meybeck (Eds.), Physical and chemical weathering in geochemical cycles (Kluwer, pp. 33–59).

Biass, S., Bonadonna, C., Connor, L., & Connor, C. (2016). TephraProb: a Matlab package for probabilistic hazard assessments of tephra fallout. Journal of Applied Volcanology, 5(1).

Boucher, O., Randall, D., Artaxo, P., Bretherton, C., Feingold, G., Forster, P., Kerminen, V.-M., Kondo, Y., Liao, H., Lohmann, U., Rasch, P., Satheesh, S. K., Sherwood, S., Stevens, B., & Zhang, X. Y. (2013). Clouds and aerosols. In T. F. Stocker, D. Qin, G.-K. Plattner, M. T. Tignor, S. K. Allen, J. Boschung, A. Nauels, Y. Xia, V. Bex, & P. M. Midgley (Eds.), Climate Change 2013: The Physical Science Basis. Contribution of Working Group I to the

Fifth Assessment Report of the Intergovernmental Panel on Climate Change (Cambridge).
Bourcier, W., Weed, H. C., Nguyen, S. N., Nielson, J. K., Morgan, L., NEwton, L., & Knauss, K. G. (1992). Solution compositional effects on dissolution kinetics of borosilicate glass. International Symposium on Water-Rock Interaction, 81–84.
Boysen, L. R., Lucht, W., Gerten, D., Heck, V., Lenton, T. M., & Schellnhuber, H. J. (2017). The limits to global-warming mitigation by terrestrial carbon removal. Earth's Future, 5(5), 463–474.
Bradford, M. A., Carey, C. J., Atwood, L., Bossio, D., Fenichel, E. P., Gennet, S., Fargione, J., Fisher, J. R. B., Fuller, E., Kane, D. A., Lehmann, J., Oldfield, E. E., Ordway, E. M., Rudek, J., Sanderman, J., & Wood, S. A. (2019). Soil carbon science for policy and practice. Nature Sustainability, 2, 1070–1072.
Brantley, S. L., Kubicki, J. D., & White, A. F. (2008). Kinetics of Water-Rock Interaction.
Brunet, J.-P. L., Li, L., Karpyn, Z. T., Kutchko, B. G., Strazisar, B., & Bromhal, G. (2013). Evolution of Cement Composition and Transport Properties under Conditions Relevant to Geological Carbon Sequestration. Energy & Fuels, 27, 4208–4220.
Buol, S. W., & Eswaran, H. (1999). Oxisols. Advances in Agronomy, 68.
Cailleteau, C., Angeli, F., Devreux, F., Gin, S., Jestin, J., Jollivet, P., & Spalla, O. (2008). Insight into silicate-glass corrosion mechanisms. Nature Materials, 7(12), 978–983.
Canadell, J. G., Monteiro, P. M. S., Costa, M. H., Cotrim da Cunha, L., Cox, P. M., Eliseev, A. V., Henson, S., Ishii, M., Jaccard, S., Koven, C., Lohila, A., Patra, P. K., Piao, S., Rogelj, J., Syampungani, S., Zaehle, S., & Zickfeld, K. (2021). Global Carbon and other Biogeochemical Cycles and Feedbacks. In V. Masson-Delmotte, P. Zhai, A. Pirani, S. L. Connors, C. Péan, S. Berger, N. Caud, Y. Chen, L. Goldfarb, M. I. Gomis, M. Huang, K. Leitzell, E. Lonnoy, J. B. R. Matthews, T. . K. Maycock, T. Waterfield, O. Yelekçi, R. Yu, & B. Zhou (Eds.), Climate Change 2021: The Physical Science Basis. Contribution of Working Group I to the Sixth Assessment Report of the Intergovernmental Panel on Climate Change (Cambridge, pp. 673–816).
Carroll, D. (1959). Ion exchange in clays and other minerals. Bulletin of the Geological Society of America, 70, 749–780.
Ciais, P., Sabine, C., Bala, G., Bopp, L., Brovkin, V., Canadell, J., Chhabra, A., DeFries, R., Galloway, J., Heimann, M., Jones, C., Quéré, C. Le, Myneni, R. B., Piao, S., & Thornton, P. (2013). Carbon and Other Biogeochemical Cycles. In T. F. Stocker, D. Qin, G.-K. Plattner, M. Tignor, S. K. Allen, J. Boschung, A. Nauels, Y. Xia, V. Bex, & P. M. Midgley (Eds.), Climate Change 2013: The Physical Science Basis. Contribution of Working Group I to the Fifth Assessment Report of the Intergovernmental Panel on Climate Change (Cambridge).
Colbourn, G., Ridgwell, A., & Lenton, T. M. (2015). The time scale of the silicate weathering negative feedback on atmospheric CO2. Global Biogeochemical Cycles, 29(5), 583–596.
Conde Bueno, P., Rubí, J. A. M., Giménez, R. G., & Ballesta, R. J. (2009). Impacts caused by the addition of wine vinasse on some chemical and mineralogical properties of a Luvisol and a Vertisol in La Mancha (Central Spain). Journal of Soils and Sediments, 9, 121–128. Crovisier, J.-L., Honnorez, J., Fritz, B., & Petit, J.-C. (1992). Dissolution of subglacial volcanic glasses from Iceland: laboratory study and modelling. Applied Geochemistry, 7, 55–81.
de Coninck, H., Revi, A., Babiker, M., Bertoldi, P., Buckeridge, M., Cartwright, A., Dong, W., Ford, J., Fuss, S., Hourcade, J.-C., Ley, D., Mechler, R., Newman, P., Revokatova, A., Schultz, S., Steg, L., & Sugiyama, T. (2018). Strengthening and Implementing the Global Response. In V. Masson-Delmotte, P. Zhai, H.-O. Pörtner, D. Roberts, J. Skea, P. R. Shukla, A. Pirani, W. Moufouma-Okia, C. Péan, R. Pidcock, S. Connors, J. B. R. Matthews, Y. Chen, X. Zhou, M. I. Gomis, E. Lonnoy, T. Maycock, M. Tignor, & T. Waterfield (Eds.), Global

Warming of 1.5°C. An IPCC Special Report on the impacts of global warming of 1.5°C above pre-industrial levels and related global greenhouse gas emission pathways, in the context of strengthening the global response to the threat of climate change, (Cambridge).
de Oliveira Garcia, W., Amann, T., Hartmann, J., Karstens, K., Popp, A., Boysen, L. R., Smith, P., & Goll, D. (2020). Impacts of enhanced weathering on biomass production for negative emission technologies and soil hydrology. Biogeosciences, 17(7), 2107–2133.
Dugdale, R. C., & Wilkerson, F. P. (1998). Silicate regulation of new production in the equatorial Pacific upwelling. Nature, 391, 270–273.
Edwards, D. P., Lim, F., James, R. H., Pearce, C. R., Scholes, J., Freckleton, R. P., & Beerling, D. J. (2017). Climate change mitigation: Potential benefits and pitfalls of enhanced rock weathering in tropical agriculture. Biology Letters, 13(4), 4.
El Swaify, S. A. (1980). Physical and mechanical properties of Oxisols. In Soils with Variable Charge (pp. 303–324).
Fang, Y., Yabusaki, S. B., Morrison, S. J., Amonette, J. P., & Long, P. E. (2009). Multicomponent reactive transport modeling of uranium bioremediation field experiments. Geochimica et Cosmochimica Acta, 73, 6029–6051.
Feng, X. (1993). Surface Layer Effects On Waste Glass Corrosion. MRS Online Proceedings Library, 333, 55–68.
Food and Agriculture Organization of the United Nations [FAO]. (2012). World agriculture towards 2030/2050: the 2012 revision. ESA Working Paper 12-03.
Fuhrman, J., Clarens, A., Calvin, K., Doney, S. C., Edmonds, J. A., O'Rourke, P., Patel, P., Pradhan, S., Shobe, W., & McJeon, H. (2021). The role of direct air capture and negative emissions technologies in the shared socioeconomic pathways towards +1.5 °c and +2 °c futures. Environmental Research Letters, 16(11).
Fuss, S., Jones, C. D., Kraxner, F., Peters, G. P., Smith, P., Tavoni, M., Van Vuuren, D. P., Canadell, J. G., Jackson, R. B., Milne, J., Moreira, J. R., Nakicenovic, N., Sharifi, A., & Yamagata, Y. (2016). Research priorities for negative emissions. Environmental Research Letters, 11(11).
Fuss, S., Lamb, W. F., Callaghan, M. W., Hilaire, J., Creutzig, F., Amann, T., Beringer, T., De Oliveira Garcia, W., Hartmann, J., Khanna, T., Luderer, G., Nemet, G. F., Rogelj, J., Smith, P., Vicente, J. V., Wilcox, J., Del Mar Zamora Dominguez, M., & Minx, J. C. (2018). Negative emissions - Part 2: Costs, potentials and side effects. Environmental Research Letters, 13(6), 2016–2050.
Gillman, G. P. (1980). The Effect of Crushed Basalt Scoria on the Cation Exchange Properties of a Highly Weathered Soil. Soil Science Society of America Journal, 44(3), 465–468.
Gíslason, S. R., & Oelkers, E. H. (2003). Mechanism, rates, and consequences of basaltic glass dissolution: II. An experimental study of the dissolution rates of basaltic glass as a function of pH and temperature. Geochimica et Cosmochimica Acta, 67(20), 3817–3832.
Goddéris, Y., François, L. M., Probst, A., Schott, J., Moncoulon, D., Labat, D., & Viville, D. (2006). Modelling weathering processes at the catchment scale: The WITCH numerical model. Geochimica et Cosmochimica Acta, 70(5), 1128–1147.
Goddéris, Y., Williams, J. Z., Schott, J., Pollard, D., & Brantley, S. L. (2010). Time evolution of the mineralogical composition of Mississippi Valley loess over the last 10kyr: Climate and geochemical modeling. Geochimica et Cosmochimica Acta, 74(22), 6357–6374.
Goddéris, Y., Brantley, S. L., François, L. M., Schott, J., Pollard, D., Déqué, M., & Dury, M. (2013). Rates of consumption of atmospheric CO2 through the weathering of loess during the next 100 yr of climate change. Biogeosciences, 10(1), 135–148.
Goll, D. S., Ciais, P., Amann, T., Buermann, W., Chang, J., Eker, S., Hartmann, J., Janssens,

I., Li, W., Obersteiner, M., Penuelas, J., Tanaka, K., & Vicca, S. (2021). Potential CO2 removal from enhanced weathering by ecosystem responses to powdered rock. Nature Geoscience, 14(8), 545–549.

Hangx, S. J. T., & Spiers, C. J. (2009). Coastal spreading of olivine to control atmospheric CO2 concentrations: A critical analysis of viability. International Journal of Greenhouse Gas Control, 3(6), 757–767.

Haraldsen, T. K., & Pedersen, P. A. (2003). Mixtures of crushed rock, forest soils, and sewage sludge used as soils for grassed green areas. Urban Forestry and Urban Greening, 2(1), 41–51.

Harley, A. D., & Gilkes, R. J. (2000). Factors influencing the release of plant nutrient elements from silicate rock powders: A geochemical overview. Nutrient Cycling in Agroecosystems, 56(1), 11–36.

Hartmann, J., Jansen, N., Dürr, H. H., Kempe, S., & Köhler, P. (2009). Global CO2-consumption by chemical weathering: What is the contribution of highly active weathering regions? Global and Planetary Change, 69(4), 185–194.

Hartmann, J., West, A. J., Renforth, P., Köhler, P., De La Rocha, C. L., Wolf-Gladrow, D. A., Dürr, H. H., & Scheffran, J. (2013). Enhanced chemical weathering as a geoengineering strategy to reduce atmospheric carbon dioxide, supply nutrients, and mitigate ocean acidification. Reviews of Geophysics, 51(2), 113–149.

Hartmann, J., Moosdorf, N., Lauerwald, R., Hinderer, M., & West, A. J. (2014). Global chemical weathering and associated p-release - the role of lithology, temperature and soil properties. Chemical Geology, 363, 145–163.

Heck, V., Gerten, D., Lucht, W., & Popp, A. (2018). Biomass-based negative emissions difficult to reconcile with planetary boundaries. Nature Climate Change, 8, 152–155.

Herbillon, A. J. (1988). Introduction to the Surface Charge Properties of Iron Oxides and Oxidic Soils. In Iron in Soils and Clay Minerals (pp. 251–266).

Hillel, D. (1998). Energy of Water into Soil. Environmental Soil Physics, 385–426.

IPCC. (2022a). Summary for Policymakers. In P. R. Shukla, J. Skea, R. Slade, A. Al Khourdajie, R. van Diemen, D. McCollum, M. Pathak, S. Some, P. Vyas, R. Fradera, M. Belkacemi, A. Hasija, G. Lisboa, S. Luz, & J. Malley (Eds.), Climate Change 2022: Mitigation of Climate Change. Contribution of Working Group III to the Sixth Assessment Report of the Intergovernmental Panel on Climate Change (Cambridge, Issue 1, pp. 1–30).

IPCC. (2022b). Summary for policymakers. In H.-O. Pörtner, D. C. Roberts, E. S. Poloczanska, K. Mintenbeck, M. Tignor, A. Alegría, M. Craig, S. Langsdorf, S. Löschke, V. Möller, & A. Okem (Eds.), Climate Change 2022: Impacts, Adaptation and Vulnerability. Contribution of Working Group II to the Sixth Assessment Report of the Intergovernmental Panel on Climate Change (Cambridge, Vol. 9781107025, pp. 3–33).

Johansson, D. J. A., Azar, C., Lehtveer, M., & Peters, G. P. (2020). The role of negative carbon emissions in reaching the Paris climate targets: The impact of target formulation in integrated assessment models. Environmental Research Letters, 15(12).

Kantola, I. B., Masters, M. D., Beerling, D. J., Long, S. P., & DeLucia, E. H. (2017). Potential of global croplands and bioenergy crops for climate change mitigation through deployment for enhanced weathering. Biology Letters, 13(4).

Kantzas, E. P., Val Martin, M., Lomas, M. R., Eufrasio, R. M., Renforth, P., Lewis, A. L., Taylor, L. L., Mecure, J. F., Pollitt, H., Vercoulen, P. V., Vakilifard, N., Holden, P. B., Edwards, N. R., Koh, L., Pidgeon, N. F., Banwart, S. A., & Beerling, D. J. (2022). Substantial carbon drawdown potential from enhanced rock weathering in the United Kingdom. Nature Geoscience, 15(5), 382–389.

Keith, D. W. (2000). Geoengineering the Climate: History and Prospect. Annual Review of

Energy and the Environment, 25.
Kelland, M. E., Wade, P. W., Lewis, A. L., Taylor, L. L., Sarkar, B., Andrews, M. G., Lomas, M. R., Cotton, T. E. A., Kemp, S. J., James, R. H., Pearce, C. R., Hartley, S. E., Hodson, M. E., Leake, J. R., Banwart, S. A., & Beerling, D. J. (2020). Increased yield and CO2 sequestration potential with the C4 cereal Sorghum bicolor cultivated in basaltic rock dust-amended agricultural soil. Global Change Biology, 26, 3658–3676.
Keller, D. P., Lenton, A., Littleton, E. W., Oschlies, A., Scott, V., & Vaughan, N. E. (2018). The Effects of Carbon Dioxide Removal on the Carbon Cycle. Current Climate Change Reports, 4(3), 250–265.
Köhler, P., Hartmann, J., & Wolf-Gladrow, D. A. (2010). Geoengineering potential of artificially enhanced silicate weathering of olivine. Proceedings of the National Academy of Sciences of the United States of America, 107(47), 20228–20233.
Kump, L. R., Brantley, S. L., & Arthur, M. A. (2000). Chemical Weathering, Atmospheric CO2, and Climate. Annual Review of Earth and Planetary Sciences, 28, 611–667.
Kuppel, S. (2019). Cartographie des états hydrologiques de la zone critique. Vers une approche modèle - données.
Lasaga, A. C. (1981). Chapter 4. Transition State Theory. In Kinetics of Geochemical Processes.
Lawford-Smith, H., & Currie, A. (2017). Accelerating the carbon cycle: The ethics of enhanced weathering. Biology Letters, 13(4).
Lawrence, C., Harden, J., & Maher, K. (2014). Modeling the influence of organic acids on soil weathering. Geochimica et Cosmochimica Acta, 139, 487–507.
Leturcq, G., Berger, G., Advocat, T., & Vernaz, E. (1999). Initial and long-term dissolution rates of aluminosilicate glasses enriched with Ti, Zr and Nd. Chemical Geology, 160.
Lewis, A. L., Sarkar, B., Wade, P., Kemp, S. J., Hodson, M. E., Taylor, L. L., Yeong, K. L., Davies, K., Nelson, P. N., Bird, M. I., Kantola, I. B., Masters, M. D., DeLucia, E., Leake, J. R., Banwart, S. A., & Beerling, D. J. (2021). Effects of mineralogy, chemistry and physical properties of basalts on carbon capture potential and plant-nutrient element release via enhanced weathering. Applied Geochemistry, 132(June), 105023.
Li, L., Maher, K., Navarre-Sitchler, A., Druhan, J., Meile, C., Lawrence, C., Moore, J., Perdrial, J., Sullivan, P., Thompson, A., Jin, L., Bolton, E. W., Brantley, S. L., Dietrich, W. E., Mayer, K. U., Steefel, C. I., Valocchi, A., Zachara, J., Kocar, B., ... Beisman, J. (2017). Expanding the role of reactive transport models in critical zone processes. Earth-Science Reviews, 165, 280–301.
Lumsdon, D. G., & Farmer, V. C. (1995). Solubility characteristics of proto-imogolite sols: how silicic acid can de-toxify aluminium solutions. European Journal of Soil Science, 46(2), 179–186.
Ma, T., Jivkov, A. P., Li, W., Liang, W., Wang, Y., Xu, H., & Han, X. (2017). A mechanistic model for long-term nuclear waste glass dissolution integrating chemical affinity and interfacial diffusion barrier. Journal of Nuclear Materials, 486, 70–85.
Maher, K. (2011). The role of fluid residence time and topographic scales in determining chemical fluxes from landscapes. Earth and Planetary Science Letters, 312(1–2), 48–58.
Maher, K., Steefel, C. I., White, A. F., & Stonestrom, D. A. (2009). The role of reaction affinity and secondary minerals in regulating chemical weathering rates at the Santa Cruz Soil Chronosequence, California. Geochimica et Cosmochimica Acta, 73(10), 2804–2831.
Maher, K., & Ulrich Mayer, K. (2019). The art of reactive transport model building. Elements, 15(2), 117–118.
Manning, D. (2008). Biological enhancement of soil carbonate precipitation : Passive removal

of atmospheric CO2. Mineralogical Magazine, 72, 639–649.
Manning, D. A. C. (2015). How will minerals feed the world in 2050? PRoceedings of the Geologists' Association, 126(1), 14–17. Mayer, K. U., Frind, E., & Blowes, D. W. (2002). A numerical model for the investigation of reactive transport in variably saturated media using a generalized formulation for kinetically controlled reactions. Water Resources Research, 38, 1301–1321.
Meysman, F. J. R., & Montserrat, F. (2017). Negative CO2 emissions via enhanced silicate weathering in coastal environments. Biology Letters, 13(4).
Mimura, A. M. S., Almeida, J. M., Vaz, F. A. S., de Oliveira, M. A. . L., Ferreira, C. C. M., & Silva, J. C. J. (2016). Chemical composition monitoring of tropical rainwater during an atypical dry year. Atmospheric Research, 169, 391–399.
Minx, J. C., Lamb, W. F., Callaghan, M. W., Fuss, S., Hilaire, J., Creutzig, F., Amann, T., Beringer, T., De Oliveira Garcia, W., Hartmann, J., Khanna, T., Lenzi, D., Luderer, G., Nemet, G. F., Rogelj, J., Smith, P., Vicente Vicente, J. L., Wilcox, J., & Del Mar Zamora Dominguez, M. (2018). Negative emissions - Part 1: Research landscape and synthesis. Environmental Research Letters, 13(6).
Moosdorf, N., Renforth, P., & Hartmann, J. (2014). Carbon dioxide efficiency of terrestrial enhanced weathering. Environmental Science and Technology, 48(9), 4809–4816.
NASA Goddard Institute for Space Studies [GISS]. (2022). GISS Surface Temperature Analysis (GISTEMP).
Oelkers, E. H., Bénézeth, Pa., & Pokrovski, G. S. (2009). Thermodynamic Databases for Water-Rock Interaction. Reviews in Mineralogy and Geochemistry, 70(1), 1–46.
Oelkers, E. H., & Gíslason, S. R. (2001). The mechanism, rates and consequences of basaltic glass dissolution: I. An experimental study of the dissolution rates of basaltic glass as a function of aqueous Al, Si and oxalic acid concentration at 25°C and pH = 3 and 11. Geochimica et Cosmochimica Acta, 65(21), 3671–3681.
Palandri, J. L., & Kharaka, Y. K. (2004). A compilation of rate parameters of water-mineral interaction kinetics for application to geochemical modeling.
Parkhurst, D. L., & Appelo, C. A. J. (1999). User's guide to PHREEQC (Version 2): a computer program for speciation, batch-reaction, one-dimensional transport, and inverse geochemical calculations. In Water-Resources Investigations Report 99-4259.
Paul, A. (1977). Chemical durability of glasses; a thermodynamic approach. Journal of Materials Science, 12, 2246–2268.
Peña-Ramírez, V. M., Vásquez-Selem, L., & Siebe, C. (2009). Soil organic carbon stocks and forest productivity in volcanic ash soils of different age (1835–30,500 years B.P.) in Mexico. Geoderma, 149(3–4), 224–234.
Perez-Fodich, A., & Derry, L. A. (2019). Organic acids and high soil CO 2 drive intense chemical weathering of Hawaiian basalts: Insights from reactive transport models. Geochimica et Cosmochimica Acta, 249, 173–198.
Pokrovsky, O. S., & Schott, J. (2000). Kinetics and mechanism of forsterite dissolution at 25°C and pH from 1 to 12. Geochimica et Cosmochimica Acta, 64, 3313–3325.
Renforth, P. (2012). The potential of enhanced weathering in the UK. International Journal of Greenhouse Gas Control, 10, 229–243.
Renforth, P. (2019). The negative emission potential of alkaline materials. Nature Communications, 10(1).
Renforth, P., Washbourne, C. L., Taylder, J., & Manning, D. A. C. (2011). Silicate production and availability for mineral carbonation. Environmental Science and Technology, 45(6), 2035–2041.

Riahi, K., Bertram, C., Huppmann, D., Rogelj, J., Bosetti, V., Cabardos, A. M., Deppermann, A., Drouet, L., Frank, S., Fricko, O., Fujimori, S., Harmsen, M., Hasegawa, T., Krey, V., Luderer, G., Paroussos, L., Schaeffer, R., Weitzel, M., van der Zwaan, B., ... Zakeri, B. (2021). Cost and attainability of meeting stringent climate targets without overshoot. Nature Climate Change, 11(12), 1063–1069.

Ritchie, H., Roser, M. & Rosado, P. (2020). $CO_2$ and Greenhouse Gas Emissions. OurWorldInData.org.

Rockström, J., Gaffney, O., Rogelj, J., Meinshausen, M., Nakicenovic, N., & Schellnhuber, H. J. (2017). A roadmap for rapid decarbonization. Science, 335(6331), 1269–1271.

Sanderson, B. M., O'Neill, B. C., & Tebaldi, C. (2016). What would it take to achieve the Paris temperature targets? Geophysical Research Letters, 43(13), 7133–7142.

Schenker, M. B., Pinkerton, K. E., Mitchell, D., Vallyathan, V., Elvine-Kreis, B., & Green, F. H. Y. (2009). Pneumoconiosis from agricultural dust exposure among young California farmworkers. Environmental Health Perspectives, 117(6), 988–994.

Schuiling, R. D., & Krijgsman, P. (2006). Enhanced weathering: An effective and cheap tool to sequester CO 2. Climatic Change, 74(1–3), 349–354.

Shamshuddin, J., Anda, M., Fauziah, C. I., & Omar, S. S. R. (2011). Growth of cocoa planted on highly weathered soil as affected by application of basalt and/or compost. Communications in Soil Science and Plant Analysis, 42(22), 2751–2766.

Shamshuddin, J., & Kapok, J. R. (2010). Effect of Ground Basalt on chemical Properties of an ultisol and oxisol in Malaysia. Pertanika Journal of Tropical Agricultural Science, 33, 7–14.

Smith, P., Adams, J., Beerling, D. J., Beringer, T., Calvin, K. V., Fuss, S., Griscom, B., Hagemann, N., Kammann, C., Kraxner, F., Minx, J. C., Popp, A., Renforth, P., Vicente Vicente, J. L., & Keesstra, S. (2019). Land-Management Options for Greenhouse Gas Removal and Their Impacts on Ecosystem Services and the Sustainable Development Goals. Annual Review of Environment and Resources, 44, 255–286. Sposito, G. (2016). The Chemistry of Soils. Third Edition. (Oxford Uni).

Steefel, C. I. (2008). Geochemical kinetics and transport. Kinetics of Water-Rock Interaction, 545–589.

Steefel, C. I. (2009). CrunchFlow User's Manual.

Steefel, C. I., & Lasaga, A. C. (1994). A coupled model for transport of multiple chemical species and kinetic precipitation/dissolution reactions with application to reactive flow in single phase hydrothermal systems. American Journal of Science, 294, 529–592.

Steefel, C. I., DePaolo, D. J., & Lichtner, P. C. (2005). Reactive transport modeling: An essential tool and a new research approach for the Earth sciences. Earth and Planetary Science Letters, 240(3–4), 539–558. https://doi.org/10.1016/j.epsl.2005.09.017 Stefánsson, A., & Gíslason, S. R. (2001). American Journal of Science. American Journal of Science, 301, 513–556.

Steefel, C. I., Appelo, C. A. J., Arora, B., Jacques, D., Kalbacher, T., Kolditz, O., Lagneau, V., Lichtner, P. C., Mayer, K. U., Meeussen, J. C. L., Molins, S., Moulton, D., Shao, H., Šimůnek, J., Spycher, N., Yabusaki, S. B., & Yeh, G. T. (2015). Reactive transport codes for subsurface environmental simulation. In Computational Geosciences (Vol. 19, Issue 3).

Stocker, T. F., Qin, D., Plattner, G.-K., Alexander, L. V., Allen, S. K., Bindoff, N. L., Bréon, F.-M., Church, J. A., Cubasch, U., Emori, S., Forster, P., Friedlingstein, P., Gillett, N., Gregory, J. M., Hartmann, D. L., Jansen, E., Kirtman, B., Knutti, R., Krishna Kumar, K., ... Xie, S.-P. (2013). Technical Summary. In T. F. Stocker, D. Qin, G.-K. Plattner, M. Tignor, S. K. Allen, J. Boschung, A. Nauels, Y. Xia, V. Bex, & P. M. Midgley (Eds.), Climate Change 2013: The Physical Science Basis. Contribution of Working Group I to the Fifth

Assess- ment Report of the Intergovernmental Panel on Climate Change (Cambridge).
Strefler, J., Amann, T., Bauer, N., Kriegler, E., & Hartmann, J. (2018). Potential and costs of carbon dioxide removal by enhanced weathering of rocks. Environmental Research Letters, 13(3).
Su, C., & Harsh, J. B. (1994). Gibbs free energies of formation at 298 K for imogolite and gibbsite from solubility measurements. 58(6), 1667–1677.
Su, C., & Harsh, J. B. (1998). Dissolution of allophane as a thermodynamically unstable solid in the presence of boehmite at elevated temperatures and equilibrium vapor pressures. Soil Science, 163(4), 299–312.
Taylor, L. L., Quirk, J., Thorley, R. M. S., Kharecha, P. A., Hansen, J., Ridgwell, A., Lomas, M. R., Banwart, S. A., & Beerling, D. J. (2016). Enhanced weathering strategies for stabilizing climate and averting ocean acidification. Nature Climate Change, 6(4),
Techer, I., Advocat, T., Lancelot, J., & Liotard, J.-M. (2001). Dissolution kinetics of basaltic glasses: control by solution chemistry and protective effect of the alteration film. Chemical Geology, 176(1–4), 235–263.
ten Berge, H. F. M., van der Meer, H. G., Steenhuizen, J. W., Goedhart, P. W., Knops, P., & Verhagen, J. (2012). Olivine weathering in soil, and its effects on growth and nutrient uptake in ryegrass (Lolium perenne L.): A pot experiment. PLoS ONE, 7(8).
Torres, M. (2014). Application of Crunch-Flow Routines to Constrain Present and Past Carbon Fluxes at Gas-Hydrate Bearing Sites.
United Nations. (n.d.). What is Climate Change.
United Nations Environment Programme [UNEP]. (2018). The Emissions Gap Report 2018.
Van Straaten, P. (2006). Farming with rocks and minerals: Challenges and opportunities. Anais Da Academia Brasileira de Ciencias, 78(4), 731–747.
Van Wambeke, A., Eswaran, H., Herbillon, A. J., & Comerma, J. (1974). OXISOLS. In Pedogenesis and Soil Taxonomy. II. The Soil Orders (Issue 2, pp. 325–354).
Vanselow, A. P. (1932). Equilibria of the base-exchange reactions of bentonites, permutites, soil colloids, and zeolites. Soil Science, 33(2), 95–114.
Vaughan, N. E., & Gough, C. (2016). Expert assessment concludes negative emissions scenarios may not deliver. Environmental Research Letters, 11(9).
Vienne, A., Poblador, S., Portillo-Estrada, M., Hartmann, J., Ijiehon, S., Wade, P., & Vicca, S. (2022). Enhanced Weathering Using Basalt Rock Powder: Carbon Sequestration, Co-benefits and Risks in a Mesocosm Study With Solanum tuberosum. Frontiers in Climate, 4(May).
Voegelin, A., Vulava, V. M., Kuhnen, F., & Kretzschmar, R. (2000). Multicomponent transport of major cations predicted from binary adsorption experiments. Journal of Contaminant Hydrology, 46, 319–338.
Wanner, C., Eggenberger, U., & Mäder, U. (2012). A chromate-contaminated site in southern Switzerland – Part 2: Reactive transport modeling to optimize remediation options. Applied Geochemistry, 27, 655–662.
Werth, D., & Avissar, R. (2004). The regional evapotranspiration of the Amazon. Bulletin of the American Meteorological Society, 4737–4739.
White, A. F., & Brantley, S. L. (2003). The effect of time on the weathering of silicate minerals: Why do weathering rates differ in the laboratory and field? Chemical Geology, 202(3–4), 479–506.
White, A. F., Schulz, M. S., Stonestrom, D. A., Vivit, D. V., Fitzpatrick, J., Bullen, T. D., Maher, K., & Blum, A. E. (2009). Chemical weathering of a marine terrace chronosequence, Santa Cruz, California. Part II: Solute profiles, gradients and the comparisons of contemporary and long-term weathering rates. Geochimica et Cosmochimica Acta, 73(10), 2769–2803.

Wolery, T. J. (1992). EQ3/6, A Software Package for Geochemical Modeling of Aqueous Systems: Package Overview and Installation Guide (Version 7.0).

Wolff-Boenisch, D., Gislason, S. R., Oelkers, E. H., & Putnis, C. V. (2004). The dissolution rates of natural glasses as a function of their composition at pH 4 and 10.6, and temperatures from 25 to 74°C. Geochimica et Cosmochimica Acta, 68(23), 4843–4858.

Xu, T., Zheng, L., & Tian, H. (2011). Reactive transport modeling for CO2 geological sequestration. Journal of Petroleum Science and Engineering, 78, 765–777.

Yang, L., & Steefel, C. I. (2008). Kaolinite dissolution and precipitation kinetics at 22 ° C and pH 4. 72, 99–116.

Yeh, G.-T., & Tripathi, V. S. (1991). A Model for Simulating Transport of Reactive Multispecies Components: Model Development and Demonstration. Water Resources Research, 27(12), 3075–3094.

Zeebe, R. E., & Wolf-Gladrow, D. (2001). CO2 in Seawater: Equilibrium, Kinetics, Isotopes.

# Appendices

## IPCC mitigation pathways

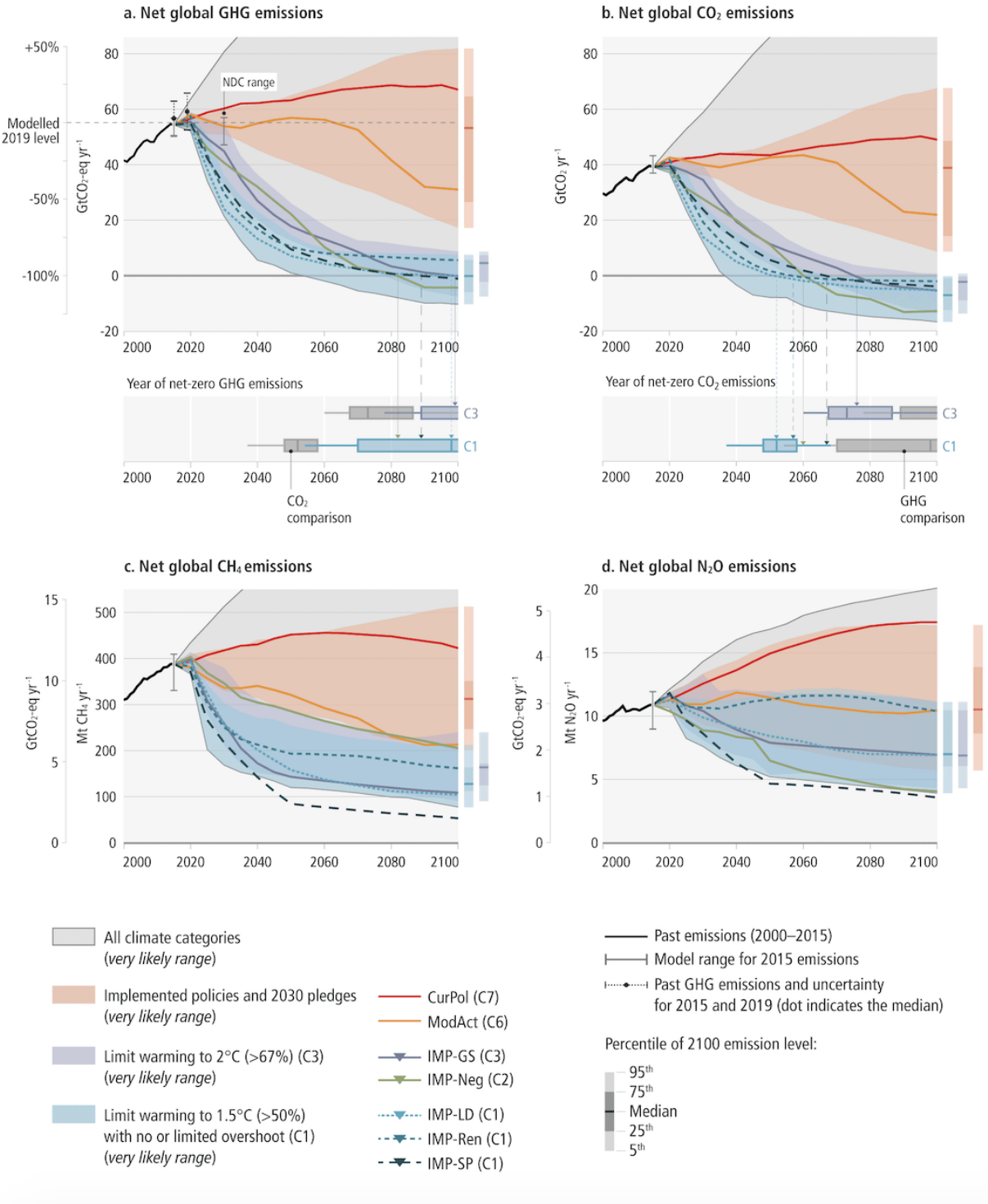


Figure A.1: Modelled mitigation emission pathways (IMPs) for global (a) GHG, (b) $CO_2$, (c) $CH_4$ and (d) $N_2O$ until 2100 (IPCC, 2022a). Pathways named C1 enable to limit warming to 1.5 °C with no overshoot, whereas pathways classified as C2 reach the same goal with an overshoot. Pathway C3 implies limiting global warming to 2 °C and pathways C7 and C6 represent high-emission scenarios.

Working group 3 of the IPCC published in their last report global emissions pathways consistent with the objective to maintain global warming below 2 or 1.5 °C (IPCC, 2022a). Figure 14.a, b, c and d illustrates global GHG, $CO_2$, $CH_4$ and $N_2O$ emissions, respectively. The blue and purple areas represent the range of emissions in which it is very likely to limit warming to 1.5 and 2 °C, respectively. The red area depicts emission pathways following NDC's and policies that were implemented by the end of 2020. The grey area includes all the evaluated pathways. Each pathway focuses on a different aspect to reduce global GHG emissions.

The pathways enabling to limit warming below 1.5 °C with no (named C1) or limited overshoot (C2) are the following:

- **IMP-LD (C1)** concentrates on an efficient resources use and a change in consumption patterns
- **IMP-Ren (C1)** emphasises the use of renewable energies
- **IMP-SP (C1)** illustrates the reduction of inequalities and progress towards sustainable development
- **IMP-Neg (C2)** focuses on the deployment of CDR techniques

Another pathway limiting global warming to 2 °C (classified as C3) is:

- **IMP-GS (C3)** representing a slower introduction of mitigation measures followed by their strengthening

Despite different focuses, all these scenarios rely on a more or less extensive deployment of CDR techniques to counterbalance residual GHG emissions and reach net-zero emissions, as well as deep, rapid and sustained emission reductions in all sectors.

Oxisol worldwide repartition and global croplands with potential for ESW map

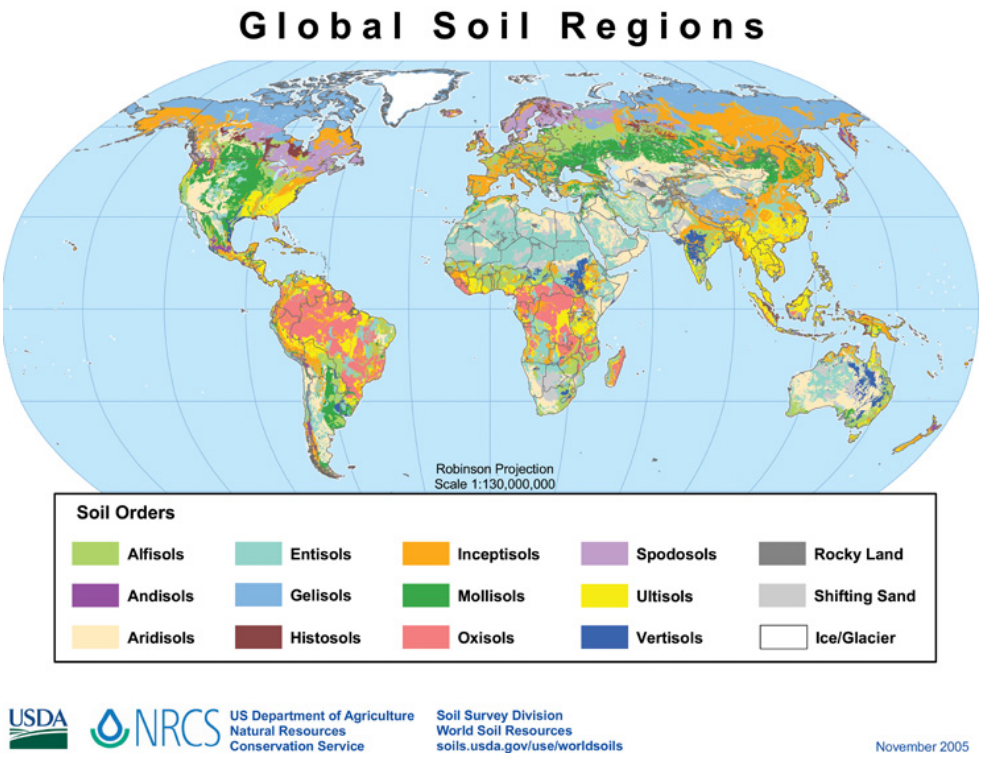


Figure A.2: Global soil classification map according to the United States soil taxation system (United States Department of Agriculture, 2005). Oxisols are mainly located in south America and central Africa. Some Oxisols can also be found in Madagascar and Indonesia.

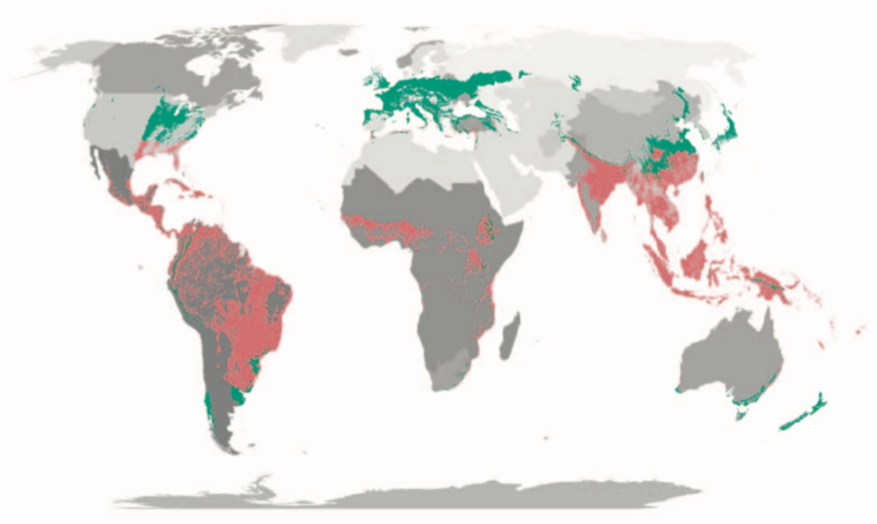

Figure A.3: Map of global croplands divided between warm (red areas) and temperate (green areas) humid climate (Strefler et al., 2018). Each category presents a different weathering rate, slower for the temperate regions and faster for the warm regions, and thus different potentials for ESW. Areas were defined in Strefler et al. (2018) based on the global ecophysiography map by Sayre et al. (2014)

## Basaltic glass solubility constant computation

Table A.1: Oxides dissolution reactions and thermodynamic equilibrium constants used to compute basaltic glass solubility constant at 25 °C

| Specie | Dissolution Reaction | log $K_{m,eq}$ |
|---|---|---|
| $Al_2O_3$ | $Al_2O_3 + 5\ H_2O \rightleftharpoons 2\ Al(OH)_4^- + 2\ H^+$ | -60.908[a] |
| FeO | $FeO + 2\ H^+ \rightleftharpoons Fe^{2+} + H_2O$ | 13.352[a] |
| MgO | $MgO + 2\ H^+ \rightleftharpoons Mg^{2+} + H_2O$ | 21.335[a] |
| CaO | $CaO + 2\ H^+ \rightleftharpoons Ca^{2+} + H_2O$ | 32.576[a] |
| $Na_2O$ | $Na_2O + 2\ H^+ \rightleftharpoons 2\ Na^+ + H_2O$ | 67.427[a] |
| $K_2O$ | $K_2O + 2\ H^+ \rightleftharpoons 2\ K^+ + H_2O$ | 84.041[a] |
| Amorphous silica | $SiO_{2(am)} \rightleftharpoons SiO_{2(aq)}$ | -2.714[b] |

[a] Original data from EQ3/6 database (Wolery, 1992).
[b] Retrieved from Gunnarsson and Arnórsson (2000).

## Porosity evolution with weathering duration and depth for different models and simulations

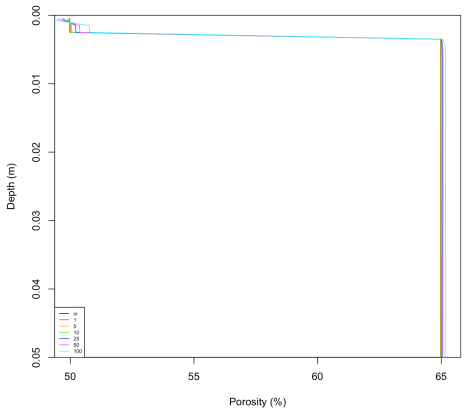


Figure A.4: Soil porosity evolution with depth and weathering duration after a single application of olivine of 5000 g $m^{-2}$ to the soil surface (M1). The model results with and without ion exchange (CEC) do not differ.

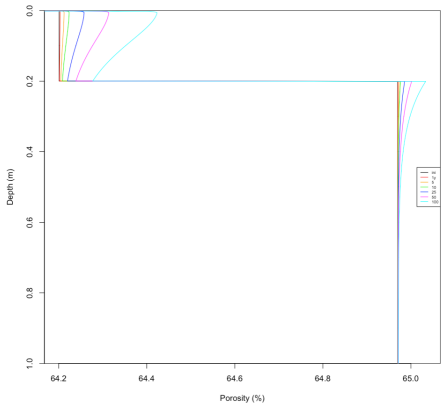


Figure A.5: Soil porosity evolution with depth and weathering duration after a single application of olivine of 5000 g $m^{-2}$ into the 0-20 cm top soil layer (M2). The model results with and without ion exchange (CEC) do not differ.

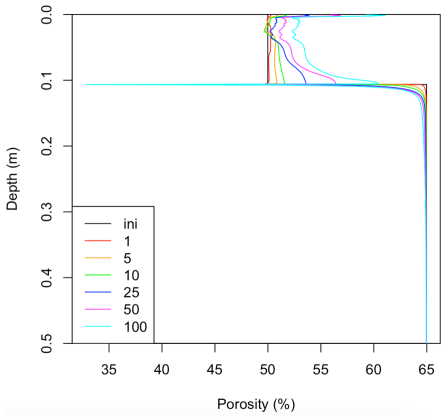


Figure A.6: Soil porosity evolution with depth and weathering duration after a single application of basalt of 150000 g $m^{-2}$ to the soil surface (M3). The model results with and without ion exchange (CEC) do not differ.

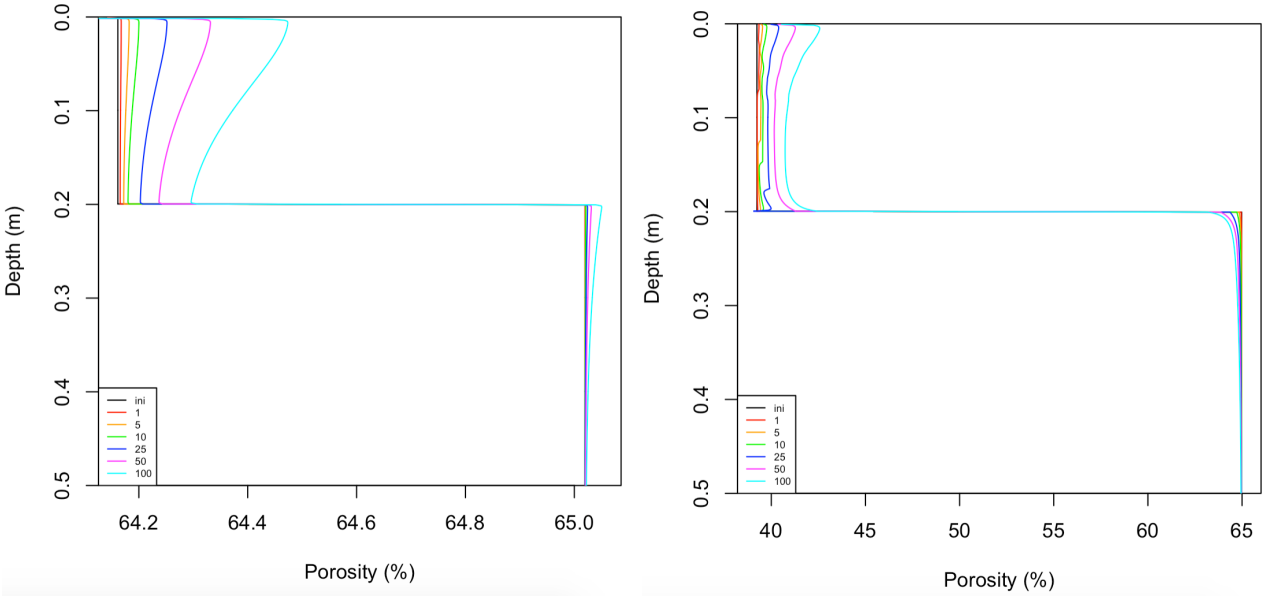


(a) M4/M4$_{CEC}$ (L)

(b) M4/M4$_{CEC}$ (H)

Figure A.7: Soil porosity evolution with depth and weathering duration after a single application of basalt of 5000 g $m^{-2}$ (31a) or 150000 g $m^{-2}$ (31b) into the 0-20 cm soil layer (M4). The model results with and without ion exchange (CEC) do not differ.

### Carbon dioxide removal potential of the different models and simulations

Table 7: Annual CDR as a function of weathering duration for L- and H-olivine applied to the soil surface (M1) and incorporated in the 0-20 cm layer (M2) and L- and H-basalt applied to the soil surface (M3) and incorporated in the 0-20 cm layer (M4). The model results with and without ion exchange (CEC) do not differ.

| Model and simulation | CDR [ g CO2 $m^{-2}$ $yr^{-1}$] | | | | | |
|---|---|---|---|---|---|---|
| | 1 yr | 5 yr | 10 yr | 25 yr | 50 yr | 100 yr |
| M1 L-olivine | 131.7 | 131 | 130.7 | 129.2 | 127.8 | 124.5 |
| M1 H-olivine | 2188.4 | 2214.7 | 2212.4 | 2205.5 | 2194.3 | 2172.4 |
| M2 L-olivine | 265.8 | 241.0 | 240.4 | 238.7 | 235.9 | 230.8 |
| M2 H-olivine | 4220.3 | 4262.1 | 4258.0 | 4246.1 | 4226.7 | 4188.4 |
| M3 L-basalt | 138.7 | 136.5 | 135.7 | 133.7 | 130.8 | 125.9 |
| M3 H-basalt | 6129.4 | 6246.8 | 4947.1 | 6013.5 | 6190.9 | 4231.1 |
| M4 L-basalt | 758.1 | 579.7 | 557.3 | 491.9 | 404.0 | 286.9 |
| M4 H-basalt | 3690.3 | 4061.3 | 4574.8 | 7417.8 | 11883.0 | 6951.5 |

### Solid phases abundances and aqueous species concentrations with a reduced solubility constant for allophanes

Figure A.8 shows the evolution of gibbsite and allophanes abundances after the incorporation of 150000 g $m^{-2}$ of olivine in the 0-20 cm layer. With the initial solubility constant for allophanes, gibbsite precipitated and no allophane was formed during the first 100 yr of weathering (Figure 12b). Here, the simulation predicts the precipitation of gibbsite in the first millimeters, followed by allophane precipitation and gibbsite dissolution in the rest of the profile until 50 yr of weathering. These precipitation of allophanes and dissolution of gibbsite are more intense in the layer in which the olivine is incorporated. Between 50 and 100 yr of weathering, there is no more $SiO_{2(aq)}$ in solution, hence, allophane dissolves and gibbsite precipitates.

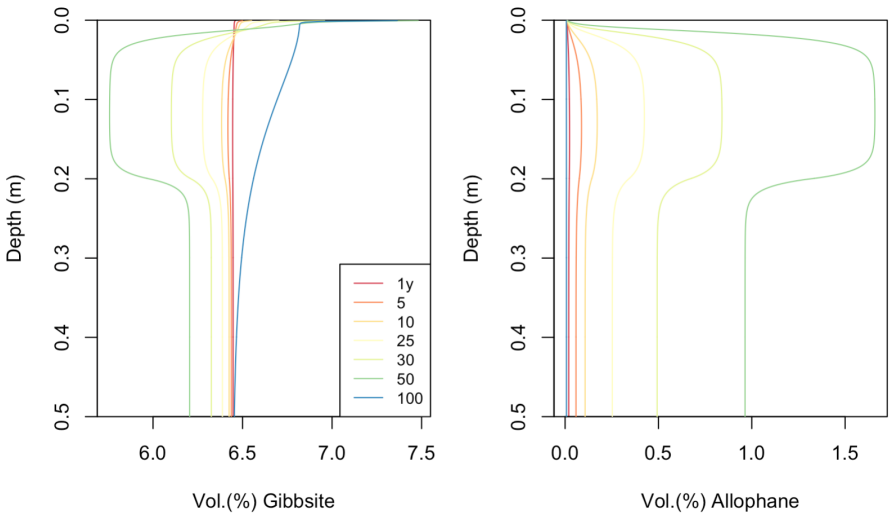


Figure A.8: Evolution with weathering duration and depth of the V%. of gibbsite and allophanes following the addition of 150000 g $m^{-2}$ of olivine into the 0-20 cm layer (M2) with a reduced solubility constant for allophanes. The model results with and without ion exchange (CEC) do not differ.

Figure A.9 illustrates the evolution of $AL^{3+}$ in solution after the addition of 150000 g $m^{-2}$ of

olivine on the soil surface. It can be seen that in the amendment layer (≈10 cm), a decrease in aluminium is predicted. Prior to the modification of allophanes solubility constant, an accumulation of $Al^{3+}$ was predicted at this depth (Figure 10b). Regarding the concentration in $SiO_{2(aq)}$ after the application of 5000 g $m^{-2}$ of olivine, it decreases with time to reach 0 after 100 yr, whereas with the initial solubility constant, the concentration profile after 100 yr was the same as after 1 yr of weathering.

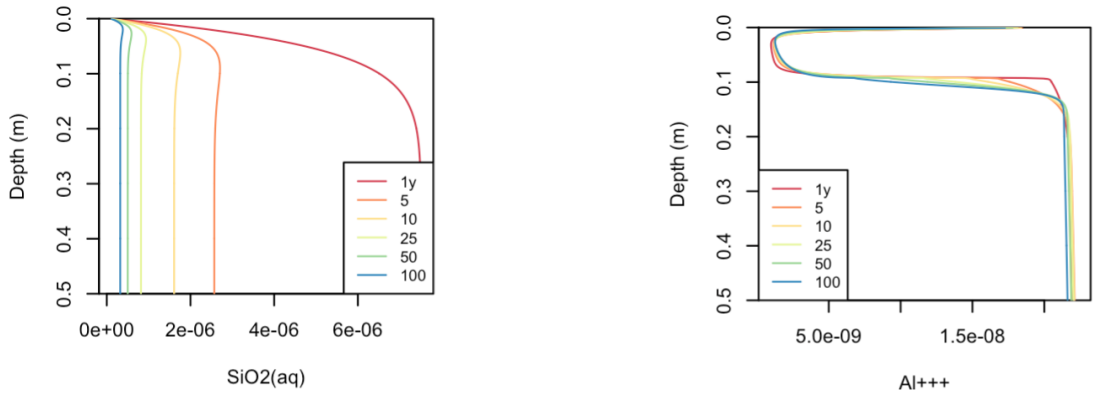


(a) $SiO_{2(aq)}$ (M1 (L)) (b) $Al^{3+}$ (M1 (H))

Figure A.9: Evolution with weathering duration and depth of the concentration [mol $L^{-1}$] of $SiO_{2(aq)}$ and $Al^{3+}$ in the soil solution following the addition of 5000 g $m^{-2}$ 32a or 150000 g $m^{-2}$ of olivine to the soil surface (M1) with a reduced solubility constant for allophanes. The model results with and without ion exchange (CEC) do not differ.

### Weathering rates and saturation index of primary and secondary solid phases in different models and simulations

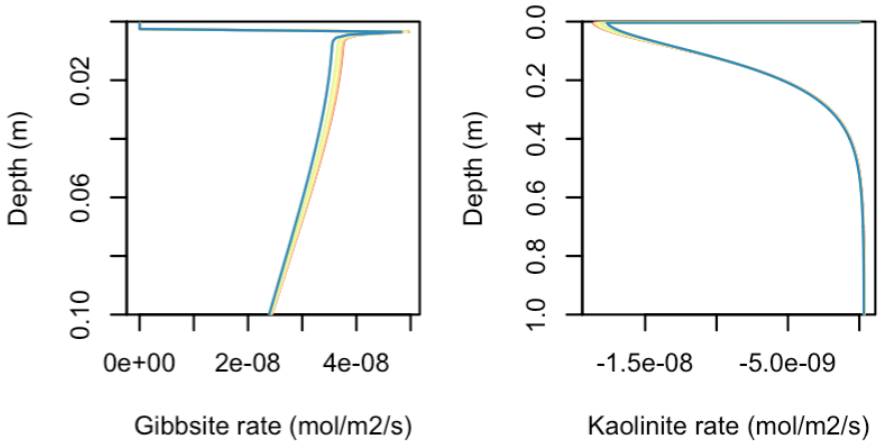


Figure A.10: Evolution of the weathering rate of gibbsite and kaolinite as a function of depth and weathering duration after the application of 5000 g $m^{-2}$ of olivine to the soil surface (M1). The model results with and without ion exchange (CEC) do not differ.

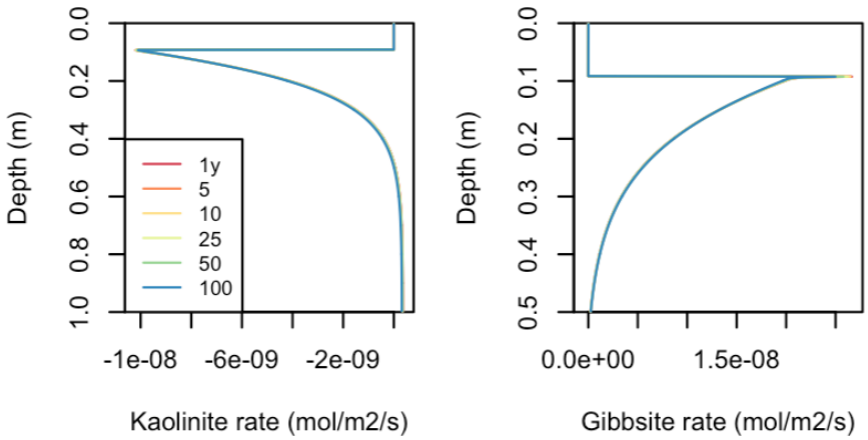


Figure A.11: Evolution of the weathering rate of gibbsite and kaolinite as a function of depth and weathering duration after the application of 5000 g $m^{-2}$ of olivine to the soil surface (M1). The model results with and without ion exchange (CEC) do not differ.

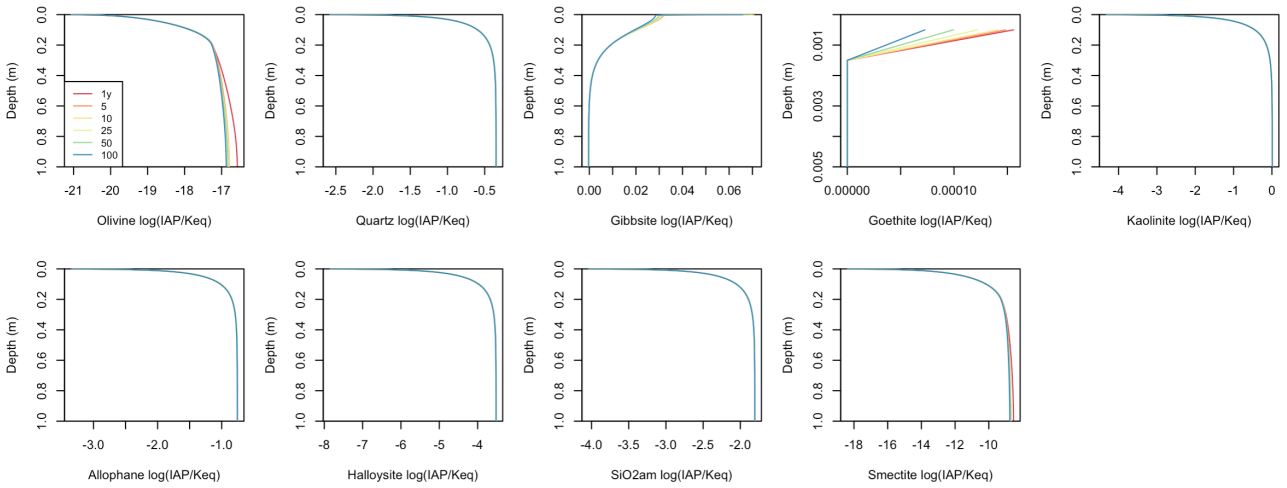


Figure A.12: Evolution of the saturation index of primary and secondary solid phases as a function of soil depth and weathering duration following the addition of 5000 g $m^{-2}$ of olivine incorporated into the 0-20 cm layer (M2). The model results with and without ion exchange (CEC) do not differ.

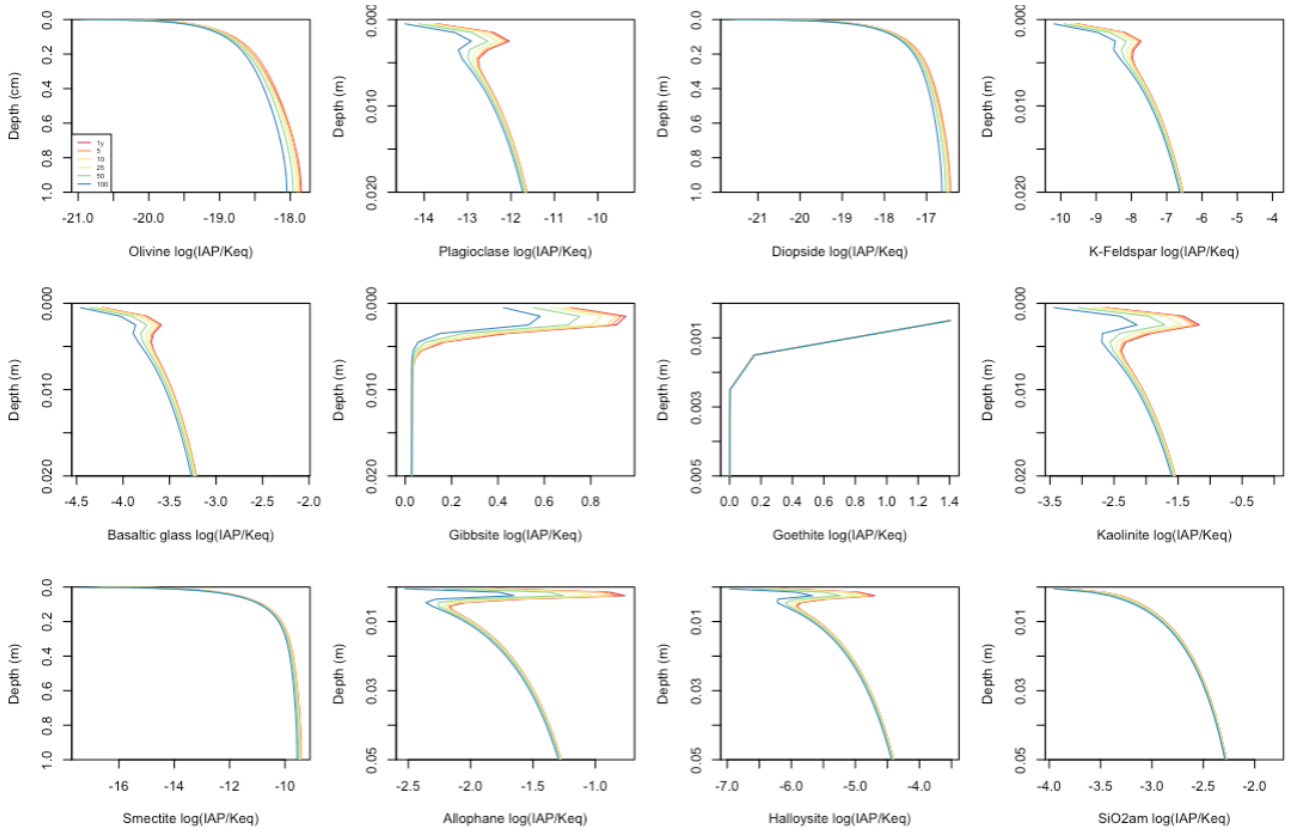


Figure A.13: Evolution of the saturation index of primary and secondary solid phases as a function of soil depth and weathering duration following the addition of 5000 g $m^{-2}$ of basalt applied to the soil surface (M3). The model results with and without ion exchange (CEC) do not differ.

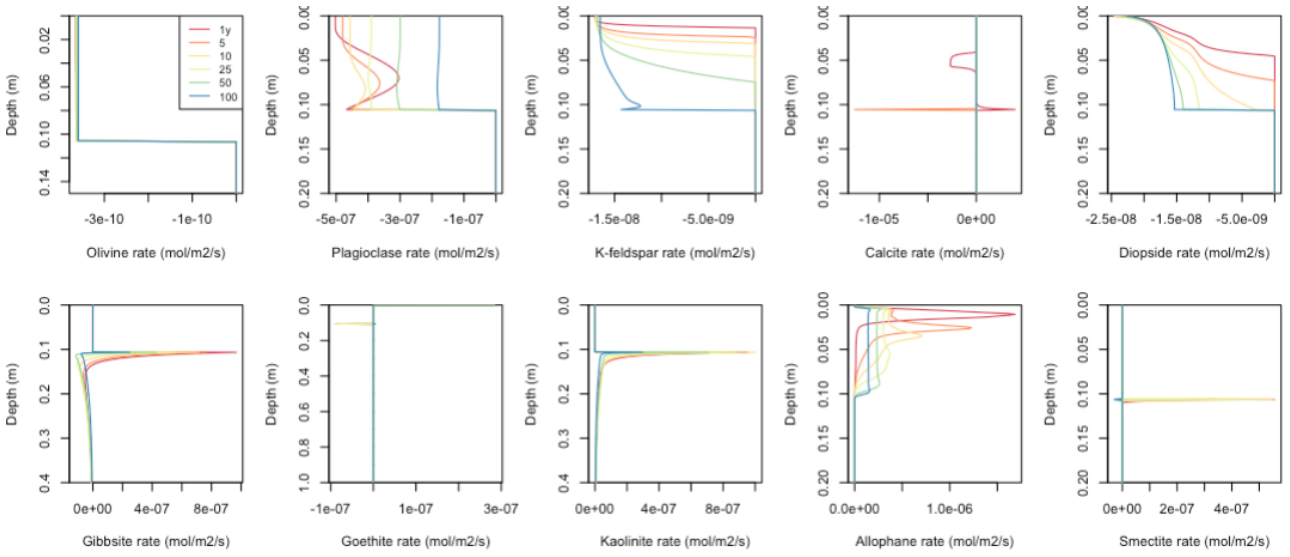


Figure A.14: Evolution of the weathering rate of primary and secondary solid as a function of depth and weathering duration after the application of 150000 g $m^{-2}$ of basalt to the soil surface (M3). The model results with and without ion exchange (CEC) do not differ.

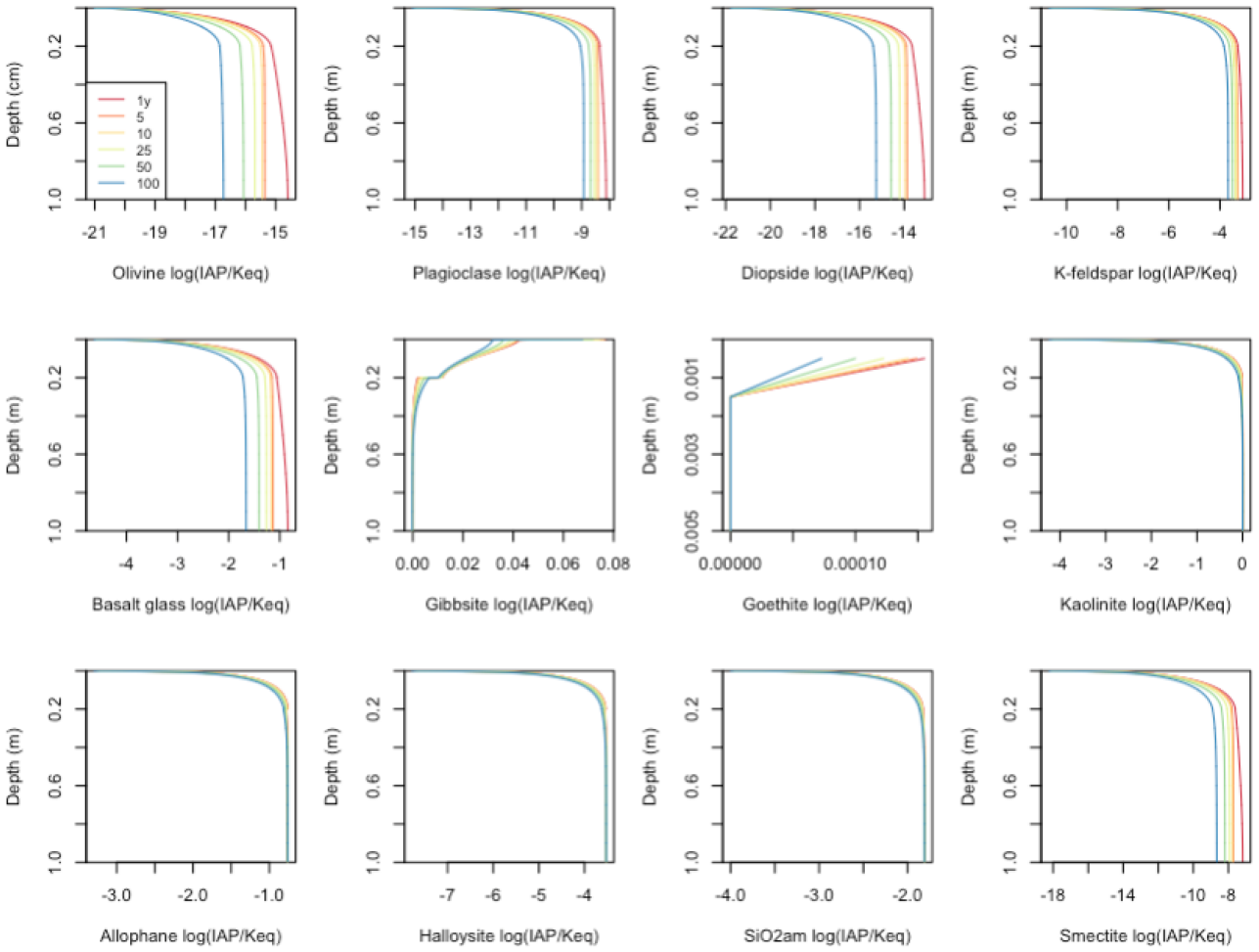


Figure A.15: Evolution of the saturation index of primary and secondary solid phases as a function of soil depth and weathering duration after the application of 5000 g $m^{-2}$ of basalt into the 0-20 cm soil layer (M4). The model results with and without ion exchange (CEC) do not differ.

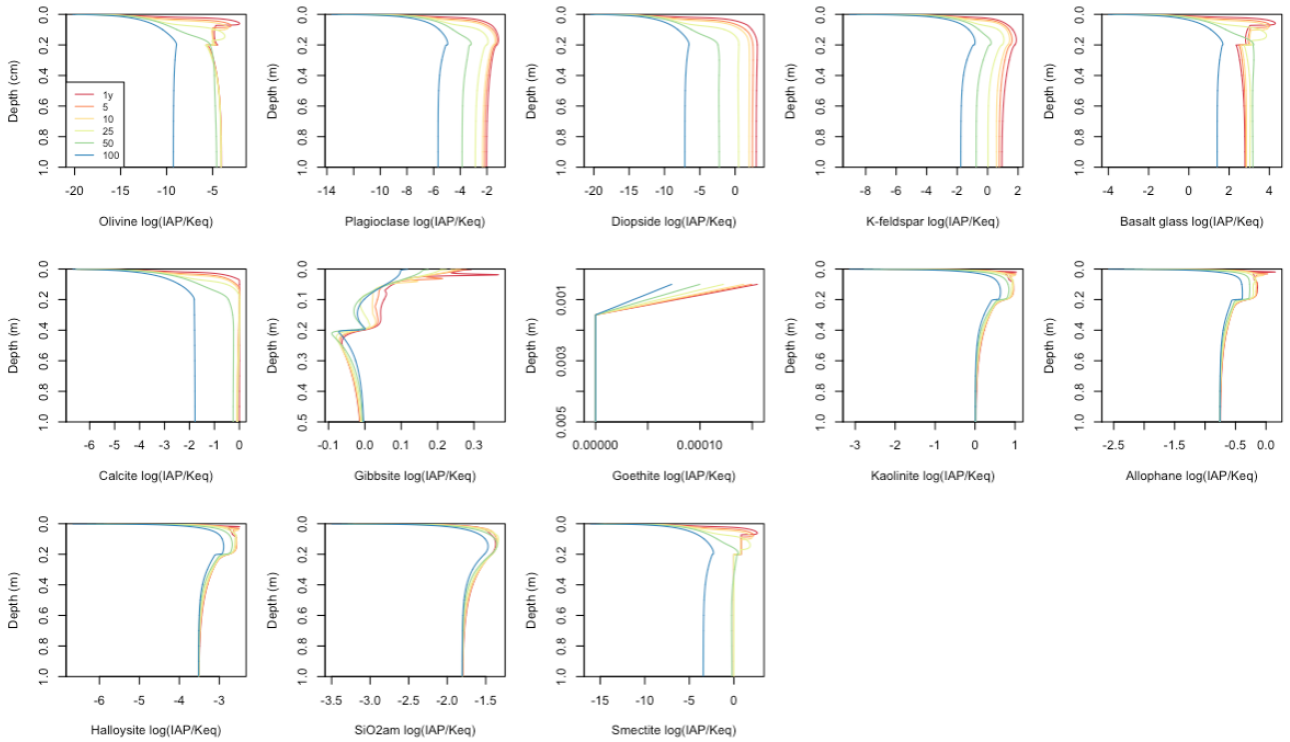


Figure A.16: Evolution of the saturation index of primary and secondary solid phases as a function of soil depth and weathering duration after the application of 150000 g $m^{-2}$ of basalt into the 0-20 cm soil layer (M4). The model results with and without ion exchange (CEC) do not differ.

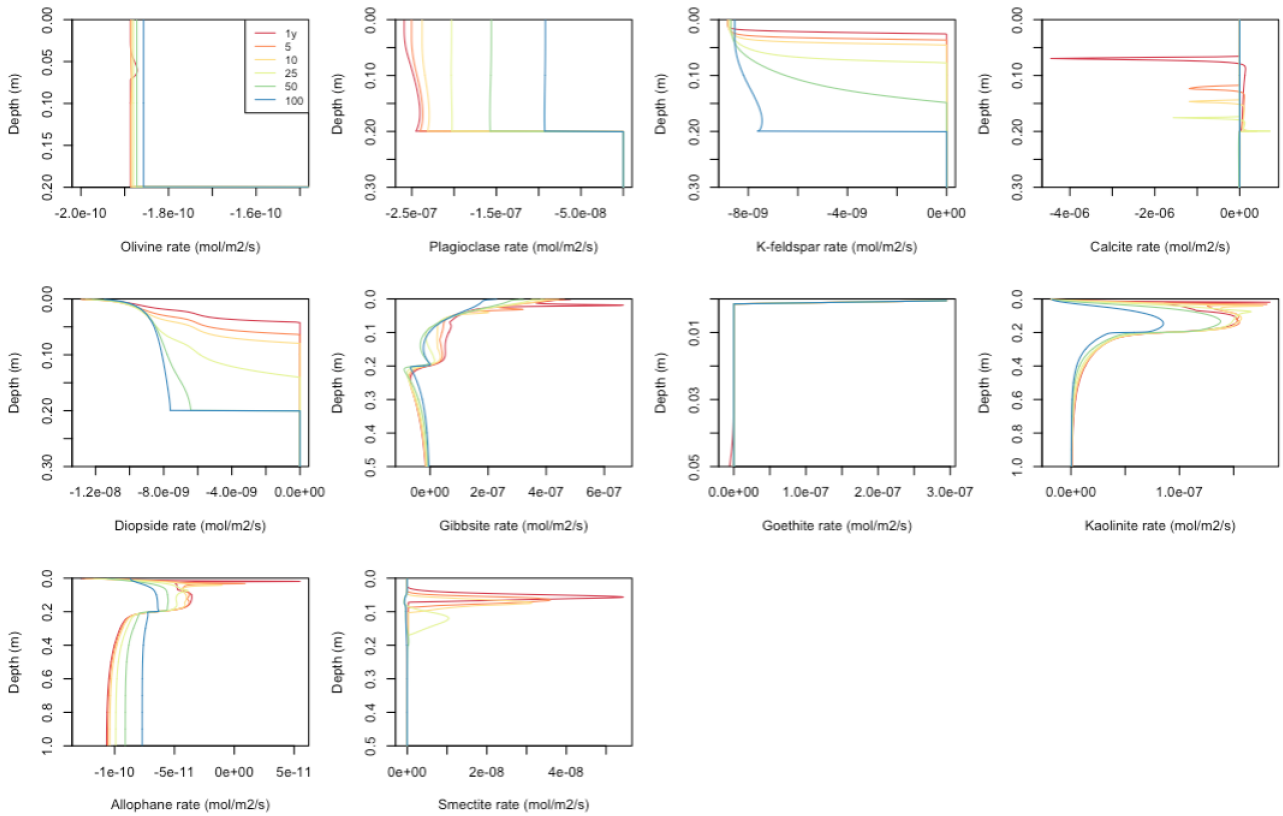


Figure A.17: Evolution of the weathering rate of primary and secondary solid phases as a function of soil depth and weathering duration after the application of 150000 g $m^{-2}$ of basalt into the 0-20 cm soil layer (M4). The model results with and without ion exchange (CEC) do not differ.

# Assessing the potential of enhanced silicate weathering in a tropical soil to remove atmospheric $CO_2$ and improve soil fertility: a modelling study

Juliette Glorieux

Enhanced silicate weathering in croplands is increasingly suggested as a NET that could remove significant quantities of $CO_2$ from the atmosphere and induce ancillary benefits to soil fertility and crop growth. However, many uncertainties remain as most existing ESW studies rely on the extrapolation of laboratory weathering rates to calculate $CO_2$ removal and barely evaluate ESW impact on soil properties. Moreover, different application modes and silicate materials are discussed but no studies precisely assess their effect under similar conditions. Given the scarcity of reactive transport modelling studies on ESW with basalt and olivine, we use the reactive transport model CrunchFlow to investigate the effect of adding both crushed silicates to an Oxisol to enhance chemical weathering and atmospheric CDR. We tested two application rates (5000 and 150000 g $m^{-2}$) either added to the soil surface or mixed within the top 20 cm of the soil profile.

We show here that repeated addition of basalt leads to higher annual CDR than olivine. However, the basalt annual CDR gradually decreases with time, whereas the olivine CDR is predicted to remain stable. We estimate annual CDR in the range of 2172-4188 and 4231-6951 g CO2 $m^{-2}$ $yr^{-1}$, after 30 annual applications of olivine and basalt respectively, subjected to 100 years of weathering. If deployed on tropical croplands, ESW may thus sequester about 3.3-10.4% of the current annual anthropogenic $CO_2$ emissions. Our results demonstrate that both CDR efficacy and soil fertility improvement are maximized when the material is incorporated into the top soil layer.

We found that basalt application may lead to higher co-benefits for soil fertility as significant concentrations of $K^+$, $Ca^{2+}$ and $Mg^{2+}$ are released into the soil solution. As ESW with olivine and basalt induces a significant increase in the soil solution pH, these nutrients will be readily available to crop plants. Moreover, repeated basalt application induces an increase in CEC, thereby increasing soil chemical fertility. In contrast, a $Ca^{2+}$ deficit in plants may arise after olivine amendment due to $Mg^{2+}$ continuous release.

Enhanced silicate weathering studies based on an RTM would benefit from a comparison with data acquired through a long-term in situ ESW experiment so as to validate the silicate weathering rates inferred theoretically and to better assess the actual co-benefits of ESW for soil fertility. Nevertheless, RTM offers a unique tool for exploring ESW in soils under various environmental conditions, soil properties and silicate application modalities.

**UNIVERSITÉ CATHOLIQUE DE LOUVAIN**
**Faculté des bioingénieurs**
Croix du Sud, 2 bte L7.05.01, 1348 Louvain-la-Neuve, Belgique | **www.uclouvain.be/agro**